Coherent Sensing of Magnetic Waveforms with Spin-squeezed Atoms

Ferran Martin Ciurana

A thesis submitted for the degree of Doctor of Philosophy

ICFO - The Institute of Photonic Sciences
UPC - Universitat Politècnica de Catalunya

Thesis Advisor: Prof. Dr. Morgan W. Mitchell
Thesis Co-Advisor: Dr. Robert J. Sewell

December, 2017

In loving memory of my mother
and my grandmother

"There comes a time when you realize that everything is a dream, and only those things preserved in writing have any possibility of being real"
James Salter, *All That is*

Abstract

Optical magnetometers use magnetically-sensitive atomic ensembles and optical read-out to detect the amplitude of magnetic fields. They have become the most sensitive instruments for measuring low-frequency magnetic fields surpassing competing technologies like superconducting quantum interface devices (SQUIDs), and find applications in a variety of fields ranging from medicine, biology and geophysics, as well as tests of fundamental physics. However, their fundamental sensitivity is bounded by quantum mechanical behavior of the atoms, which gives rise to the standard quantum limit (SQL). As many instruments are approaching this fundamental limit, it becomes necessary to explore ways to overcome the SQL. Quantum metrology studies strategies to increase the sensitivity beyond the SQL by means of quantum engineering the atomic states.

In this thesis, we investigate the quantum enhanced detection of time varying radio-frequency magnetic fields using a cold atomic ensemble of ^{87}Rb atoms held in an optical dipole trap. We first theoretically develop a new measurement technique based on stroboscopic back-action evading measurements that takes advantage of the atomic coherence. This measurement scheme is suitable for the detection of arbitrarily-chosen components of radio-frequency waveforms and includes radio-frequency magnetometry as a special case.

Experimentally, we demonstrate the capabilities of this technique using a linearly chirped waveform as a test case. As a first experiment, we demonstrate the selective response of the method in the coherently accumulated signal by the atoms. For this, we dispersively probe the atoms via Faraday rotation and non-destructively measure the induced magnetization.

In the last part of the thesis we demonstrate quantum enhanced magnetic field detection. In a measure-evolve-measure (MEM) sequence, a first stroboscopic quantum non-demolition (QND) measurement produces a state with reduced projection noise, followed by a period of free evolution where the atoms accumulate signal. A second QND measurement detects the change relative to the first measurement. We demonstrate entanglement-enhanced sensing of sinusoidal and linearly chirped waveforms, with metrologically-relevant noise reduction of ξ^2_{m} =0.84(8) and ξ^2_{m} =0.80(3), respectively. We achieve volume-adjusted sensitivity of $\delta \mathrm{B}\sqrt{\mathrm{V}} \approx 3.96$ fT$\sqrt{\mathrm{cm}^3/\mathrm{Hz}}$, comparable to the best radio-frequency magnetometers.

Resum

Els magnetòmetres òptics utilitzen conjunts d'atoms sensibles magnèticament i lectura òptica per detectar l'amplitud de camps magnètics. S'han convertit en els instruments més sensibles per mesurar camps magnètics de baixa freqüència, superant tecnologies rivals com els dispositius superconductors d'interfície quàntica (SQUID), alhora que troben aplicacions en camps tan diversos com la medicina, la biologia, la geofísica, fins a proves de física fonamental. No obstant això, la seva sensibilitat està fonamental limitada pel comportament quàntic dels àtoms que dóna lloc al límit quàntic estàndard (SQL). Donat que molts instruments s'aproximen a aquest límit fonamental, es imprescindible explorar maneres de supera-l'ho. La metrologia quàntica estudia estratègies per augmentar la sensibilitat més enllà del SQL mitjançant enginys quàntics en l'estat dels àtoms.

En aquesta tesi investigem la detecció de camps magnètics de freqüència de ràdio amb un conjunt d'atòms freds de ^{87}Rb mantinguts en una trampa de dipol òptic. En primer lloc, desenvolupem teòricament una nova tècnica de mesura basada en mesures estroboscòpiques que eviten la contra-acció de la mesura alhora que permet aprofitar la coherència atòmica. Aquest esquema de mesura és compatible amb la detecció de components elegits arbitràriament de formes d'ona de freqüència de ràdio i inclou la magnetometria de radiofreqüència com a cas especial.

Demostrem experimentalment les capacitats d'aquesta tècnica utilitzant una forma d'ona de prova amb canvi de freqüència lineal. Al primer experiment, demostrem la resposta selectiva del mètode en la senyal coherent acumulada pels àtoms. Per aconseguir-ho, provem de forma dispersiva els àtoms amb la sonda Faraday i mesurem no destructivament l'oscil.lació de Rabi de la població atòmica entre els subnivells magnètics dels nivells hiperfins de l'àtom.

A la darrera part de la tesi, demostrem la detecció de l'amplitud de camps magnètics amb precisió millorada gràcies a efectes quàntics. En una seqüència de mesura-evolució-mesura (MEM), una primera mesura quàntica, estroboscòpica i no destructiva (QND) produeix un estat amb soroll de projecció atòmic reduït. El segueix un període d'evolució lliure on els àtoms s'acumulen senyal. Una segona mesura QND detecta el canvi relatiu a la primera mesura. Demostrem detecció millorada per entrellaçament quàntic per a formes d'ona sinusoïdals i amb canvi de freqüència lineal, amb reduccions de soroll metrològicament rellevants

ξ^2_{m} =0.84(8) i ξ^2_{m} =0.80(3), respectivament. Aconseguim una sensibilitat ajustada pel volum $\delta \mathrm{B}\sqrt{\mathrm{V}} \approx 3.96\ \mathrm{fT}\sqrt{\mathrm{cm}^3/\mathrm{Hz}}$, comparable als millors magnetòmetres operant a freqüència de ràdio.

Contents

"Life, it seems, is not meaningless but, rather, so full of meaning that its meaning must be constantly murdered for the sake of cohesion and comprehension. For the sake of the storyline"

Steve Tesich, *Karoo*

1 Introduction

Metrology is the branch of science studying measurements. It has interest from both theoretical and experimental perspectives. The theoretical side proposes new measurement techniques to improve measurement precision and addresses the fundamental question of the *meaning* of a measurement. Experimentally, metrology studies improving instrumentation performance and standards. In 1879 Lord Kelvin considered the use of atomic transitions as universal references for measurements of fundamental quantities (Snyder F. Wilbert, 1973). It is planned from next year to redefine the International System of Units wholly from natural constants (Ian, 2012).

Correctly predicted by Lord Kelvin, atoms are used as standards for timekeeping (Bureau Internationel des Poids et Mesures). Pioneering work on atomic clocks was developed by Rabi (Rabi et al., 1939) and advanced by Ramsey (Ramsey, 1950). Timekeeping has been an area of intense research and holds the record for the most precise measurement performed with atoms to date (Bloom et al., 2014; Hinkley et al., 2013). The use of atoms is not only restricted to time measures. Atomic sensors have been used for detection of magnetic fields (Kominis et al., 2003), measurements of gravity gradients (Snadden et al., 1998; McGuirk et al., 2002), as inertial sensors for navigation (Geiger et al., 2011; Stockton et al., 2011), in experiments testing fundamental physics (Gaaloul et al., 2010; Bouchendira et al., 2011; Allmendinger et al., 2014) and have been proposed for the detection of gravitational waves (Dimopoulos et al., 2008; Chaibi et al., 2016).

When operated with an ensemble of N_{A} non-entangled atoms, the precision of

atomic sensors is limited by the quantum mechanical nature of the atomic polarization, limiting the uncertainty of the measurement to $\propto 1/\sqrt{N_{\mathrm{A}}}$, the standard quantum limit (SQL).

When the number of atoms is limited the precision in a measurement cannot be arbitrarily improved by classical means, which typically is achieved by increasing N_{A} unrestrictedly. Quantum metrology studies ways to further improve the measurement sensitivity when increasing the number of particles or the measurement time are unfeasible or inappropriate strategies. Attempts have been made using new measurement strategies in order to attain improved sensitivity (Giovannetti et al., 2011). Quantum metrology is based on the profitable use of entanglement, this is, quantum correlations among the particles used in the measurement.

Quantum metrology showed that the SQL can be surpassed using squeezed states, i.e., states that have redistributed noise from one quadrature to another (Wineland et al., 1992; Kitagawa and Ueda, 1993; Wineland et al., 1994). Squeezed states were firstly demonstrated in photon quadratures (Grangier et al., 1987; Predojević et al., 2008; Vahlbruch et al., 2008), and state-of-the-art experiments benefit from sensitivity improvement due to squeezed light (LIGO, 2013, 2011).

In this thesis we focus on spin-squeezing in neutral atomic systems and its application to quantum sensing. Pioneering work producing atomic spin squeezing mapped the nonclassical state of light into atoms (Hald et al., 1999). Shortly after, interactions between atoms constituting a Bose-Einstein condensates were exploited to produce states with reduced noise (Orzel et al., 2001; Esteve et al., 2008; Sackett, 2010; Riedel et al., 2010). In these setups was possible to achieve large amounts of squeezing, but it was challenging to utilize the squeezing to sense ambient perturbations.

The development of quantum non-demolition (QND) measurements allowed generation of squeezed states using measurements (Kuzmich et al., 1998, 2000; Appel et al., 2009; Takano et al., 2009; Schleier-Smith et al., 2010b; Chen et al., 2011; Sewell et al., 2012). In this case, the squeezing is achieved by dispersive atom-light interactions where the atoms cause a state-dependent phase shift on the light, which then is measured. An advantageous characteristic of measured-based squeezing is that at the same time the probing induces the squeezing, the measurement output is used to characterize the state, reducing two challenges of squeezing into a single one. The uncertainty of the collective atomic state is reduced to the uncertainty of the detected photons. The light measurement precision must be of lower uncertainty than the imprinted atomic quantum projection noise.

The main challenge for QND measurement to produce squeezing is to get the maximum possible information per photon. Photons scattered into free space carry information about the atomic state, and if lost they will not contribute to

the creation of entanglement necessary to project the atoms into a spin-squeezed state. Is therefore necessary that each atom has a low probability of scattering a photon. In order to gain information about the atomic state, a large light-atom interaction strength is desirable. Different systems have been used to get the interaction strength required for producing atomic squeezed states, from hot vapor cells containing large atom number (Lucivero et al., 2016) where each photon interacts with a large number of atoms, to cold and trapped atoms in special geometries (Kubasik et al., 2009) where the photons efficiently interact with the atoms. A different approach is to build optical cavities around trapped atoms (Schleier-Smith et al., 2010b; Chen et al., 2011) to enhance the coupling strength as the photons interact many with the atoms, resulting in an build-up of phase shift during the different round-trips. Cavity measurement-based setups have enabled larger amounts of squeezing (Bohnet et al., 2014; Hosten et al., 2016b,a). To date, in these cavity enhanced measurements the atoms are prepared in a clock state, insensitive to magnetic field changes.

In contrast to the above-described works, here we use the atoms as sensors for radio frequency magnetic fields. Alkali atom based magnetometers have shown exceptional sensitivities (Kominis et al., 2003; Sheng et al., 2013) in DC magnetic field measurements but atoms can also be used to efficiently detect radio frequency fields (Savukov et al., 2005; Shah et al., 2010; Chalupczak et al., 2012; Savukov et al., 2014). A simple and effective method is to optically pump atoms along the direction of an applied DC field, and then wait for them to interact with an RF perturbation. The bias field keeps the spin polarization stable against most magnetic perturbations, with the important exception of resonant fields, i.e. those at the Larmor frequency. Resonant fields drive a precession of increasing amplitude, so that a measurement of the amplitude after an accumulation time indicates the amplitude of the resonant part of the RF field.

This measurement process as just described is limited by quantum noise - the state that results from optical pumping has a spin noise in the orthogonal components $\propto 1/\sqrt{N_{\mathrm{A}}}$. This noise can, however, be squeezed, reducing the spin noise and thus the minimum signal that can be detected. As described above the squeezing can be performed by measurement, so that a sequence of measurement, evolution, and measurement, a relatively simple modification to the naive RF magnetometry sequence, can beat the standard quantum limit for sensing of RF fields.

While the dynamics of time varying fields can be reconstructed by measuring over successive, acquisition periods with increasing duration or rapidly sampling the signal using small acquisition steps, these protocols are inefficient at sensing the magnetic fields. Quantum noise and quantum coherence play essential roles in determining the projection noise sensitivity of sensing magnetic fields with N_{A}

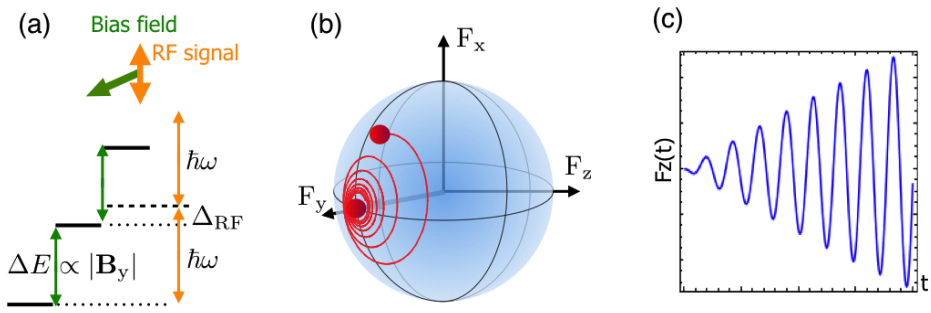

Figure 1.1: (a) A bias field breaks the degeneracy of the hyperfine ground states by an energy shift proportional to the bias field strength ΔE. An orthogonal RF magnetic field couples two hyperfine levels. The atoms are solely resonant to radio-frequencies matching ΔE. (b) An atomic ensemble spin polarized along the bias field will start to spiral around its original orientation due to the interaction with the RF field. (c) Measuring along the direction orthogonal to both magnetic fields, an increasing signal is expected. From the amplitude of the measured signal it is possible to infer the strength of the RF field.

spins-f atoms (Budker and Romalis, 2007)

$$\delta B_{\mathrm{PN}} \sqrt{T_{\mathrm{acq}}} \propto \frac{1}{\sqrt{2 f N_{\mathrm{A}} \tau}} \tag{1.1}$$

where T_{acq} is the total acquisition time including averaging repeated measurements. The factor $1/\sqrt{2fN_{\mathrm{A}}\tau}$ reflects the standard quantum limit spin projection noise of the atomic precession angle. The signal accumulation time τ is determined by the smaller of the single-measurement duration and spin atomic coherence time. Analogous expressions govern clocks and other atomic instruments (Degen et al., 2017). As shown by Eq. (1.1), atomic magnetometers have best performance when the measurement duration equals the atomic spin coherence time.

We detect radio-frequency magnetic fields at ≈40 kHz taking advantage of the quantum coherence of an ensemble of spin squeezed atoms. We first prepare the atoms in a spin squeezed state by means of stroboscopic QND measurements which evade the measurement back-action (Thorne et al., 1978). The quantum enhanced atoms are then allowed to evolve for a long interrogation time where they are solely under the influence of the external radio-frequency magnetic perturbation. The atoms accumulate phase information for a signal of frequency matching the Larmor frequency. A second stroboscopic QND measurement is

performed in order to measure the amplitude acquired by the atoms due to the field. We show quantum noise reduction in the measurement of the field's amplitude due to entanglement among the atoms. Other quantum enhanced atomic magnetometers have been demonstrated for the detection of RF fields in the range of 300 kHz (Wasilewski et al., 2010) to 6.8 GHz (Ockeloen et al., 2013). The method here presented can be exploited to sense a wide range of frequencies by changing the strength of the field and carefully adjusting the probe frequency (Savukov et al., 2005). When the coherence time exceed the measurement time, spin squeezing improves the short-term sensitivity and the measurement bandwidth (Huelga et al., 1997; André et al., 2004; Auzinsh et al., 2004).

To date, coherent measurements has been used to detect constant magnetic fields (Leroux et al., 2010b; Sewell et al., 2012) or simple sinusoidal signals (Ockeloen et al., 2013). In this thesis, we demonstrate a new technique that accumulates signal over a long time, as the RF magnetometry described above does, but which is capable of detect time varying radio-frequency magnetic fields. As described above, the RF atomic magnetometers are sensitive to RF fields matching the Larmor frequency. By modulating the strength of the bias field we change the atomic resonance frequency as a function of time, and thus extend the coherent detection to more general radio-frequency waveforms, those with time-varying frequencies. The measurable amplitude takes the form of an overlap integral, with a pattern function that is controlled by the experimenter. The pattern function depends on the modulated bias field. When the bias field profile matches the waveform the amplitude is maximal. In this way, the amplitude of an arbitrary signal component can be detected. We show that the sensitivity of such a measurement can be improved by using quantum enhanced atoms

Outline of the thesis

The manuscript is organized as follows:

Chapter 2 describes the theoretical concepts. We introduce the collective variables for atomic ensembles and see that they follow the usual commutator relations for angular momentum operators. We explain coherent and squeezed states. We characterize the light probe pulse in terms of the Stokes operators. We use these definitions on the description of the light-atom interaction, and show that this interaction can be described as a quantum non-demolition measurement capable of preparing spin squeezed states. At the end of the chapter we discuss how to experimentally estimate the interaction strength between atoms and photons.

In **Chapter 3** we briefly summarize the experimental setup as it has been presented elsewhere (Kubasik, 2009; Koschorreck, 2010; Dubost, 2012; Napolitano, 2014; Behbood, 2015; Colangelo, 2016). We describe the improvements made in

the course of this thesis: a new laser system to cool and trap more atoms into the dipole trap and an upgrade of the dipole trap optics to increase the light-atom coupling. We present the preparation of the atoms in two different and orthogonal coherent spin states as well as their efficiencies. The last sections show the characteristic of the trapped atoms: number of atoms and their temperature, atomic cloud volume, lifetime, light-matter coupling constant and scattering rate.

Chapter 4 presents the development of a fast, pulsed and low-noise photodetector based on a charge sensitive amplifier. We measure its noise characteristics and its shot-noise limited range of operation. We enrich the measurement capabilities by making the signal available in real time using a solution based on analog electronics. We compare the performance on the two scenarios, real-time and off-line detection. Finally we compare the performance of our detector with other detectors present in the bibliography.

Chapter 5 details the working principle of atomic ensembles for constant and oscillating magnetic fields. We discuss the efforts to produce a homogeneous magnetic field along the length of the atomic cloud resulting in a long spin coherence time. We describe the control on the magnetic field and a technique to measure the bias magnetic field and the gradient along the trap axis. We present measurements of magnetic Rabi oscillations and from those we calibrate the strength of the radio-frequency field. We then present our measurement strategy to coherently detect arbitrarily-shaped radio-frequency time varying signals using a cold atomic ensemble. We experimentally verify the theory using a particular case of waveform, a linearly chirped signal.

Chapter 6 describes detection of radio-frequency fields and linearly chirped waveform amplitudes beyond the projection-noise limit, using stroboscopic backaction evading measurements on magnetic atomic ensembles. The combination of quantum non-demolition measurements and stroboscopic probing in a measure-evolve-measure sequence gives this quantum sensing advantage, while also allowing full use of the system coherence, resulting in a sensitivity-volume figure of merit comparable to the best radio-frequency magnetometers at these frequencies.

Finally, **Chapter 7** summarizes the main results and discusses possible applications of the work.

"Most human beings have an almost infinite capacity for taking things for granted"

Aldous Huxley, *Brave New World*

"There really is nothing quite like total ignorance, is there?"

Neil Gaiman, *Neverwhere*

2

Quantum description of atoms and light

In this chapter we introduce the main actors appearing during the thesis, rubidium 87 atoms and optical pulses. We start by describing the angular momentum properties of ^{87}Rb and see how they set limits on the precision of atomic sensors. We introduce the concept of spin squeezing as a way to overcome these limitations. We then describe the optical pulses following a collective variable description of their spin and find strong analogies between the mathematical description of the optical and material systems.

Once we have formally described the two "parties", we study how they interact for the particular case where the optical pulses are far detuned from an atomic transition. This interaction gives rise to a Hamiltonian with a term describing a quantum non-demolition type of measurement plus unwanted terms. We describe our approach to cancel the undesired term in the Hamiltonian and describe how a QND measurement can produce spin squeezed states.

The theoretical description summarized here is brief and far from exhaustive. Along the text we include numerous references to the literature to provide the necessary context.

2.1 Atomic Spin State

The experiments described in this thesis are carried out using rubidium 87 atoms, (^{87}Rb), an alkali atom. Alkali metal atoms are useful for a variety of applications because they have a single electron in the outer-most energy shell that can be easily manipulated. The energy level structure of the atom can be qualitatively understood by considering only the valence electron and the nucleus, i.e., ignoring the electrons of the inner energy shells. The valence electron has spin $s = 1/2$. The ground state is an s shell with orbital angular momentum $l = 0$, so the total electron angular momentum is $j = l + s = 1/2$. The first excited state is a p shell with $l = 1$. The fine structure splits this state into the $p_{1/2}$ and $p_{3/2}$ levels, where we use the standard spectroscopic notation with the subscript denoting the total angular momentum j. The energy transition between the ground state and the $p_{1/2}$ and $p_{3/2}$ levels are referred as the D_1 and D_2 transitions, with transitions wavelength of 795 nm and 780 nm, respectively.

All alkali metal isotopes have nonzero nuclear spin i. In the case of ^{87}Rb $i = 3/2$. The hyperfine interaction between electron and nuclear spins further splits the atomic energy levels into states with total atomic spin $f = i + j$. The electronic ground state is split into levels with $f = 1$ and $f = 2$, separated by the hyperfine energy splitting. We work on the D_2 transition where the excited, $p_{3/2}$, has four manifolds f'={0, 1, 2, 3}. Each of these manifolds has $2f + 1$ magnetic sub-levels, described by m_f. In Fig. 2.1 the 24 electronics states for the D_2 transition are represented.

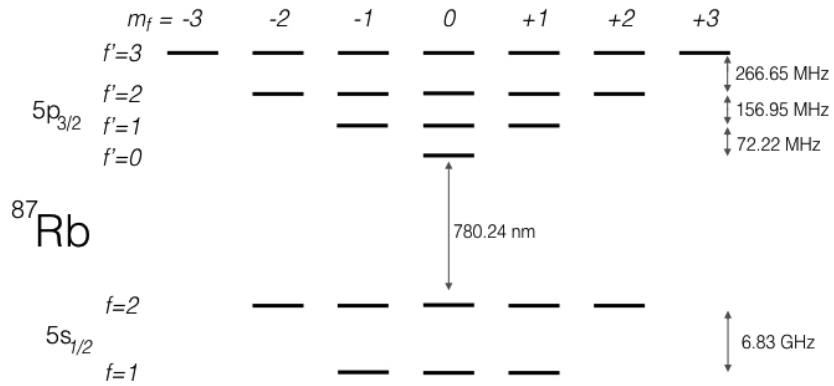

Figure 2.1: D_2 transition for ^{87}Rb . The states are labeled with the total angular momentum f and the magnetic quantum number m_f.

The total angular momentum **f** and the magnetic quantum number m_f are

enough to define the energy levels of the ground states. As we will see later, given than the hyperfine ground state separation (6.83 GHz) is much larger than the probe detuning ($\Delta \sim$700 MHz), and that the probe is far from resonance to any excited state, it is possible to ignore the effect of the $f = 2$ hyperfine level. And so, we restrict ourselves to the $f = 1$ hyperfine level.

We denote the total angular momentum of a *single atom* by $\hat{\mathbf{f}}$ and for a collection of atoms we denote the *collective* total angular momentum by $\hat{\mathbf{F}}$ as

$$\hat{\mathbf{F}} = \sum_{i=1}^{N_{\mathrm{A}}} \mathbf{f}^{(\mathbf{i})} \tag{2.1}$$

where N_{A} is the total number of atoms and $\mathbf{f}^{(\mathrm{i})}$ is the total angular momentum of the i'th atom. To write Eq. (2.1) we have assumed symmetry under particle exchange. This allows us to write the total angular momentum of the collective state in the symmetric space as $F_{\mathrm{tot}} = N_{\mathrm{A}} f$, whereas the full Hilbert space has dimension $(2f + 1)^{N_{\mathrm{A}}}$.

The components for the collective spin operator obey the same commutation relation rules as single atom operators

$$[\hat{F}_i, \hat{F}_j] = i\epsilon_{ijk}\hat{F}_k \tag{2.2}$$

where ϵ_{ijk} is the Levi-Civita symbol. Here and during the rest of the thesis we have taken $\hbar = 1$. The non-vanishing commutator of the spin operators leads to the Robertson-Schödinger uncertainty relation

$$\mathrm{var}(\hat{F}_i)\mathrm{var}(\hat{F}_j) \geq \frac{1}{4}|\langle \hat{F}_k \rangle^2| \tag{2.3}$$

where the variances are given by $\mathrm{var}(\hat{F}_i) = \langle \hat{F}_i^2 \rangle - \langle \hat{F}_i \rangle^2$.

A coherent spin state (CSS) is a state with angular momentum maximum along a particular direction in space, for example along y

$$\langle \hat{F}_y \rangle = f N_{\mathrm{A}} \tag{2.4}$$

and is the state with minimum uncertainty, whose orthogonal spin component variances are equal and saturate the uncertainty principle

$$\mathrm{var}(\hat{F}_x) = \mathrm{var}(\hat{F}_z) = \frac{1}{2} f N_{\mathrm{A}} \tag{2.5}$$

The above equation expresses the minimum noise that a a non-entangled state can have due to projection noise (PN), caused by the random outcome of a measurement orthogonal to the atom's polarization axis. A convenient way to illustrate the atomic state is with the generalized Bloch sphere (Bloch, 1946), which basically is a mapping of the spin vector on a sphere. In Fig. 2.2 the CSS expressed by Eq. (2.4) is represented on a Bloch sphere.

2.1.1 Phase estimation

Consider the same state we have just introduced, a CSS polarized along the y-axis. If the atoms are under the influence of a magnetic field of unknown strength along the x-direction, described by $\mathbf{B} = B_\mathrm{x}\mathbf{e}_\mathrm{x}$, the collective spin will precess around $\mathbf{e}_\mathrm{x}$. The angle the atoms rotate during a time t is $\theta = \gamma B_\mathrm{x} t$, where γ is the gyromagnetic ratio. It is possible to determine the magnitude of the bias field B_x from the displaced angle θ. For small interaction time, the angle is small and B_x can be deduced from measuring F_z

$$F_\mathrm{z} \approx \langle F_\mathrm{y} \rangle \theta \tag{2.6}$$

By error propagation it is possible to calculate the variance of the measurement of the angle θ, given by

$$\mathrm{var}(\theta) = \frac{\mathrm{var}(F_\mathrm{z})}{\langle F_\mathrm{y} \rangle^2} \tag{2.7}$$

Intuitively, the angular resolution depends on the variance of the measured spin component. At the same time, it also depends on the *mean spin length* which acts as a lever arm, see Fig. 2.2. The spin length is orthogonal to the uncertainty disk. A larger the spin makes the measured displacement of F_z larger, improving the precision on which θ can be estimated. However, a larger spin length also increases the uncertainty in the F_z component, Eq. (2.5). This two competing mechanisms and gives rise to the fundamental sensitivity in which an angle can be estimated using a CSS, called the standard quantum limit (SQL). Following Eq.s (2.4) and (2.5) it can be written as

$$\mathrm{var}(\theta)_\mathrm{CSS} = \frac{1}{2f}\frac{1}{N_\mathrm{A}} \tag{2.8}$$

2.2 Spin Squeezing

Exploring Heisenberg's uncertainty relation for the angular spin operators, Eq. (2.3), we notice that the inequality constrains the product of uncertainties for the in-plane spin components, but there is no bound on the variance of individual components. For an ensemble used in the previous example, with $\langle F_\mathrm{y} \rangle = f N_\mathrm{A}$, it is possible for one if its components to have variance $\mathrm{var}(F_\mathrm{z}) \leq f N_\mathrm{A}/2$, a reduced noise compared to Eq. (2.5).

Collective spin states with reduced variance compared to a CSS are called spin squeezed states (SSS). A spin state with noise reduced (*squeezed*) in $\hat{F}_\mathrm{z}$ must have increased noise (*anti-squeezed*) in $\hat{F}_\mathrm{x}$ as the Heisenberg principle dictates. In discussions of squeezing there are different definitions that use different noise

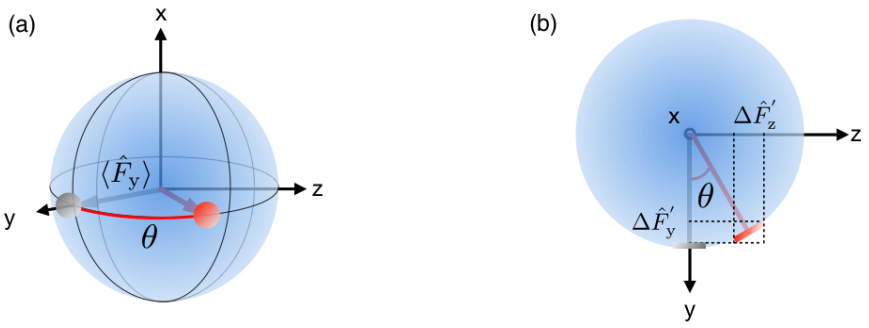

Figure 2.2: An atomic ensemble prepared with the mean spin along y is under a magnetic field along x of strength B_x which causes the collective spin to rotate about x by an angle θ. By measuring $\hat{F}_z$, the rotated angle θ can be determined. The fundamental resolution is determined by the quantum uncertainty of the spin projection noise, shown here as an uncertainty patch, figure (a). The initial uncertainty in the F_z-component limits the precision on which θ can be determined, and the dynamical evolution coherently transfer this uncertainty into $\hat{F}_y$ whose uncertainty initially was neglegible, figure (b).

reference levels that lead to SSS having different properties (Ma et al., 2011). In the following we focus on one of the criteria more widely used to quantify spin squeezing, the Wineland criterion.

2.2.1 Quantifying spin squeezing

As we have seen, the achievable angular resolution using a CSS is bounded by the atomic projection noise, Eq. (2.8). The SQL can, however, be surpassed by using spin squeezed states, states which have the uncertainty of one of its components smaller than CSS, see Fig. 2.3. Due to the smaller angular uncertainty of the SSS the angular resolution is improved. At the same time, the spin length is orthogonal to the squeezed component, and a larger spin length makes the measured displacement of F_z larger, enhancing the measurement sensitivity.

Wineland (Wineland et al., 1992; Itano et al., 1993) proposed a parameter that quantifies the metrological usefulness of a squeezed state by comparing it to the performance of a CSS

$$\zeta_m^2 = \frac{\mathrm{var}(\theta)}{\mathrm{var}(\theta)_{\mathrm{CSS}}} = \frac{2fN_A\mathrm{var}(F_z)}{\langle F_y \rangle^2} \tag{2.9}$$

where we have used Eq. (2.8). $\mathrm{var}(\theta)$ is the angular variance of the state we want to quantify. A collective atomic state with $\zeta_{\mathrm{m}}^2 < 1$ is a spin squeezed state that has improved metrological sensitivity over a CSS.

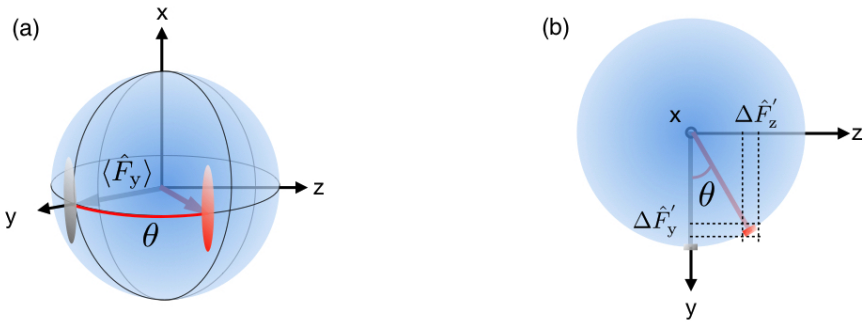

Figure 2.3: A spin squeezed state with reduced noise in the F_{z}-component is used as to sense a magnetic field along x-axis. The reduced noise in $\hat{F}_{\mathrm{z}}$ allows determination of the rotation angle θ with sensitivity beyond the SQL.

2.3 Polarization States of Light

In the experiment we probe the atoms using optical pulses. In the this section we describe how we characterize the light pulses by collective photon spin, and find strong symmetry between the description of light and the description of atomic spin described in Sec 2.1.

The electric field of a single mode with two orthogonal polarizations can be expressed by (Mandel and Wolf, 1995)

$$\hat{E} = \hat{E}^{(+)} + \hat{E}^{(-)} \tag{2.10}$$

where the positive and negative frequency parts are described by

$$\hat{E}^{(+)} = \sqrt{\frac{\hbar\omega}{2\varepsilon_0 V}}(\hat{a}_+ \mathbf{e}_+ + \hat{a}_- \mathbf{e}_-) e^{i\mathbf{k}\cdot\mathbf{z}-\omega t} \tag{2.11}$$

with the property that

$$\hat{E}^{(+)} = (\hat{E}^{(-)})^\dagger \tag{2.12}$$

In the definition of Eq. (2.11), a_i are the annihilation operators of the two modes $i = \{+, -\}$, ε_0 is the vacuum electric permittivity, $\hbar$ is the reduced Planck's constant, V is the mode volume and $\mathbf{e}_i$ are unit vectors describing the polarization.

The angular frequency of the field can be expressed as $\omega = |\mathbf{k}|c$, where c is the speed of light and $\mathbf{k}$ is the wave-vector.

The annihilation operator and its conjugate, the creation operator, obey the commutation relation

$$[\hat{a}_i, \hat{a}_j^\dagger] = \delta_{ij} \tag{2.13}$$

where $\{i, j\} \in \{+, -\}$. The annihilation operator lowers the number of photons in the given mode by one, while the creation operator increases the number of photons in a given mode by one. The complete set of basis vector is given by

$$\begin{aligned} \mathbf{e}_+ &= \frac{-1}{\sqrt{2}}(\mathbf{e}_x + i\mathbf{e}_y) \\ \mathbf{e}_- &= \frac{1}{\sqrt{2}}(\mathbf{e}_x - i\mathbf{e}_y) \\ \mathbf{e}_0 &= \mathbf{e}_z \end{aligned} \tag{2.14}$$

where $\{\mathbf{e}_x, \mathbf{e}_y, \mathbf{e}_z\}$ are unit vector in the Cartesian coordinate system.

The energy of the EM field is given by $\hat{H} = \sum_i \hbar\omega(\hat{a}_i^\dagger \hat{a}_i + 1/2)$. From here on, the zero-point energy (the $1/2$ in the previous expression) will be neglected. The photon number operator is given by $\hat{n}_{\mathrm{ph,i}} = \hat{a}_i^\dagger \hat{a}_i$, and the single photon energy is thus $\hbar\omega$.

When the light is used as a meter it is convenient to derive a signal from some comparison between two modes, as for example the polarization. The polarization state is well described by the Stokes operators (Guenther, 1990). For a pulse of light propagating in the z-direction it becomes

$$\begin{aligned} \hat{S}_0 &= \frac{1}{2}(\hat{a}_+^\dagger \hat{a}_+ + \hat{a}_-^\dagger \hat{a}_-) \\ \hat{S}_\mathrm{x} &= \frac{1}{2}(\hat{a}_+^\dagger \hat{a}_- + \hat{a}_-^\dagger \hat{a}_+) \\ \hat{S}_\mathrm{y} &= \frac{1}{2}(\hat{a}_-^\dagger \hat{a}_+ - \hat{a}_+^\dagger \hat{a}_-) \\ \hat{S}_\mathrm{z} &= \frac{1}{2}(\hat{a}_+^\dagger \hat{a}_+ - \hat{a}_-^\dagger \hat{a}_-) \end{aligned} \tag{2.15}$$

Eq. (2.15) can be written in the compact form of $\hat{S}_i = (\hat{a}_+^\dagger, \hat{a}_-^\dagger)\sigma_i(\hat{a}_+, \hat{a}_-)^T$ where σ_i are the Pauli matrices. From this definition it becomes clear that the Stokes operators obey angular momentum commutation relations $[\hat{S}_x, \hat{S}_y] = i\hat{S}_z$ and cyclic permutations. The operator $\hat{S}_0$ commutes with all the other components of $\mathbf{S}$. The non-vanishing commutator of the Stokes operators leads to a Heisenberg uncertainty principle like for the light polarizations. The corresponding uncertainty relation is

$$\mathrm{var}(\hat{S}_i)\mathrm{var}(\hat{S}_j) \geq \langle \hat{S}_k \rangle^2 / 4 \tag{2.16}$$

We will use linearly-polarized photonic states in which the $\hat{S}_x$ component dominates, with expectation value $\langle \hat{S}_x \rangle = N_L/2$, where N_L is the total number of photons in the pulse. From Eq. (2.16) and assuming equal uncertainties in the other Stokes operators, what defines a coherent polarization state, we find

$$\mathrm{var}(\hat{S}_y) = \mathrm{var}(\hat{S}_z) = N_L/4 \tag{2.17}$$

In analogy with the atomic projection noise, when a pulse of light polarized into one of the Stokes component is measured in an orthogonal basis the measurement outcome will be random. The random flips of the spin components leads to the light shot-noise.

As for the atomic angular momentum, the light spin state can be represented as a vector pointing on a sphere, the Poincarè sphere.

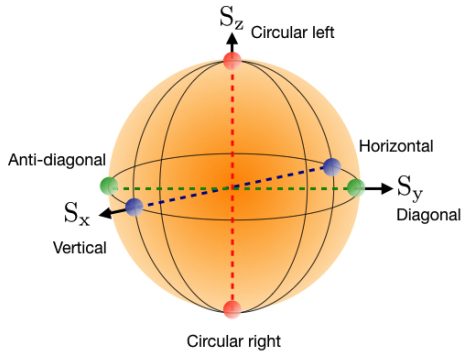

Figure 2.4: The Poincarè sphere for representing light polarization.

2.4 Interaction Between Atomic Spins and Polarized Light

In this section we briefly describe the light-atom interaction. We start the discussion with non-formal but intuitive description of the interaction based on symmetry arguments. We then present the interaction Hamiltonian and describe its main characteristics.

2.4.1 Pictorial description

We introduce the interaction of polarized light with an atomic ensemble of atoms. Consider the D_2 line transition of ^{87}Rb , we detune a probe laser by an amount Δ

to the transition between the $f = 1 \rightarrow f' = 0$, see Fig. 2.5 (b). The polarization of the laser light will change as it interacts with the atomic sample. If the detuning is large enough we can neglect absorption effects compared to dispersion due to their different scaling with detuning, respectively, $1/\Delta^2$ and $1/\Delta$. Dispersion effects change the polarization state of light if the index of refraction is different for two orthogonal polarization components, i.e. if the sample is birefringent.

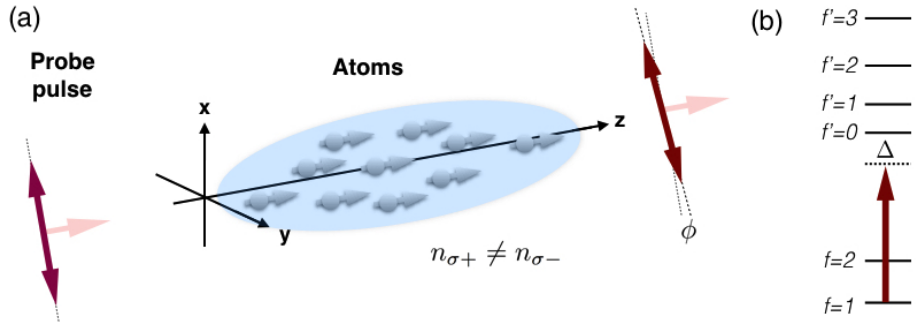

Figure 2.5: (a) Spins oriented along the propagation direction might show circular birefringence where $n_{\sigma+} \neq n_{\sigma-}$. A linearly polarized pulse will have rotated its polarization direction at the output of the atomic cloud. (b) Detuning a laser from the $f = 1 \rightarrow f' = 0$ on the D_2 line of ^{87}Rb produces this interaction.

Fig. 2.5 (a) shows a pulse of light propagating along the z-axis through an atomic sample consisting of atoms spin polarized along the same z-direction. Intuitively, the refractive index $n_x = n_y = n_{\pi/4} = n_{-\pi/4}$ since there is no preferred direction in the xy-plane. But the situation is different for z. Classically, spins polarized along the z-axis can be described as charged particle rotating around the axis. We can decompose the linear polarization of the probe into two circular polarizations components with opposite rotation direction, σ_+ and σ_- parts. If the medium has circular birefringence, i.e., $n_{\sigma+} \neq n_{\sigma-}$, the two circular components describing the linearly polarized light would acquire different phase shifts and the light at the output of the media would have its polarization direction rotated around the z-axis. More formally, it rotates the $\hat{S}_\mathrm{x}$ and $\hat{S}_\mathrm{y}$ components about the z-axis but preserves the total number of photons. This effect, the rotation of the polarization direction of a light beam due to interaction with a birefringent medium is known as Faraday rotation (Hammerer et al., 2010; Budker et al., 2002).

2.4.2 Dipole interaction

It is beyond the scope of this thesis to describe the dipole interaction theory in detail. Good references for a explanation are (Geremia et al., 2006; de Echaniz et al., 2008; Kupriyanov et al., 2005; Hammerer et al., 2010). In the following we will briefly summarize the logic behind the formidable algebraic work to present the interaction Hamiltonian in its final form.

To describe the interaction of the light field with the atoms we assume that the interaction is a small perturbation of the Hamiltonian describing the atomic free evolution (Sakurai, 1994),

$$\hat{H} = \hat{H}_{\mathrm{A}} + \hat{H}_{\mathrm{int}}. \tag{2.18}$$

The first term is the Hamiltonian describing the free evolution of the atoms and can be written as (Marlan O. Scully, 1997)

$$\hat{H}_{\mathrm{A}} = \hbar \sum_{i=1}^{\infty} \omega_i |\psi_i\rangle\langle\psi_i| \tag{2.19}$$

where $\hbar\omega_i$ are energy-eigenvalues and $|\psi_i\rangle$ the corresponding energy-eigenstates. It also includes the energy of the light field described by the single mode quantum field of Eq. (2.10). The second term in Eq. (2.18) describes the atom-light dipole interaction

$$\hat{H}_{\mathrm{int}} = -\hat{\mathbf{d}} \cdot \hat{\mathbf{E}} \tag{2.20}$$

As described by several authors (Geremia et al., 2006; de Echaniz et al., 2008; Hammerer et al., 2010), a second order perturbation theory known as adiabatic elimination can be applied when the laser probe is sufficiently far of resonance from the D_1 or D_2 line. It assumes that one excited state couples two ground states via photon scattering. The excited state is virtual, i.e., never populated, but the interaction causes a change on the field that is depends on of the spin-state and a change in the atoms that dependents of the light shift. Under such approximations, a light probe pulse of duration τ interacts with the collective atomic ensemble according to the Hamiltonian

$$\begin{aligned}\tau\hat{H}_{\mathrm{int}} = {} & g_1 \hat{S}_{\mathrm{z}} \hat{F}_{\mathrm{z}} \\ & + g_2 \left(\hat{S}_{\mathrm{x}}(\hat{F}_{\mathrm{x}}^2 - \hat{F}_{\mathrm{y}}^2) + \hat{S}_{\mathrm{y}}(\hat{F}_{\mathrm{x}}\hat{F}_{\mathrm{y}} + \hat{F}_{\mathrm{y}}\hat{F}_{\mathrm{x}}) + \frac{1}{\sqrt{3}} \hat{S}_0 (2\hat{F}_{\mathrm{z}}^2 - \hat{F}_{\mathrm{y}}^2 - \hat{F}_{\mathrm{x}}^2) \right)\end{aligned} \tag{2.21}$$

where g_1 and g_2 are light-atom coupling constants proportional to the vector $\alpha^{(1)}$ and tensor $\alpha^{(2)}$ polarizability components. As described in (de Echaniz et al.,

2005), the coupling constants g_i can be described as

$$g_i = \alpha_0 \mathfrak{g} \sum_{F'} \frac{\alpha^{(i)}_{F,\ F'}}{\Delta_{F,\ F'}} \tag{2.22}$$

where $\alpha^{(i)}_{F,\ F'}$ is the rank-i unit-less polarization coefficient of the $F \to F'$ transition, and

$$\begin{aligned} \alpha_0 &= \frac{3\epsilon_0 \hbar \Gamma \lambda_0^3}{8\pi^2} \\ \mathfrak{g} &= \frac{\omega_0}{2\epsilon_0 V} \end{aligned} \tag{2.23}$$

with Γ being the spontaneous decay rate, $\lambda_0(\omega_0)$ the transition wavelength (frequency) and V is the interaction volume. The magnitude of the coupling constant g_1 and g_2 depend differently on the probe detuning with $g_1 \propto \frac{1}{\Delta}$ and $g_2 \propto \frac{1}{\Delta^2}$ giving rise to a variety of dynamics (de Echaniz et al., 2008).

In the interaction Hamiltonian Eq.(2.21) the scalar coefficient has been ignored. It introduces a shift on the atomic energy levels by an amount proportional to the probe intensity, but has no effect on the dynamics of the atomic spins or optical polarization. The vector term is responsible for the Faraday rotation signal. It couples the circular polarization of the probe light to the collective spin component along the light's propagation direction. This interaction generates correlations between the atoms and the light. The tensor component, in turn, induces nonlinear dynamics on the internal state of the atomic spins.

Even though the tensorial term is smaller, this term is not negligible over the interaction time scale needed to produce spin squeezing. Different probing schemes have been proposed and implemented to minimize the nuisance introduced by the tensorial term. One of them consists of applying two probe pulses with different frequency detuned from the D_1 and D_2 lines to cancel the tensorial component but without affecting the vector term (Appel et al., 2009). A different method is to use probe pulses with alternating polarization, i.e., intercalate pulses with orthogonal polarizations in such a way that each pulse cancels the tensorial rotation introduced by the previous pulse. This probing scheme is known as dynamical decoupling (Koschorreck et al., 2010b). Yet there is a third probing scheme, called magic angle probing, where a bias field is applied in a particular angle and direction with respect to the probe beam propagation (Smith et al., 2004). However, in this work we follow a different approach. It based on a modulated probing scheme where the spins precess under an external magnetic field. The same spin component is stroboscopically measured at π-phase difference achieving back-action evasion. In Sec 2.5.2 we present it in more detail.

2.5 QND Interaction

In this section we describe the quantum non-demolition (QND) characteristics of the interaction Hamiltonian described in Eq. (2.21) and discuss how to exploit it to produce useful spin squeezed states for metrology.

In a QND measurement, a *system* $\mathfrak{S}$ and a *meter* $\mathfrak{M}$ interact through $\hat{H}_{\rm int}$ and end-up entangled. Because system and meter are entangled, $\mathfrak{S}$ and $\mathfrak{M}$ carry information about themselves but also about the other party. By a subsequent classical measurement on the meter, generally destructive, the imprinted information about the system variable can be harnessed. The basic requirement that a measurement needs to fulfill in order to be named as QND is the availability of a variable to be measured repeatedly giving predictable results.

$$[\hat{O}(t), \hat{O}(t')] = 0 \tag{2.24}$$

Clearly, constants of the motion are QND observables. But they are not the only variables that can be measured by means of QND measurements. Furthermore, the coupling between meter and system should not feed-back fluctuations into the QND variable of the system. In order to avoid this it is sufficient that the QND variable $\hat{O}$ commutes with the interaction Hamiltonian of the system and the meter

$$[\hat{O}, \hat{H}_{\rm int}] = 0 \tag{2.25}$$

This condition is known as the back-action evasion criterion.

Eq's (2.24) and (2.25) are formal expressions that an operator must fulfill in order to be QND. However, as described in (Holland et al., 1990; Poizat, J. Ph. et al., 1994), in practical applications there are some extra requirements that a QND observable must accomplish. An equivalent description of quantum non-demolition measurements on spin systems can be found in (Mitchell et al., 2012). For the experimental set-up used in this thesis, the experimental verification of the QND interaction is described in (Sewell et al., 2013).

2.5.1 Implementation of QND measurements

Neglecting the tensorial light-shifts caused by the probe, the light atom interaction Hamiltonian described in Eq. (2.21) becomes

$$\tau \hat{H}_{\rm int} = g_1 \hat{S}_{\rm z} \hat{F}_{\rm z} \tag{2.26}$$

To study the evolution of the light and atomic operators we use the Heisenberg equation of motion in the Heisenberg picture

$$\frac{d\hat{O}}{dt} = \frac{1}{i}[\hat{O}, \hat{H}_{\rm int}] \tag{2.27}$$

This gives simple input-output relations between operators before and after the interaction, labelled (in) and (out), up to first order in the interaction time τ, obtaining

$$\begin{aligned} \hat{F}_{\mathrm{x}}^{(\mathrm{out})} &= \hat{F}_{\mathrm{x}}^{(\mathrm{in})} - g_1 \hat{S}_{\mathrm{z}}^{(\mathrm{in})} \hat{F}_{\mathrm{y}}^{(\mathrm{in})} & \hat{S}_{\mathrm{x}}^{(\mathrm{out})} &= \hat{S}_{\mathrm{x}}^{(\mathrm{in})} - g_1 \hat{S}_{\mathrm{y}}^{(\mathrm{in})} \hat{F}_{\mathrm{z}}^{(\mathrm{in})} \\ \hat{F}_{\mathrm{y}}^{(\mathrm{out})} &= \hat{F}_{\mathrm{y}}^{(\mathrm{in})} + g_1 \hat{S}_{\mathrm{z}}^{(\mathrm{in})} \hat{F}_{\mathrm{x}}^{(\mathrm{in})} & \hat{S}_{\mathrm{y}}^{(\mathrm{out})} &= \hat{S}_{\mathrm{y}}^{(\mathrm{in})} + g_1 \hat{S}_{\mathrm{x}}^{(\mathrm{in})} \hat{F}_{\mathrm{z}}^{(\mathrm{in})} \\ \hat{F}_{\mathrm{z}}^{(\mathrm{out})} &= \hat{F}_{\mathrm{z}}^{(\mathrm{in})} & \hat{S}_{\mathrm{z}}^{(\mathrm{out})} &= \hat{S}_{\mathrm{z}}^{(\mathrm{in})} \end{aligned} \tag{2.28}$$

from which we can conclude that $\hat{S}_{\mathrm{z}}$ and $\hat{F}_{\mathrm{z}}$ are QND observables. A complete symmetry between light and atoms is noticeable. As previously described, Eq.'s (2.28) demonstrate that two systems contain information about the other part.

2.5.2 Stroboscopic QND measurements

In the experiments described in this thesis we apply periodically modulated Faraday measurements to achieve back-action evading QND measurements. We prepare the atoms in a CSS with angular momentum along the y-axis, under a parallel bias magnetic field. The magnetic field causes the spin orientation F_{y} to be fixed, but the spin uncertainty distribution to precess, so the noise in F_{z} coherently evolve to noise in F_{x} and vice-versa.

Despite the fact that F_{z} is a dynamical variable it is possible to measure it using a QND scheme. First, we notice that in light of Eq. (2.25), measurements of the F_{z} component are back-action evading. This is to say that it is possible to obtain information about the F_{z} without disturbing it. Furthermore, since the F_{z} variable is not changed, repeated measurements of it will commute, Eq. (2.24). An ideal QND measurement as described by Eq. (2.26), combined with periodic measurements of the same component can surpassed the standard quantum limit. This was proposed in the late 70's in the context of gravitational wave detection (Thorne et al., 1978; Braginsky et al., 1980).

However, the atom-light interaction Hamiltonian includes an additional term in addition to the simple QND interaction, Eq. (2.21). In order to cancel the tensorial rotation induced by the probe the measurement needs alternate between measuring $+F_{\mathrm{z}}$ and $-F_{\mathrm{z}}$. Each individual measurement produces the undesired tensorial rotation but in opposite directions. Consecutive probe pulses sent at times such that they are measuring $\pm F_{\mathrm{z}}$ produce coherent back-action effects that cancel each other. As a result, the combined pulses achieve back-action evasion. A proof is presented in **Appendix A**.

2.5.3 Conditional spin squeezing

We have seen that an interaction Hamiltonian of the type described in Eq. (2.26) allows QND measurements of the atomic spins via dispersive probing. Here we will explain the role of QND measurements in the production of spin squeezed states.

From Eq. (2.28) we see that the interaction transfers information from $\hat{F}_\mathrm{z}$ to $\hat{S}_\mathrm{y}$. The variance of the measurement outcome is

$$\begin{aligned}\mathrm{var}(\hat{S}_\mathrm{y}^{(\mathrm{out})}) &= \mathrm{var}(\hat{S}_\mathrm{y}^{(\mathrm{in})}) + \tilde{g}_1^2 \mathrm{var}(\hat{S}_\mathrm{x}^{(\mathrm{in})}\hat{F}_\mathrm{z}^{(\mathrm{in})}) \\ &\approx \mathrm{var}(\hat{S}_\mathrm{y}^{(\mathrm{in})}) + \tilde{g}_1^2 \langle \hat{S}_\mathrm{x}^{(\mathrm{in})}\rangle^2 \mathrm{var}(\hat{F}_\mathrm{z}^{(\mathrm{in})})\end{aligned} \tag{2.29}$$

where we used the fact that $\hat{S}_\mathrm{y}$ and $\hat{F}_\mathrm{z}$ are uncorrelated before the interaction, assumed that $\langle \hat{S}_\mathrm{x}^{(\mathrm{in})}\rangle^2 \gg \mathrm{var}(\hat{S}_\mathrm{x})$, which is the case for an input coherent state with many photons, polarized in the H or V direction, and and we have dropped higher order terms. The symbol $\tilde{g}_1$ differentiates from g_1 as the former deals with noise properties of the measurement and the later with mean values. Only in the case where the light-atom coupling is homogeneous the two quantities are equal. In all the other cases the two coupling constant must be measured independently. The effect of non-homogenous matching between the atomic sample and the probe light and its effect on the light-atom interaction were recognized early and have been approached theoretically (Müller et al., 2005) and experimentally on the first spin squeezing experiments (Appel et al., 2009). The coupling inhomogeneity has become more relevant nowadays with the current state-of-the-art reported values of squeezing since they are enhanced by a cavity surrounding the atomic ensemble (Schleier-Smith et al., 2010a; Bohnet et al., 2014; Baragiola et al., 2014; Hosten et al., 2016b).

We will come to this point later on when describing the experimental setup in **Chapter 3**, where we will describe how we calibrate the mean coupling constant described by Eq. (2.28), and also when talking about the squeezing results in **Chapter 6**, where we experimentally find the constant of proportionality for the quantum noise described by Eq. (2.29).

The first term of Eq. (2.29) describes the noise in the light meter while the second terms expresses the phase fluctuations introduced by the atomic projection noise. We define the signal-to-noise ratio of the QND measurement as the quotient of the atomic and light noises,

$$\kappa^2 \equiv \frac{\tilde{g}_1^2 \langle \hat{S}_\mathrm{x}^{(\mathrm{in})}\rangle^2 \mathrm{var}(\hat{F}_\mathrm{z}^{(\mathrm{in})})}{\mathrm{var}(\hat{S}_\mathrm{y}^{(\mathrm{in})})} = \tilde{g}_1^2 \frac{N_\mathrm{A} N_\mathrm{L}}{2} \tag{2.30}$$

assuming that both the light and atomic systems are quantum noise limited as

described in Eq. (2.17) and Eq. (2.5). This allows us to re-write Eq. (2.29) as

$$\mathrm{var}(\hat{S}_{\mathrm{y}}^{(\mathrm{out})}) = (1+\kappa^2)\mathrm{var}(\hat{S}_{\mathrm{y}}^{(\mathrm{in})}) \tag{2.31}$$

At the same time, the atomic state is also affected by the QND interaction. As shown by several author (Hammerer et al., 2004, 2010), the change in $\mathrm{var}(\hat{F}_{\mathrm{z}})$ by the QND measurement conditioned to the measurement outcome $\hat{S}_{\mathrm{y}}^{(\mathrm{out})}$ is

$$\mathrm{var}(\hat{F}_{\mathrm{z}}^{(\mathrm{out})}|\hat{S}_{\mathrm{y}}^{(\mathrm{out})}) = \frac{1}{1+\kappa^2}\mathrm{var}(\hat{F}_{\mathrm{z}}^{(\mathrm{in})}) \tag{2.32}$$

The above equations confirms that a QND interaction of a meter with a system as described in Eq. (2.26) followed by a destructive detection of the meter produces a change in the system, leaving it in a state with reduced uncertainty.

Although a single measurement is enough to project the atomic state into a squeezed state, verification of the squeezing requires the use of two pulses. The first QND measurement reduces the atomic noise of the measured component while the second measurement is used to evaluate the correlation between them. The conditional variance between the two measurements tells how much variance is left if we use the first measurement to *predict* the second. The measurement noise reduction is quantified by

$$\mathrm{var}(\mathcal{M}_2|\mathcal{M}_1) = \mathrm{var}(\mathcal{M}_2 - \chi\mathcal{M}_1) \tag{2.33}$$

where the degree of correlation is quantified by the coefficient χ, which minimizes Eq. (2.33), defined as

$$\chi \equiv \frac{\mathrm{cov}(\mathcal{M}_1, \mathcal{M}_2)}{\mathrm{var}(\mathcal{M}_2)} \tag{2.34}$$

where $\mathcal{M}_1$ ($\mathcal{M}_2$) are the measurement outputs of the first (second) measurement of the meter $\mathfrak{M}$. The covariance between the measurements is defined as $\mathrm{cov}(\mathcal{M}_1, \mathcal{M}_2) = \frac{\langle \mathcal{M}_1\mathcal{M}_2\rangle + \langle \mathcal{M}_2\mathcal{M}_1\rangle}{2} - \langle \mathcal{M}_1\rangle\langle \mathcal{M}_2\rangle$.

The measurement outputs $\mathcal{M}_i$ include noise both light shot noise and atomic noise, see Eq. (2.29). As we use the atoms as sensors, the light shot noise is inherent in the measurement. It is possible to account for it be repeating the measurement without atoms in the trap, and subtract it from the measured noise if we are interested in the atomic squeezed state characteristics.

For the judgment on the metrological relevance of the spin squeezing we use the conditional spin variance Eq. (2.33) in an expression similar to the Wineland squeezing criteria Eq. (2.9)

$$\xi_m^2 = \frac{1}{\eta^2}\frac{\mathrm{var}(\mathcal{M}_2|\mathcal{M}_1)}{\mathrm{var}(\mathcal{M}_1)} \tag{2.35}$$

again, $\xi_m^2 < 1$ indicates metrological advantage and includes the readout noise. Spin squeezing depends not only on the projection noise suppression but also on the preservation of atomic coherence, so the signal-to-noise ratio is improved. η accounts for the coherence loss of the measured state.

"You can only live in the world you ken. The rest is just wishful thinking or paranoia"

Irvine Welsh, *Filth*

3 Experimental setup

In this chapter, I describe the apparatus used to perform the experiments discussed later in the thesis. Before describing the experiment as such, I will briefly offer an overview of the trap's history and the people who worked with it. Next, I present the technical details of the apparatus necessary to understand its working principle, including modifications and improvements on the setup done during my PhD. The cooling and trapping details as well as a deeper description of the technical aspects can be found in several previous doctoral theses (Schulz, 2002; Crepaz, 2006; Kubasik, 2009; Koschorreck, 2010). Afterwards, I describe one of the important properties of our experiment, the capability to prepare the atoms in different states by using optical pumping from different directions. In the last section of this chapter, I will describe the absorption imaging technique used to calibrate the strength of atom-light interaction and estimate the atomic cloud size.

3.1 Brief History of the Apparatus

The machine we work(ed) with in the lab has had a long scientific path since its beginning. The vacuum system was physically moved twice, first from Innsbruck to Barcelona and later from Barcelona to ICFO's actual location in Castelldefels.

Many people has worked with it. Matthias Schulz and Herbert Crepaz built the vacuum system and the two magneto-optical traps and are the references for

the technical questions about the system. Originally the experiment was designed to trap individual atoms. Once the experiment was established at ICFO, Marcin Kubasik changed the dipole trap optics for trapping an atomic ensemble and developed the optical pumping with which he demonstrated a good state preparation. Marco Koschorreck implemented a two-polarization probing scheme with which he achieved squeezing. He developed the absorption imaging system and improved the atomic coherence time by means of magnetic field gradient compensation. Brice Dubost developed a two direction optical pumping scheme, parallel and antiparallel to the trap axis, used to prepare a non-Gaussian state. Mario Napolitano, with whom I overlapped for short time, used the nonlinear optical interactions in a cold atomic ensemble to implement a nonlinear spin measurement. Mario's work showed that the for interacting particles the "Heisenberg limit" no longer holds. Naeimeh Behbood implemented the off-axis optical pumping and upgraded the experiment capabilities demonstrating real-time feedback on the atomic state. Starting from a thermal spin state she generated a macroscopic singlet state, a state with the three spin components simultaneously squeezed. Giorgio Colangelo, with whom I shared most of my time during the PhD, demonstrated simultaneous tracking of spin angle and amplitude beyond classical limits.

3.2 Description of the Cold Atoms Apparatus

The main part of the experimental setup consists of a double stage magneto-optical trap (MOT). A two-dimensional MOT collects atoms from the background in a region with higher pressure, $\approx 10^{-8}$ mbar. Atoms accumulated in the two-dimensional MOT feed a three-dimensional MOT in a chamber having lower pressure. The two regions of the vacuum chamber are kept at different pressure by differential pumping. The atoms are transferred by a "pushing" beam along the untrapped direction. The power of the push-beam is of the most importance in the loading rate of the 3D MOT, typically of few 10^7 atoms per second. In the 3D MOT we have a very pure vacuum of $< 10^{-11}$ mbar background pressure. The MOT temperature is fixed by the spontaneous decay rate of the excited level, $\Gamma \approx 2\pi \times 6 \times 10^6\,\mathrm{s}^{-1}$, corresponding to the Doppler limited temperature of 146 µK.

The atoms are transferred from the MOT to a far off resonant dipole trap (FORT). The electric dipole interaction of the atoms with the dipole trap changes the ground state energy of atoms, effect referred as ac-Stark shift (Davidson et al., 1995). The optical trap is created by a gaussian beam gently focused to a waist diameter of 54 µm and an optical power of 6 W at a laser wavelength of 1064 nm, which creates a potential depth of $\approx$200 µK. Since the gaussian beam has a non-uniform intensity distribution it creates a gradient of intensity of the electric field vector that translates into a dipole force caused by position dependent light shift.

As the trap is red detuned the atoms are attracted towards the focus of the beam. A schematic of the optics setup is shown in Fig. 3.1.

We cool the atoms below the Doppler limit to increase the number of atoms in the trap using polarization gradient cooling (Metcalf and van der Straten, 1999; Koschorreck, 2010). This is achieved by increasing the detuning of the cooler laser from 2Γ to 15Γ in the last milli-seconds of the MOT loading while also the repumper laser power is reduced to let the atoms accumulate into the lower energy ground state $F = 1$. During this stage the quadrupole coils are switched off achieving a pure molasses phase. The temperature is then lowered down to almost 16 µK, and around 10% of the atoms are transferred into the dipole trap and the laser of the MOT are switched off.

In an optimized working regime, two seconds of loading the MOTs are enough to trap more than a million and a half atoms in the FORT. Confining the atoms in the dipole trap has several advantages: first, this trap geometry produces a large atom-light interaction for light propagating along the trap axis. Second, it allows long coherence time of the atomic state. Finally, a long lifetime of the atoms in the dipole trap, >20 s, allows the possibility to repeat experiments without the need of recapturing atoms.

3.2.1 Laser system

In this section we summarize the most important properties of the lasers used in the experiment, and center the attention to the improvements on the existing setup. The laboratory is equipped with a total of four laser systems. All the lasers light arriving to the trapping setup is fiber coupled into single mode polarization maintaining fibers to improve the alignment stability of the trap.

MOT lasers

For the creation of the MOT two lasers are needed. The first, called cooler, is tuned slightly below the cycling transition $\mathrm{F} = 2 \rightarrow \mathrm{F}' = 3$ and it is responsible for the trapping force. The second, called repumper, brings the atoms back to the cycling transition once they have fallen to $\mathrm{F} = 1$. It is tuned close to the resonance $\mathrm{F} = 1 \rightarrow \mathrm{F}' = 2$, see Fig. 3.2.

The repumer is a commercially available diode laser (Toptica DL100) frequency stabilized to an atomic transition of ^{87}Rb by means of saturated absorption spectroscopy and provide output powers around 70 mW. It is locked to the crossover $F = 1 \rightarrow F' = 1 - 2$, and frequency shifted by ∼80 MHz with an acousto-optic modulator (AOM) to be on resonance with the $F = 1 \rightarrow F' = 2$. The average power per beam on the 2D MOT is 12 mW and 300 µW per beam on the 3D MOT.

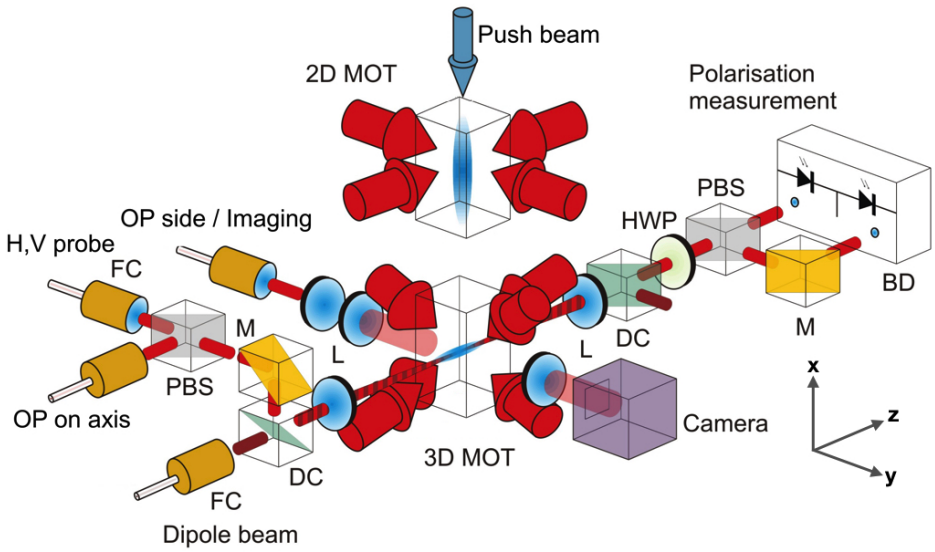

Figure 3.1: Schematic of the experiment (not to scale). A 2D MOT works as a reservoir of cold atoms where the cooling and trapping beams, shown as red arrows, collect atoms from the background and transfer them into a 3D MOT using a push beam along the direction where the atoms are not cooled. In the lower chamber the atoms are trapped by six counter-propagating laser beams. Finally the atom are held in a far off-resonant trap (FORT) produced by a high power gently focused laser beam. With the help of a CCD camera we perform absorption imaging with off-axis light to measure the number of atoms in the FORT.

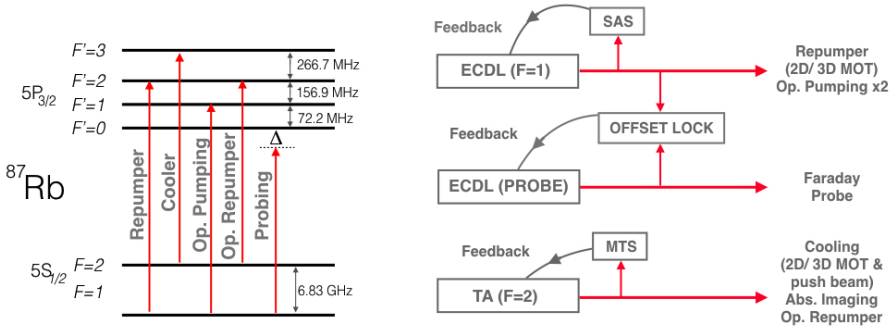

Figure 3.2: Left: ^{87}Rb D2 transition hyperfine structure with frequency splittings between the hyperfine energy level and light fields used in the experiment. Right: Laser present in the experiment, with locking strategy and tasks carried out by each laser.

Previously, the cooler laser was a Toptica DL100 with the same characteristics of the repumper laser. A part of the cooler laser was split and used to injection locked a diode laser obtaining an additional 70 mW of optical power used to feed the 2D MOT. The cooler was replaced by a diode laser and a tapered amplifier (Toptica TA 100) to increase the amount of optical power, with the aim to increase the total number of atoms in the FORT and the signal-to-noise ratio for the squeezing experiments. The Toptica TA 100 has a maximum optical power of 1 W at the output on air. To stabilize it a part of the light is split and blue shifted by 60 MHz before it enters a spectroscopy cell. In such a way the laser is locked closer to the $F' = 2$ than locking in the crossover $F' = 2 - 3$ and we have a detuning range of many natural linewidths which is important for sub-Doppler cooling. The laser is frequency stabilized using modulation-transfer-spectroscopy (MTS) (McCarron et al., 2008; de Escobar et al., 2015) at a modulation frequency of 200 kHz on top of the 60 MHz shift. The averaged power on the MOT beams is 12 mW and 30 mW for the cooler 3D and 2D, respectively, and ∼300 µW for the push beam. A change of 10% in the push beam power can lead a reduction of N_{A} by 50%.

The upgrade of the cooler laser caused a remarkable increase in the number of atoms trapped in the 3D MOT as we increased the total optical power in the cooler MOT beams. We can describe the dynamics of the number of atoms in a trap, N_{A}, either MOT or FORT by a rate equation of the form:

$$\frac{dN_{\mathrm{A}}}{dt} = L - \alpha N_{\mathrm{A}} - \beta N_{\mathrm{A}}^2 \tag{3.1}$$

where the terms with different power of N_A describe different physical mechanisms. The term without N_A is the loading rate of the trap, L. Losses due to collisions with background atoms are proportional to the number of atoms in the trap and described by the coefficient α. Light assisted collisions or two-body loses are proportional to N_A^2. There are other mechanisms like ground state collisions between cold atoms and photon reabsorption scattering which can be ignored for the conditions of our traps. We can re-write Eq. (3.1) in the form of

$$\frac{dN_A}{dt} = -\mu_0(N_A - \mu_1)(N_A - \mu_2) \tag{3.2}$$

whose solution is easier to implement as a fit function. The solution for arbitrary μ_0, μ_1 and μ_2 is

$$N_A(t) = \mu_1 + \frac{\mu_1(-\mu_1 + \mu_2)}{(\mu_1 - \mu_2 \exp^{(-\mu_1+\mu_2)t\mu_0})} \tag{3.3}$$

In Fig. 3.3 is shown the improvement in the number of atoms in the 3D MOT and in the FORT. The data is well fitted using Eq. (3.3). The fit outputs are rearranged into the more meaningfull form given in Eq. (3.1) and listed in Table 3.1.

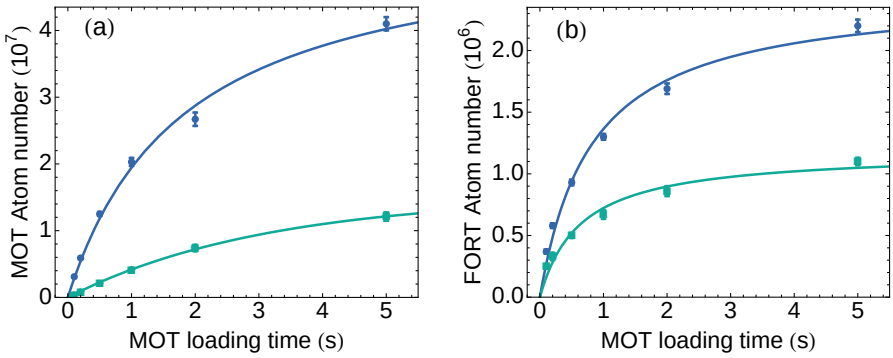

Figure 3.3: Total atom number trapped in the 3D MOT (a) and the FORT (b) as a function of the MOT loading time. Blue circles (green squares) stand for the data after (before) the upgrade of the cooler laser. Solid lines are fit using Eq. (3.3) and error bars represent $\pm 1\sigma$ standard error of the mean.

		L (10^6)	α	β (10^{-9})
After	MOT	25.4(7)	0.6(1.0)	0.02(1)
	DT	2.2(3)	1.1(2)	0.29(3)
Before	MOT	4.2(1)	0.02(1)	23.1(1)
	DT	1.3(3)	1.3(3)	1.3(3)

Table 3.1: Table with fit results using Eq. (3.3) and rearranged using the parameters of Eq. (3.1). All coefficients have units of s^{-1}.

Probing laser

The probing laser is an independent continuous wave external cavity diode laser (Toptica DL100). The beam is chopped using an AOM to create pulses of the desired length and photon number. Since the probing is done far from resonance there is no transition to lock to. The lock is done employing a beat-note locking scheme (Koschorreck, 2010). A small portion of the probe and repumper lasers, the later referenced to an atomic resonance, are split and combined on a beam splitter where a fast photo-detector detects the beat-note signal between the two lights. The detector output is fed in a phase-locked loop (PLL) circuit and used to feedback the piezo voltage and current of the probe laser to keep the frequency stabilized at a given offset from the reference laser. The PLL is programmed with a computer and the offset frequency lock runs from 300 MHz to 3 GHz, red or blue detuned. The offset lock shows a frequency drift of few MHz, making a negligible effect compared to the detuning from resonance, typically 700 MHz.

Dipole trap laser

The laser for the FORT is a Nd-YAG at 1064 nm from IPG Photonics that emits a maximum output power of 20 W in a single mode continuous wave. The trapping laser arrives to the setup through a large mode area photonic crystal fiber from NKT Photonics with a solid core of 25 µm diameter. Single mode light propagation is enabled through the photonic crystal structure surrounding the solid core in a hexagonal arrangement. The fiber coupler has a cladding mode stripper to protect the fiber. The crystal fiber is not polarization maintaining, the light polarization is adjusted before the fiber coupler with polarizarion optics, a half-wave plate (HWP) and a quarter-wave plate (QWP), and cleaned after the fiber with a polarization beam splitter (PBS). The fiber is fixed to the table to avoid changes and/or stress that would change the light polarization at the fiber's output and that will show as power fluctuations at the atoms position. The dipole trap power is controlled with an AOM, allowing fast and precise switching of powers. The overall efficiency, including AOM diffraction, coupling into fiber and losses until

the atoms position is over 50%, with typical power at the atoms location of 6 W.

It is known that displacing the focal point of the FORT with respect to the MOT center can improve the atom transfer (Kuppens et al., 2000). However, when focused with a single lens, the position of the focus and the beam waist are not independent. We improved the optical system for the dipole trap with the aim of decoupling these two quantities, the beam waist and the focal point. It consisted on a three-lens telescope made of positive lenses, see Fig. 3.4. To first order approximation, the focal length of the two outermost lenses define the magnification of the telescope, M=f_{L1}/f_{L3}. A third lens placed close to the focal plane of the other two lenses to change the beam propagation properties, being convergent (divergent) when the L2 is located closer to L1 (L3) than to the focal plane. The laser light enters the telescope through a fiber launcher from Shäfter and Kirchhoff, which has an aspheric lens with a focal lengths of 6.2 mm. The telescope lenses have been chosen for the beam input characteristics for this particular fiber launcher but also considering that the engineered beam would be focused into the vacuum chamber with an already present in the system achromat lens with focal length f =80 mm. The telescope is designed to roughly have a magnification of M=1:2 in order to be focused into a waist of $\approx$ 50 µm. The focal lengths of the lens L2 has to be smaller but comparable to the focal lengths of L1, and in order to minimize the aberrations it has to be bi-convex. The optical system has been simulated with the software OSLO, including the distance of the different optical elements in the simulations. The commercial available lenses closer to the calculated ideal telescope are provided by Melles Griot; the lens L1 is a plano-convex lens with focal length f_{L1} =25.8 mm, L2 is a bi-convex lens with focal length f_{L2} =23.9 mm and L3 is a plano-convex lens with focal length f_{L3} =51.5 mm. They three are made of fused silica and have antireflective coating for high power. In addition of the telescope, a periscope made with two dielectric mirrors allows beam walking the dipole laser.

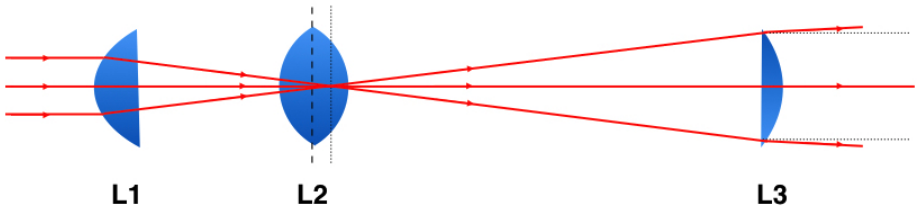

Figure 3.4: Dipole laser optical system layout to decouple beam waist and focal point. To first order approximation, the telescope composed by L1 and L3 defines the total magnification, position of L2 defines the beam propagation characteristics.

To take full advantage of the enhancement two quantities need to be optimized. One is the number of atoms trapped in the FORT, N_A; as early stated, this quantity is related to the position of the beam waist with respect to the MOT location. The other quantity is the signal from the Faraday probe and it is given by the size of the beam waist. Since the two quantities are not fully decoupled, an iterative process is needed to improve both quantities.

3.2.2 Atom-light interaction phase

The heart of the experiment is the measurement of light polarization rotations. To successfully detect these rotations it is crucial to have great control on the polarization state of the probe light. The probe light is coupled in polarization maintaining fibers and cleaned at the output to prepare the light into a high purity linear polarization using PBS with an extinction ratio of $1 : 10^6$. After the fiber output of we have a set of zero-order wave-plates to manipulate the probe light to compensate for changes down the path until it arrives to the atoms. We can set the the polarization of the probe to be linear with an extinction ratio of one part in 10^5. We also need to an accurate measurement of the number of photons arriving to the atoms. For this, we split the probe beam using a combination of HWP and a second PBS. A large fraction of the beam is directed onto a fast reference photo-detector (RD, Thorlabs PDA10A) and the rest of the beam is directed to the atoms. The RD signal is recorded on a digital storage oscilloscope (DSO, LeCroy Waverunner 64Xi) and calibrated by comparison to a power-meter placed close to the atoms position.

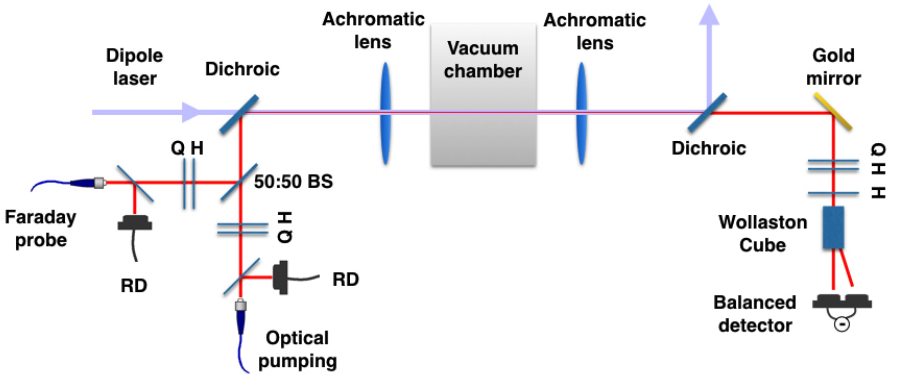

Figure 3.5: Optics layout for the detection of the Faraday rotation. Q and H stand for QWP and HWP respectively.

The probe light at 780 nm is overlapped with the dipole laser at 1064 nm on a dichroic beam splitter cube (DBS). The two co-propagating beams are gently focused into the vacuum chamber with the same 80 mm achromat lens. The focused waist of the probe beam was chosen to be ∼20 µm. The dipole beam size has a beam waist of ∼54 µm. At this value the atomic transverse size matches the probe waist, Müller et al. (2005). The two beams are re-collimated with second achromat lens after the vacuum chamber. A second DBS is used to separate the probe light from the trapping light. The dipole laser is then guided to a beam dump and the probe light is sent to a balanced photo-detector. At the detection stage we have again a set of zero-order wave-plates to compensate the birefringence introduced by the dichroic mirror. Polarization dependent losses through the optical elements must be taken into account when calculating the polarization rotation angle.

3.2.3 Shot-noise-limited polarization detection

The detection of the probe pulses is done with polarization optics and a balanced differential photo-detector, DPD, acting as a polarimeter. Light pulses propagating along the trap axis experience a polarization rotation $S_{\mathrm{y}}^{(\mathrm{out})} = S_{\mathrm{y}}^{(\mathrm{in})} \cos\phi + S_{\mathrm{x}}^{(\mathrm{in})} \sin\phi$, where $S_i^{(\mathrm{in/out})}$ are the Stokes operators before/after passing the atoms, $\phi = g_1 F_z$ is the Poincaré-sphere rotation angle, and g_1 the atom-light interaction strength factor. Detection of $S_{\mathrm{y}}^{(\mathrm{out})}$ is done with the differential photo-detector and $S_{\mathrm{x}}^{(\mathrm{in})}$ is measured by the RD.

Of the most importance in the detection system is the balanced differential photo-detector. Two different DPD have been used in this thesis. The first was designed and made in the group of Eugene Polzik at Niels Bohr Institute by Patrick Windpassinger and the second was developed during this thesis. A full chapter of this dissertation, **Chapter 4**, is devoted to explain the characteristics and properties of the latter detector, where we also compare the performance of the two photo-detectors. In the following we will briefly describe the operation principle of the former detector. Technical details about the construction and characterization of this particular detector can be found in (Windpassinger et al., 2009).

The DPD outputs the difference in photo-charges of two photo-diodes connected in series. The signal comes from an imbalance of the flux of photons reaching the two photo-diodes due to the polarization rotation of the light when interacted with the atoms. The differential signal is integrated by a low noise charge sensitive amplifier. The integrated signal is then followed by a pulse shaper where the step signal coming from the integrator is converted in a pulse approximately having a Gaussian shape. The integrator and the pulse shaper amplifiers are standard off the self components provided by Cremat Inc.

The signal of the differential detector and RD are acquired by a multi-channel DSO for later analysis. The DSO is run in segmented mode, where several trigger events are combined into one file.

3.3 Atomic State Preparation

To prepare the atoms in a desired state we use optical pumping, i.e., we send pulses of light resonant to a particular transition. The polarization of the light and its direction of propagation define the hyperfine ground state and excited state that are coupled and forbidden. States with the hyperfine ground state manifold F that cannot be excited to F' by that polarization are called dark states, and are populated by atoms decaying into the dark state by spontaneous emission. Once the atoms have fallen into the dark state they accumulate there.

We perform optical pumping on the $F = 1 \rightarrow F' = 1$ transition of the D_2 line. For the work presented here two states with macroscopic magnetization along the z and y-axes have been used, called F_z and F_y respectively. To produce the first state we send circularly polarized light along the trap axis preparing the atoms in a state where $\langle \mathbf{F} \rangle$ is along the z-axis. The F_y-polarized state is achieved by sending circularly polarized light transversally to the trap axis, i.e., along the y-axis.

The optical pumping is a cumulative process and the time needed to pump all the atoms depends on the light intensity. During the preparation some fraction of the atoms can decay into the $F = 2$ ground state. To achieve an efficient state preparation another light source is needed to recycle the atoms falling into the $F = 2$ level back to the $F = 1$ ground state. This light is called "optical repumper" and it is resonant to the $F = 2 \rightarrow F' = 2$ transition. It is addressed to the atoms from the MOT beams to ensure that all the atoms are illuminated avoiding residual population in $F = 2$. During the optical pumping process a magnetic field in the same direction of the pump beam is applied to fix the atomic spins.

The beam to produce the F_z-polarized state is co-propagating with the dipole beam and focused to a waist of 100 µm, wider than the atomic cloud to uniformly distribute the light over the cloud length. Pumping an optically thick sample can lead to shadowing effect where atoms at the beginning of the ensemble absorb all the light, and atoms at the end of the sample are not addressed by it, and so these atoms are not polarized. To prevent this from happening, the pumping intensity and duration and the optical repumper intensity as well as their frequencies have been chosen to minimize this issue. We find a good optical pumping efficiency, polarizing 99(3)% of the atoms (Koschorreck et al., 2010a), i.e., producing an state with $\langle F_z \rangle = N_A$. This value has been supported by numerical simulations done in the group (Koschorreck, 2010; Napolitano, 2014). To fully polarize the

atomic ensemble the pumping is done with a single 100 µs long pulse under bias field B_z of 100 mG. Fig. 3.6 (a) shows a characterization curve for the preparation of atoms in the F_z-state.

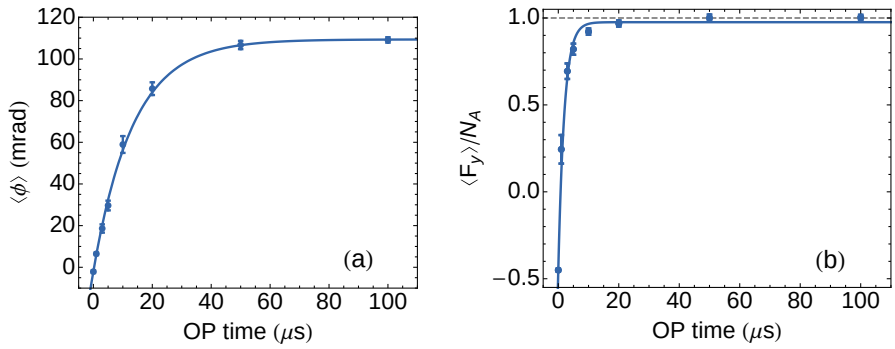

Figure 3.6: (a) Mean optical rotation angle ϕ for a state with $\langle \mathbf{F} \rangle$ along the z-axis state as a function of the optical pumping length. (b) F_y-polarized state preparation efficiency as a function of the optical pumping pulse length. The amplitude has been normalized to the total magnetization signal $\langle F_z \rangle = N_A$. Solid line are fits to the data using the function $a(1-e^{-t/\tau})+c$ from which we extract τ =13.5(7) µs (2.0(1) µs) for F_z (F_y) and an amplitude for $\langle F_y \rangle / N_A = 0.98(1)$. Error bars represent $\pm 1\sigma$ standard error of the mean.

To prepare the atoms in the F_y-polarized state, a state with $\langle \mathbf{F} \rangle$ along the y-axis, we use a large gaussian beam with a 5 mm waist and expand it horizontally using a cylindrical telescope to ∼8 mm. A perfect F_y-polarized state would give a zero average signal in the polarimeter. To measure the degree of atomic polarization we first polarize the atoms by on axis optical pumping under a B_z field and measure the coherence with the Faraday probe. We set the field along B_y and pump the atoms in F_y. The atoms are then adiabatically rotated from being polarized along the y-axis to be along z-axis by slowly rotating the magnetic field pointing. Once the atoms are along the z-axis they are probed with the Faraday probe. The amplitude of the rotated atoms is compared to the signal from the ensemble directly polarized in F_z. We observe negligible, $\lesssim 1\%$ polarization loss during the rotation. The probing scheme is illustrated in Fig. 3.7. As shown in Fig. 3.6 (b), a single pulse of 50 µs is enough to saturate the transition, demonstrating that we prepare the atoms in the F_y-polarized state with high efficiency. It is worth mentioning that the off-axis pumping has to scatter more atoms to prepare the state because the previous state was already pumped in F_z.

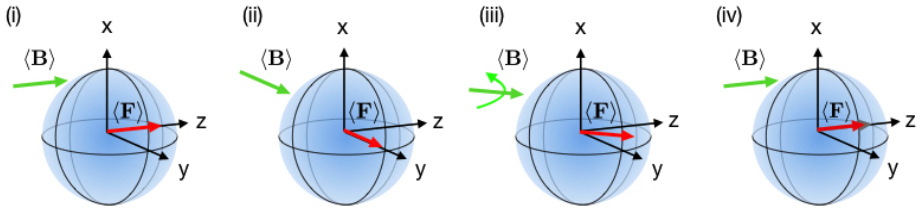

Figure 3.7: Measurement strategy to measure the amplitude of the F_y-state. (i) Initially the atoms are prepared along the z-axis under a parallel field and the coherence is measured with the Faraday probe. (ii) After, the state state is prepared along the y-axis. (iii) Then, the field is adiabatically rotated towards the z-axis and the atoms follow this rotation. (iv) Finally, the rotated state is measured using the Faraday probe and its amplitude is compared to the amplitude from the state initially prepared along F_z.

We noticed that the bias field direction can change the pumping efficiency with changes in the $\pm 2\%$ range. We empirically set the bias field that maximize the response of the atomic cloud using the Faraday rotation probe, with typical preparation efficiency of $\langle F_y \rangle \simeq 0.98 N_A$.

3.4 Characterization of the Trapped Atoms

Once the atoms have been transferred into the FORT it is necessary to study and characterize some important parameters as for example the number of atoms in the trap, the lifetime of the trapped atoms or the temperature of the atoms. In the following we describe how these quantities are measured and report the obtained values.

3.4.1 Atom number measurement

We use absorption imaging as an independent and reliable measure of the number of atoms trapped in the FORT. The technique is widely used in the field of cold and ultra-cold atomic physics (Ketterle et al., 1999). Although experimental details of have changed a bit over the course of the time, a deep description of the absorption imaging used in this set-up is present in (Koschorreck, 2010).

In short, atoms in the MOT are in a mixture of $F = 1$ and $F = 2$ ground states, and after transfer the dipole trap both states can be occupied. The relative populations depend on the amount of repumper light in the last steps of the

molasses phase, and it is optimized to maximize the atoms in $F = 1$ as it is the relevant state for the Faraday probe.

For the absorption imaging, it is necessary to move the population to $F = 2$. The atoms are transferred to $F = 2$ with a 100 µs pulse light tuned on-resonance with $F = 1 \rightarrow F' = 2$ transition and sent from the MOT beams. The imaging of the the atoms is done from the side with a 100 µs pulse of circularly polarized light resonant to the cycling transition $F = 2 \rightarrow F' = 3$. The light absorbed by the atomic cloud casts a shadow that is detected with the CCD camera, see Fig. 3.1. If the imaging light is not exactly on resonance the atomic sample would act as lens leading to image distortions which might be the source of systematic errors. After the image with the atomic shadow we collect a reference image with the same illumination conditions but without the atoms. We also take an image without the imaging light to account for and correct background light. To avoid spatially dependent light shifts the dipole trap is switched off during this process.

A difference introduced in the absorption imaging routine is the correction for the maximum observable optical depth. The atoms are allowed to expand for longer before the imaging light is sent resulting in a dilute medium, where the correction for the observable optical depth is unnecessary. The other main difference already described is the use of circularly polarized light instead of linearly polarized for the imaging as it gives a stronger signal. The new value for the scattering cross-section and current values on the imaging system can be found in (Colangelo, 2016). The statistical error in the number of atoms measured with absorption imaging is $\sim 3\%$, mainly coming from variation of the atom number in different loading events.

Interaction strength characterization

With the N_{A} independently measured by absorption imaging and the good efficiency optical pumping we can estimate the coupling constant of the interaction Hamiltonian, Eq. (2.26). The per-atom rotation is calculated from the measured rotation angle and the number of atoms by

$$g_1 = \frac{\langle \phi \rangle}{N_{\mathrm{A}}} \tag{3.4}$$

were we have assumed that the input light is completely polarized along the vertical direction, i.e., $\langle S_{\mathrm{y}}^{(\mathrm{in})} \rangle = 0$ and a full polarization of the atom, $\langle F_{\mathrm{z}} \rangle = N_{\mathrm{A}}$.

Experimentally, we load the atoms and polarize them into F_{z} as described in Sec. 3.3 of this chapter. We then probe the ensemble with the Faraday probe and obtain a mean rotation angle $\langle \phi \rangle$. After the dispersive measurement we take an absorption image of the atoms and get N_{A}. We vary the number of atoms in the dipole trap by loading the 3D MOT for different times, and repeat each

loading time to collect statistics. In Fig. 3.8 is shown a calibration plot for the g_1 coupling constant and find a value of $g_1 = 6.16(9) \times 10^{-8}$ radian·atom^{-1}.

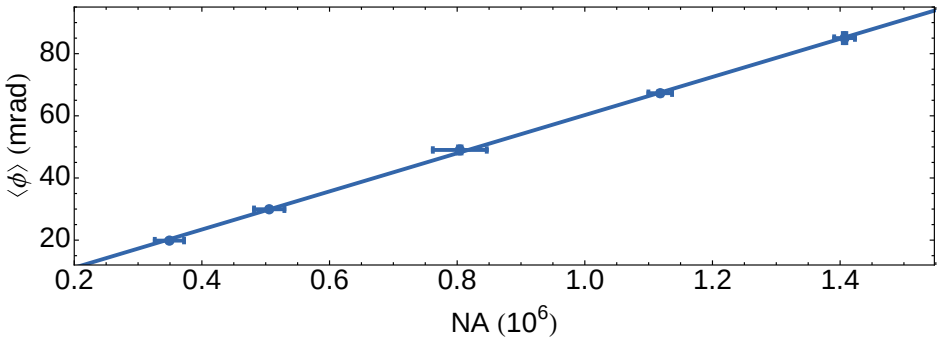

Figure 3.8: Calibration of mean Faraday rotation signal against input atom number N_A measured via absorption imaging. Solid line, the fit curve $\phi = a_0 + g_1 N_\mathrm{A}$ with values $g_1 = 6.16(9) \times 10^{-8}$ radian·atom^{-1} and $a_0 = 1.42(63) \times 10^{-3}$ radian. Error bars indicate $\pm 1\sigma$ statistical errors.

3.4.2 Atomic features

Cloud size

The shape of an atomic ensemble held in a focused single beam looks like a cigar, and its dimensions can be accurately measured. To measure the size of the atomic cloud we use the time-of-flight (TOF) technique, first applied by (Lett et al., 1989). The atoms are release from the trap and allowed to expand freely. After a variable time of expansion the atoms are measured using absorption imaging. The density distribution of the cloud is converted in a intensity distribution on the CCD.

Free, thermal and isotropic expansion of the atoms is described by (Kubasik, 2009)

$$\omega_a(t)^2 = \omega_a^2(0) + \frac{k_B T}{m}(t - t_0)^2 \tag{3.5}$$

where k_B is Boltzmann constant and m the atomic mass, known quantities. On the other hand, $\omega_a(0)$ is the initial size of the ensemble, T is the temperature of the atoms and t_0 is a time delay for switching off the dipole trap, all three quantities free parameters of the fit. The width of the radial profile is obtained by integrating each frame of the image along the longitudinal direction (the $z-$axis)

and fitting the resulting density profile with a Gaussian function to get the center and the width of the atomic ensemble. In Fig. 3.9 (a) is shown the fits to the atomic distribution for the different times used. Fitting the radial profiles versus time with Eq. (3.5) we find $\omega_a(0)$ =14.2(4) µm, from which we determine the radial full width at half maximum (FWHM) of the atomic cloud in $\rho_{radial} = 2\sqrt{2\ln 2}\ \omega_a(0)$ =33(1) µm. The width of the atomic cloud ω_a as a function of time is plotted on Fig. 3.9 (b). The time it takes the dipole trap to switch off is estimated to be t_0 =0.36(5) ms.

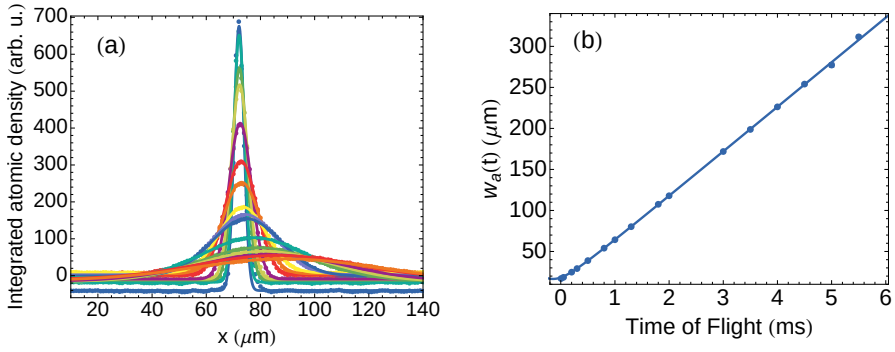

Figure 3.9: (a) Integrated density distribution and fits using a Gaussian function as a function of light time from which the center of mass positions and radial widths are obtained. (b) Characteristic transverse width of the expanding atomic cloud for different free falling times. Solid line is a fit using Eq. (3.5) used to determine the temperature of the atoms 15.5(1) µK and the transverse initial size of the ensemble $\omega_a(0)$ =14.2(4) µm. For both plots error bars would be smaller than the point and are not represented.

The axial shape of the atomic cloud does not carry as much information as the transverse dimension, but its characterization is still interesting. Unlike the transverse dimension, the axial dimension of the trap is much longer than the spread of the ensemble during the TOF, and to good approximation in $\rho_{axial}(t) \simeq \rho_{axial}(0)$. To measure its width we integrate the images along the transverse direction. A Lorentzian distribution is a good approximation to the Maxwell-Boltzmann distribution of the atoms. As can be seen in Fig. 3.10, the transverse atomic distribution has an asymmetry due to the trap loading process. We load the atoms off centre, and the atoms slowly move along the trap axis. The longitudinal trap frequency is of the order of Hz. Despite the asymmetric distribution we can accurately estimate the axial FWHM. The solid line in Fig. 3.10 is a fit with

a Lorentzian of the form $L(z) = a\rho_{axial}/2((z - z_0)^2 + (1/2\rho_{axial})^2) + b$, where ρ_{axial} is the FWHM. From the fit, we determine the axial FWHM atomic length ρ_{axial} =3.28(6) mm.

With known longitudinal and transversal dimensions we can estimate the volume of the atomic cloud. We approximate the atomic volume to an ellipsoid with semi-axis given by ρ_{axial} and ρ_{radial} and calculate its volume using $V = \frac{\pi}{6}\rho_{radial}^2\rho_{axial}$ to find the atomic volume V_{at} =1.8(1) $\times 10^{-6}$ cm^3. This will be used later in the thesis to scale the magnetic sensitivity of the atoms by its volume.

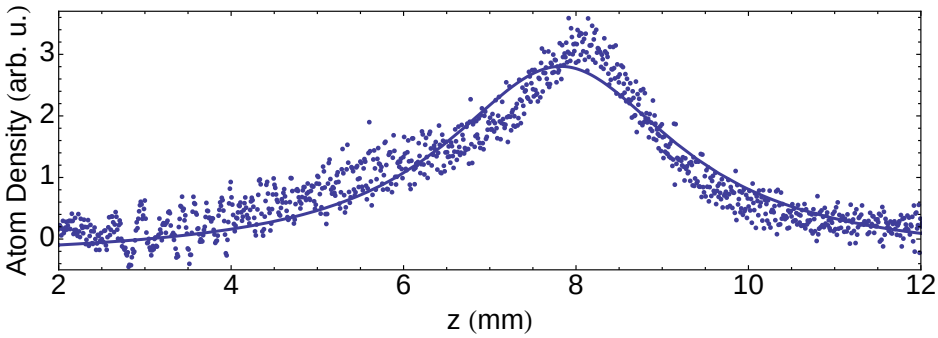

Figure 3.10: Axial shape of the atomic ensemble. The solid line is a fit with a Lorentzian function used to estimate the longitudinal FWHM ρ_{long} =3.28(6) mm.

Atom temperature

The atom's temperature can be obtained from the TOF data as it is a free parameter of the fit to the expansion of the atoms, see Eq. (3.5). The fit to the data shown in Fig. 3.9 (b) determines the temperature of the atomic sample to be 15.5(1) µK.

3.4.3 Atomic losses and depolarization

As described in the previous chapter, spin squeezing depends on the preservation of atomic coherence. There are various physical mechanisms that will reduce the number of atoms trapped in the trap and/or reduce their polarization. In the following the describe the mechanisms more relevant for our experiment.

Depolarization due to residual elliptical trapping light

An elliptical polarized component of the trapping light couple different different magnetic sub-levels m_f. Its effect is the same as the QND interaction described in Eq. (2.26). In the modifications introduced for the beam shaping of the trapping light we changed the optical elements before the QND interaction. Thus, the quality in the trapping light polarization is given by the same polarization components used previously in the experiment. Our measurements are in agreement with previously reported extinction ratios (Koschorreck, 2010), we have a mostly linearly polarized trapping laser with a circular contribution $< 10^{-5}$. As described in (Koschorreck, 2010), a completely circular polarized trapping laser will induce an energy difference between the $|1, \pm 1\rangle$ states of around 100 kHz . The expected precession frequency for the actual amount of circular polarization is in the order of $10^{-5} \times 100\,\mathrm{Hz} = 1\,\mathrm{Hz}$. We can safely neglect the effect of any residual circular polarization in the trapping laser on the atomic spin state.

Depolarization due to probing

Even though the Faraday probe is far off-resonance there is a non-zero probability for the atoms to absorb a probe photon and re-emit it. Scattered atoms out of a polarized state can return to $F = 1$ in a random m_f state, which adds noise to the atomic state, or can end up $F = 2$, where they do not contribute to the interaction and are effectively lost. For our atom-light coupling strength, squeezing is optimized with $\approx 10\%$ damage to the state (Sewell et al., 2013).

We work with an F_y-polarized state which is orthogonal to the probe axis. To measure the polarization loss caused by the probing we follow the same procedure used for the characterization of the F_y optical pumping, Fig. 3.7. We initially prepare an state with $\langle \mathbf{F} \rangle = F_\mathrm{z}$ and measure the total number of atoms in the trap N_A. We prepare the atoms in the F_y-state and measure them for a fixed time but varying the number of photons, keeping the other parameters fixed. After the *strong* probing, we adiabatically rotate the atoms to point along the z-axis and measure the remaining polarization. Comparing the initial signal with the signal after the probing for known photon number N_L, we can obtain the scattering rate per photon η_{sc} as

$$\langle F_\mathrm{y}^{(\mathrm{after})} \rangle = N_\mathrm{A} e^{-\eta_{sc} N_\mathrm{L}} + b \tag{3.6}$$

where the term b accounts for polarization offset. As explained in (Koschorreck, 2010), the measured signal is a contribution of atoms in the two hyperfine manifolds. Initially, the atoms are polarized in the $F = 1$ ground level, but due to the probing this population exponentially decays and some atoms end up in $F = 2$. The signal from atoms in $F = 2$ is smaller but it builds up at the same

rate η. As a result, there is a polarization offset. In Fig. 3.11 (a) it is shown a characterization curve from which we estimate η_{sc} =2.9(1) $\times 10^{-10}$ photons^{-1}.

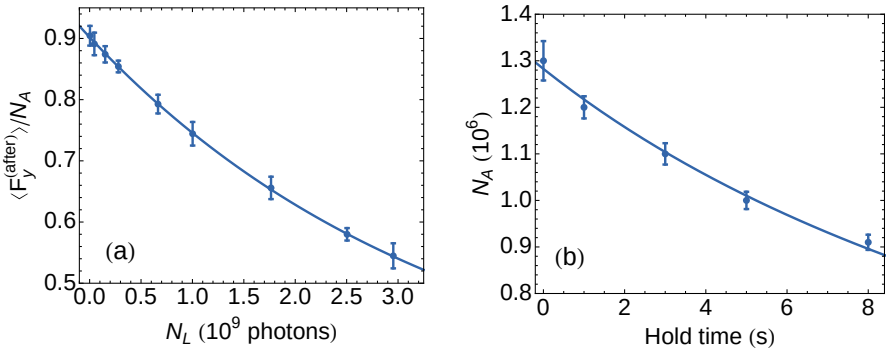

Figure 3.11: (a) Atomic loss of coherence as a function of the number of photons in the measurement. The remaining coherence of F_y has been normalized to the total atom number. Solid line is a fit with Eq. (3.6) from which we determine the scattering rate per photon η_{sc}=2.9(1) $\times 10^{-10}$ photons^{-1} (b) Number of trapped atoms as a function of trapping time. Solid line is a fit with Eq. (3.9) to obtain a lifetime of 19(1) s, text for details.

Trap lifetime

Measuring the lifetime of trapped atoms gives information about the background pressure of the vacuum system but also about the density of the atomic ensemble. As we have increased the atom number in the trap, it is worth checking if atomic collisions are now a limiting factor in the experiment. Experimentally, we load the dipole trap for one second and hold the atoms inside the dipole trap for a varying length of time before measuring N_A with absorption imaging. Analogously with the dynamics of the loading, the lifetime of trapped atoms can be described by a rate equation of form (Sofikitis et al., 2011; Kuppens et al., 2000)

$$\frac{dN(t)}{dt} = -\Gamma N - \beta N^2 \tag{3.7}$$

where the Γ term describes an exponential loss rate due to collisions of the trapped atoms with background ones and β describes losses due to collisions of trapped atoms. For our atom density, $\sim 10^{11}$ cm^{-3}, three body collisions are negligible

and we do not include them. The analytical solution of Eq. (3.7) is

$$N(t) = \frac{N_0\Gamma}{-N_0\beta + \exp(\Gamma t)(N_0\beta + \Gamma)} \tag{3.8}$$

Fitting the data with a solution to Eq. (3.8) gives a result compatible with $\Gamma = 0$, i.e., the main loss mechanism in our FORT are two-body collisions.

Having a closer look to the model, we see that it predicts a super-exponential decay for short trapping times, $t \ll 1/\Gamma$, where the fit function can be simplified as

$$N(t) \approx \frac{N_0}{1 + \beta N_0 t} \tag{3.9}$$

were, as we are in the short time, we have taken $\Gamma = 0$. Repeating the fit with the simplified equation described by Eq. (3.9) we obtain β =0.042(3) s^{-1}. From it, we determine the time needed to have half the maximum trapped population to be 19(1) s, much longer than the experiment time scale.

"What do you despise? By this are you truly known"

"Hope clouds observation"

Frank Herbert, *Dune*

4

Balanced photo-detector with real-time capabilities

In previous chapters we have described the basic principle of our measurement scheme. To extract information from a measurement a good signal-to-noise ratio (SNR) is needed. There are two obvious possibilities to improve the SNR, one is to maximize the signal, which basically means to increase the number of photons used in the measurement (for a fixed detuning and atom number, see Eq. (2.30)), and the other is trying to reduce the measurement noise as much as possible. Focusing on the latter, the minimum detectable signal of a detector is set by the electronic noise of the detector itself. Hence, reducing the electronic noise of the detector is certainly helpful.

Planned experiments (Colangelo et al., 2017b,a) required a detector with a larger dynamic range and a higher measurement bandwidth. At the same time, this was an opportunity to improve the electronic noise performance of the next generation of detectors. This chapter is the summary of the work needed for the construction and test of a new balance, differential photo-detector meeting the requirements listed above. It showed a noise equivalent charge (NEC) of 242 electrons, which reduces the shot noise limited photon number level to $N_{\mathrm{L}} \sim 10^5$.

The chapter starts out by describing the working principle of the differential photo-detector. We then move into the analysis of its noise properties in pulsed regime. Next we present a solution to access the signal of the photo-detector

in real time and show its performance. Parts of this chapter are published in (Martin Ciurana et al., 2016).

4.1 Fast, Low Noise Balanced Photo-Detector

The difference signal from two PIN photo-diodes (PDs) (Hamamatsu S3883) is obtained by connecting them in series and sensing the differential photo-charge between the diodes. To improve the response time of the photo-diodes they are reverse biased by 5 V to reduce their capacitance. The differential output current is DC coupled to the integrator, a very low noise charge-sensitive pre-amplifier (Cremat CR-110) with a capacitor C_i and a discharge resistor R_i in the feedback branch. Together these determine the relaxation time constant $\tau_\mathrm{discharge} = R_\mathrm{i}C_\mathrm{i} = 290\,\mu\mathrm{s}$ of the integrator, Fig. 4.1 (a). The response of the detector to an imbalanced signal is shown in Fig 4.1 (b). The 50 ns rise-time of the circuit is set by the capacitance of the photodiodes and the parasitic capacitance from the path between the photo-diodes and the charge-sensitive pre-amplifier, while the CR-100 itself has a nominal rise time of 7 ns. Pulses longer than the rise time will produce a ramp on the output voltage with amplitude proportional to N_diff, the difference of photon numbers on the two photodiodes. After such a pulse, the signal decays exponentially with time constant $\tau_\mathrm{discharge}$ to its initial value, see Fig 4.1 (b).

Previous differential photo-detectors used a similar circuit layout (Windpassinger et al., 2009), which was adapted from the original design of (Hansen et al., 2001). In these detectors the signal from the integrator was then fed into a pulse shaper amplifier, resulting in an output signal pulse shaped like a Gaussian function, an element not used in the design described here.

4.1.1 Detector test setup

To characterize the noise performance of the differential photo-detector DPD we use the setup shown schematically in Fig. 4.1 (a). A continuous beam from an external grating stabilized, frequency locked diode laser at 780 nm is chopped with an acousto-optic modulator (AOM) to produce pulses of desired duration and energy and coupled into a polarization maintaining optical fiber. At the output of the fiber the polarization is cleaned with a polarizing beam splitter (PBS). To monitor the power of the pulses, a large fraction of the beam is directed onto a reference photo-detector (RD) with a half-wave plate (HWP) and second PBS. The rest of the beam is split by means of a half wave plate and a Wollaston prism and each beam is focused onto one PD of the DPD. The wave-plate is adjusted to produce a zero mean signal, i.e., to balance the optical powers at the two photodiodes. We record the RD and DPD output voltages on an 8-bit digital

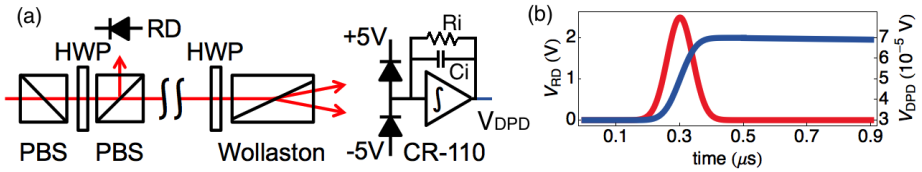

Figure 4.1: (a) Schematic of the optics and detector electronics. (b) Detector response to an imbalanced signal. Red line shows the reference detector (RD) signal and blue curve is the differential photo-detector (DPD) response, where the integrated signal rises linearly during the pulse. After the detection event the detector output decays to its initial value with a time constant of $\tau_{\text{discharge}}$ =290 µs.

storage oscilloscope (LeCroy Waverunner 64Xi) which continuously records the detector output voltage at a sampling rate of 100 Msps, asynchronously to the pulse generation.

4.1.2 Noise performance of the DPD

To characterize the noise performance of the DPD we send trains of pulses with a desired photon number N_{L}, pulse duration τ, and pulse repetition period T_{rep}. We define a single measurement for the DPD as $N_{\text{diff}} = C(\overline{V}_1 - \overline{V}_2)$, where $\overline{V}_1(\overline{V}_2)$ is the mean of N_{samp} voltage samples before (after) the optical pulse and C is a calibration factor. The number of photons N_{phot} in a pulse is estimated as $N_{\text{phot}} = C_{\text{RD}} \sum_i V_{\text{RD}}(t_i)$ where V_{RD} is the voltage output of the RD. The sum is taken over the duration of the pulse and C_{RD} is a calibration factor obtained by comparison against a power meter. For a given set of conditions, we adjust the waveplate to give a balanced signal $N_{\text{diff}} \approx 0$ and record M pulses in a single pulse train, from which we extract M values for N_{diff} and N_{phot} and compute statistics, see Fig. 4.2.

When source and detector fluctuations are taken into consideration, a linear detector will have an output signal variance given by a second-order polynomial in the average optical input energy (Bachor and Ralph, 2004),

$$\text{var}N_{\text{diff}} = a_0 N_{\text{L}}^0 + \eta N_{\text{L}} + a_2 N_{\text{L}}^2 \tag{4.1}$$

where a_0 is the "electronic noise" (EN) contribution, $a_2 N_{\text{L}}^2$ is the "technical noise" (TN) and the second term is the shot noise (SN) contribution with η the quantum efficiency of the detector. The different scalings with N_{L} allow an unambiguous identification of the different noise contributions.

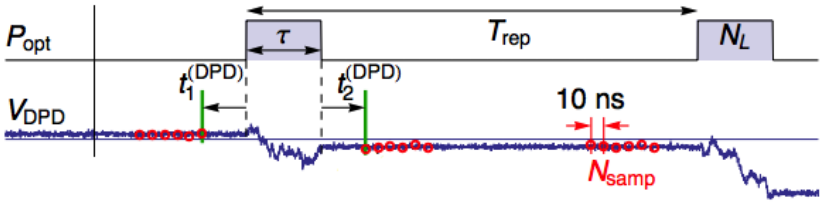

Figure 4.2: Timing diagram illustrating a possible response of the DPD to two pulses of a pulse train. P_{opt}: optical power, V_{DPD}: Balanced detector output. Red circles show oscilloscope voltage samples used to characterize the DPD noise characteristics.

To estimate the coefficients of Eq. (4.1) we collect data at a variety of pulse energy (N_{L}) in each case recording a train of 2500 pulses with repetition period $T_{\mathrm{rep}} = 0.8\,\mu\mathrm{s}$ and pulse duration $\tau = 200\,\mathrm{ns}$. Our light source is not powerful enough to measure the turning point from SN-limited to TN-limited detection. In order to measure this transition one could change τ, the probe pulse length. A more convenient way is to sum the signal from multiple pulses building a "composite pulse", i.e., a pulse containing a larger total number of photons. For a linear detection, a composite pulse will have the same information as a single higher-energy pulse (Koschorreck et al., 2010a).

The analysis parameter $\mathrm{t}_1^{(\mathrm{DPD})}$ ($\mathrm{t}_2^{(\mathrm{DPD})}$) is the time separation from the ending (beginning) of the DPD voltage samples and the start (end) of the optical pulse, see Fig. 4.2 for reference and definitions. We set $\mathrm{t}_1^{(\mathrm{DPD})} = 10\,\mathrm{ns}$ to ensure that $\overline{V}_1$ is measuring the voltage before the detection of the optical pulse. In order to determine $\mathrm{t}_2^{(\mathrm{DPD})}$ we take different values of it and fit $\mathrm{var}(N_{\mathrm{diff}})$ to obtain the corresponding fit parameters a_0, η and a_2. In Fig. 4.3 it is shown the parameter η as a function of $\mathrm{t}_2^{(\mathrm{DPD})}$. We fit η with a hyperbolic tangent to determine the minimum $\mathrm{t}_2^{(\mathrm{DPD})}$ to sample $> 99\%$ of the DPD signal and obtain $\mathrm{t}_2^{(\mathrm{DPD})} \geqslant 90\,\mathrm{ns}$.

With known analysis parameters, $\mathrm{t}_1^{(\mathrm{DPD})} = 10\,\mathrm{ns}$, $\mathrm{t}_2^{(\mathrm{DPD})} = 90\,\mathrm{ns}$ and $N_{\mathrm{samp}} = 10$ points, we fit the measured variances with Eq. (4.1) to obtain the electronic noise floor, $a_0 = 4.26(5) \times 10^5$, the shot-noise contribution, $\eta = 1.05(1)$, and the technical noise coefficient $a_2 = 2.64(1.45) \times 10^{-10}$ for the DPD. Typical results are shown in Fig. 4.4. The linear scaling of the data confirms the quantum nature of the noise. For ideal quantum noise measurements the slope should be $\eta = 1$, the discrepancy between the ideal value and the measured is coming from an error in the calibrating factor C, with difference within the $\pm 5\%$ typical error

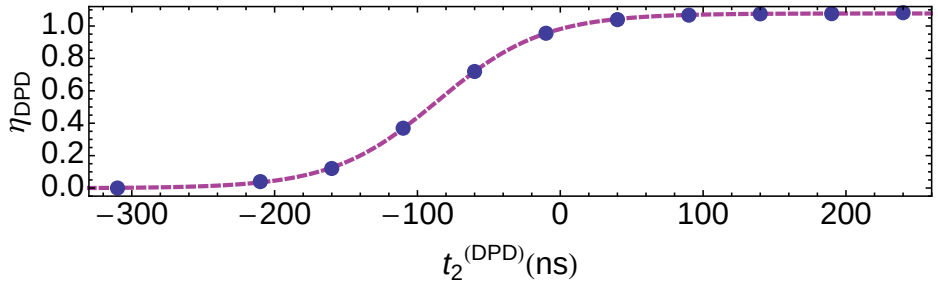

Figure 4.3: Quantum noise parameter, η, as a function of $t_2^{(DPD)}$. Dashed purple line fit using a hyperbolic tangent to determine $t_2^{(DPD)}$ >90 ns to sample > 99% of the DPD signal. Error bars are smaller than the points and are not represented.

of the power-meter used at this wavelength [1]. The detector is shot-noise limited when $a_0/\eta < N_L < \eta/a_2$. From the fit outputs, we determine that the DPD is SN-limited from $4.1(1) \times 10^5 < N_L < 4(2) \times 10^9$ photons, i.e., its SN limited behavior extends over 4 orders of magnitude.

The electronic noise of DPD contains high-bandwidth noise, e.g. Johnson noise, that can be reduced by averaging the in-principle constant output over a time window, which could be longer than the pulse itself. On the other hand, longer windows will be more sensitive to drifts and "$1/f$" noise. We investigate this trade-off by changing N_{samp} used to obtain $\overline{V}_1$ and $\overline{V}_2$ and then fit $\mathrm{var}N_{diff}^{(DPD)}$ with Eq. (4.1) to get a_0, η and a_2.

We repeat the experiment with the same pulse length $\tau = 200$ ns but a much longer probe period, $T_{rep} = 30\,\mu$s. For the analysis we use the same parameters as before, i.e., $t_1^{(DPD)} = 10$ ns and $t_2^{(DPD)} = 90$ ns. For each N_L we record more than 300 pulses in a single pulse train. From these parameters we evaluate the SN limited region of the DPD as a function of the N_{samp} used in the analysis. We fit the EN (TN) limited region $a_0/\eta < N_L$ ($N_L > \eta/a_2$) with the polynomial

$$N_L = \alpha_1 N_{samp}^{\beta_1} + \alpha_2 N_{samp}^{\beta_2} \tag{4.2}$$

where the two terms are for the two noise time-scales.

In Fig. 4.5 we observe a transition from EN $\propto N_{samp}^{\beta_1}$, where $\beta_1 < 0$ for $N_{samp} \lesssim 100$ points, describing the effects of averaging, to a $1/f$ regime for $N_{samp} \gtrsim 600$ points, with EN $\propto N_{samp}^{\beta_2}$ where $\beta_2 > 0$. The fit results are $\alpha_1^{EN} = 1.68(11) \times 10^6$,

[1] Ophir PD300. Data-sheet can be found at http://ophiropt.com/laser–measurement/sites/default/files/PD300_PD300-1W_PD300-TP_0.pdf

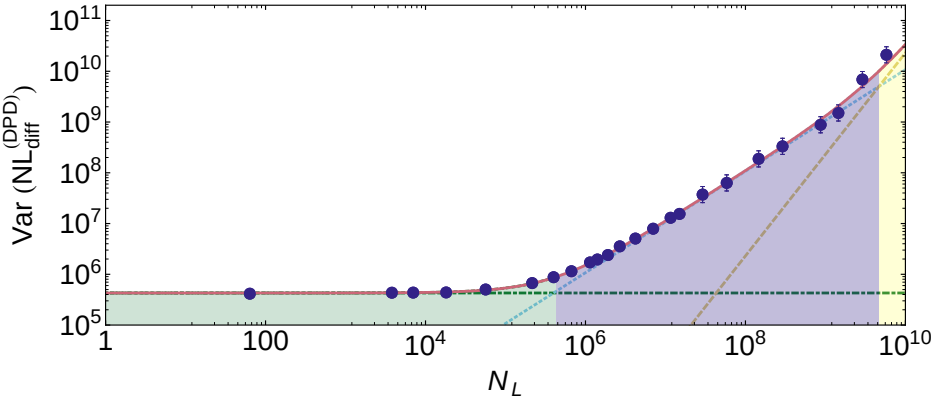

Figure 4.4: Variance of the output signal of the DPD in "balanced configuration" as function of the input photon-number in log-log scale. Solid red line fit to $\mathrm{Var}(N_{\mathrm{diff}})$ using expression Eq. (4.1). Shaded areas depicts the different detection responses: green EN-limited, blue SN-limited and yellow TN-limited. Error bars represent $\pm 1\sigma$ standard error. Broken lines represent the different contribution from EN, SN and TN.

$\alpha_2^{\mathrm{EN}} = 40(25)$, $\beta_1^{\mathrm{EN}} = -0.60(2)$ and $\beta_2^{\mathrm{EN}} = 1.08(9)$. We also notice that as shown in Fig. 4.5, increasing N_{samp} from 1 point to 400 we can reduce the electronic noise of the DPD by 10.2 dB, and that at 400 samples the DPD electronic noise is minimal. From the coefficients a_0 we can deduce the noise-equivalent charge (NEC), the number of photo-electrons necessary to create a signal equivalent to the electronic noise defined by $q_{\mathrm{SN}} = \eta_Q \sqrt{N_{\mathrm{phot,\ SN}}}$, where η_Q is the quantum efficiency of the photo-diodes. Operating at 780 nm our photo-diodes have η_Q= 0.92, resulting in a minimal NEC of 242 electrons.

Even though the EN increases for $N_{\mathrm{samp}} > 400$, the SN limited region i.e., the area between the EN and the TN curves, still increases with N_{samp} as the reduction of the TN-limited region compensates the increase of the EN. We can observe that the TN is almost flat for $N_{\mathrm{samp}} \lesssim 300$ but rapidly decreases for $N_{\mathrm{samp}} > 500$. We fit the technical noise limited region using Eq.(4.2), to find the fit parameters $\alpha_1^{\mathrm{TN}} = 1.36(56) \times 10^8$, $\alpha_2^{\mathrm{TN}} = 0.53(4.65) \times 10^3$, $\beta_1^{\mathrm{TN}} = 0.03(0.11)$ and $\beta_2^{\mathrm{TN}} = 1.99(1.31)$. Recalling the oscilloscope sample rate of 100 Msps, or 10 ns/sample, the DPD is SN-limited over measurements bandwidth running from 3 MHz to 35 kHz.

The minimum separation between consecutive pulses, or equivalently the maximum measurement bandwidth, is given the analysis parameters $\mathrm{t}_1^{(\mathrm{DPD})}$, $\mathrm{t}_2^{(\mathrm{DPD})}$

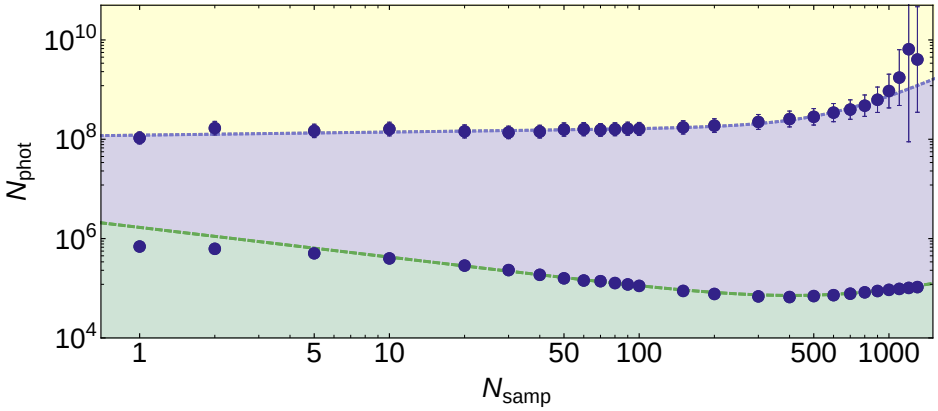

Figure 4.5: DPD SN-limited region (blue area) as function number of the oscilloscope samples used in the measurement in log-log plot. EN-limited region (green) and TN-limited (yellow), see text for details. Error bars represent $\pm 1\sigma$ standard error. Green dashed (blue dotted) curve is a fit of EN (TN) using Eq. (4.2).

and N_{samp} and the detector's rise time 50 ns, with the first found to be 10 ns and 90 ns, respectively. As clearly shown by Fig. 4.5, the measurement bandwidth and the electronic noise are closely related. The electronic noise has a minimum at $N_{\text{samp}} = 400$, or given our sampling rate, at an averaging time of 4 µs. From this we determine the minimal noise performance of our DPD to be at a measurement repetition of 125 kHz. The fastest measurement repetition occurs for minimal N_{samp}, that is $N_{\text{samp}} = 10$ ns, with a value of 6 MHz.

However, the ultimate measurement repetition is given by the detector's rise time and the shortest analysis times possible. This is to say to reduce $t_2^{(\text{DPD})}$. The effect of this will be to have a non-steady quantum noise parameter which will cause a narrowing of the shot noise limited detection range as the technical noise will increase. The minimum repetition period is given by detector rise time, 50 ns, the time parameters $t_1^{(\text{DPD})}$ and $t_2^{(\text{DPD})}$, each 10 ns, and two N_{samp}, 2×10 ns, resulting in 90 ns, or equivalently, a maximum detection bandwidth of 11 MHz, which to our knowledge makes it the fastest quantum-noise limited differential photodetector for this energy regime, i.e., for pulses with as few as 6.8×10^5 photons.

We repeat the measurement under the same scope settings to determine the electronic noise contribution of the scope itself terminating it with a 50 Ω terminator. Analogously, we vary N_{samp} to obtain $\overline{V}_1$ and $\overline{V}_2$ and fit $N_{\text{diff}}^{\text{scope}}$ with the

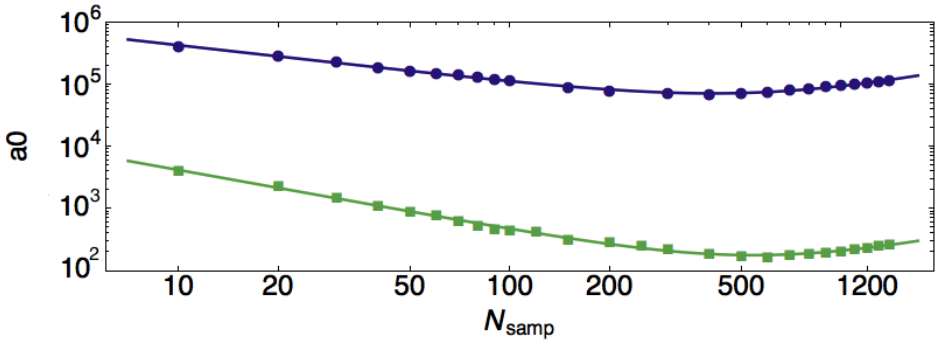

Figure 4.6: Electronics noise coefficient for the DPD (blue circles) and oscilloscope (green squares) as function of the oscilloscope samples used in the measurement in log-log plot. Solid lines are fits using Eq. (4.2). Error bars are smaller than the points and not represented.

Eq. (4.1) to find a list of scope "electronic noise" parameters a_0^{scope}. We fit a_0^{scope} with Eq. (4.2) to find the scope noise scaling parameters $\alpha_1^{\text{scope}} = 3.79(47) \times 10^4$, $\alpha_2^{\text{scope}} = 0.17(16)$, $\beta_1^{\text{scope}} = -0.96(3)$ and $\beta_2^{\text{scope}} = 0.99(13)$. From the fit outputs we conclude that it is safe to neglect the scope "electronic noise" relative to DPD electronic noise, see Fig. 4.6. The fact that $\beta_1^{\text{EN DPD}} = -0.60$ and not -1 as in the case of β_1^{scope}, means that there is some correlated noise in the DPD output signal. This is expected as the 100 MHz sampling frequency exceeds the oscilloscope input bandwidth at this setting. The measured -3 dB oscilloscope bandwidth is 30 MHz.

4.2 Real-time Detection Capability

Using the DPD requires a digital storage oscilloscope (DSO) to acquire the data for its later processing. In most experiments, the DSO is employed in segmented mode, with a specified number of time segments. Issues with digitalization noise can occur if the signals recorded at different segments have different amplitudes. Oscilloscope traces with many segments can result in a large file, and having to save and store the files in a different computer or server can slow down the repetition rate of the experiment. At the time we were testing the DPD, we just finished an experiment on real time feedback for cooling the atomic ensemble (Behbood et al., 2013a). It was based on a field-programable gate array (FPGA) that collected the RD signals and the signal from the previous differential balanced detector and calculated its ratio $\mathcal{R} = V_{\text{DPD}}/V_{\text{RD}}$ to control an

optical pumping feedback. For the feedback step the FPGA showed a latency of 11 µs for computation.

All together, these factors motivated the design and construction of a real time detection system to upgrade the experiment. It is based on standard off-the-shelf analog electronics, namely a pair of sample and hold amplifiers (SHA) and a differential amplifier (DA), and it uses the fact that the DPD output is proportional to the integral of the signal measured.

4.2.1 Principle of operation

The output from the DPD is captured by a pair of SHAs (Analog Devices AD783), gated with TTL signals. The SHA1 captures the voltage of the DPD before the optical pulse arrives, and the SHA2 captures it after the end of the pulse, analogous to $\overline{V}_1$ and $\overline{V}_2$, respectively. A differential amplifier DA (Analog Devices AD8274) amplifies the difference of the two voltages held on the SHAs.

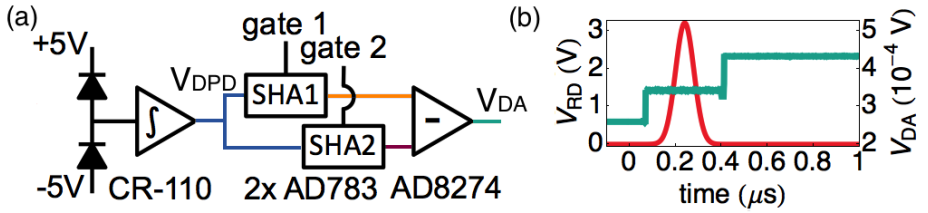

Figure 4.7: (a) Schematic of the real time detection electronics. (b) Differential amplifier (DA) response to an imbalance optical input signal. Red line shows the RD signal and green curve is the DA response. The DA outputs the difference of a pair of SHAs signals sampling the V_{DPD} output shortly before and shortly after the pulse. After the detection event the DA output stays steady.

4.2.2 Noise performance of the DA

To characterize the noise properties of the DA we repeat the same procedure as for the DPD: we record on the oscilloscope the RD and DA output voltages. The SHA1 captures $V_{\mathrm{DPD}}(t_1^{(\mathrm{gate})})$ before the optical pulse arrives, and the SHA2 captures $V_{\mathrm{DPD}}(t_2^{(\mathrm{gate})})$ after the end of the pulse, see Fig. 4.8 for reference and definitions.

We define a single measurement as $N_{\mathrm{diff}} = C'\overline{V}_{\mathrm{DA}}$, where $\overline{V}_{\mathrm{DA}}$ is the mean of N'_{samp} voltage samples a time t^{DA} after the end of the SHA2 and C' is a calibration factor obtained by comparison against a power meter. Under the

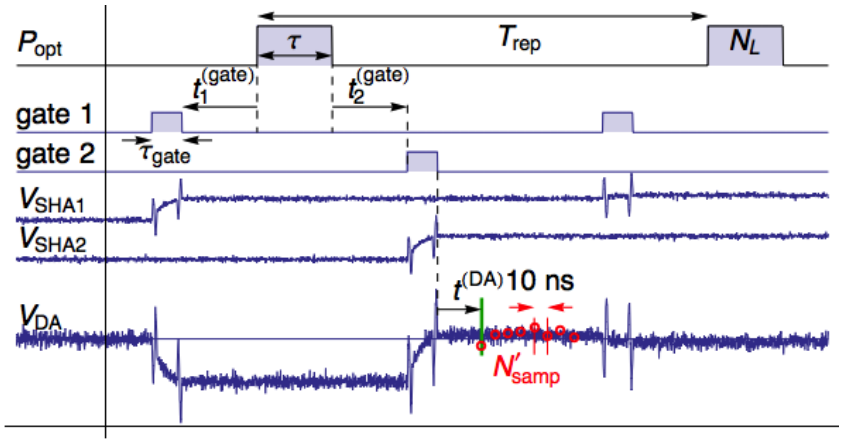

Figure 4.8: Timing diagram illustrating a possible response of the DA to two pulses of a pulse train. P_{opt}: optical power, gate 1, gate 2: gate voltages causing the respective SHAs to sample (high) and to hold (low), V_{DA}: differential amplifier output. Red circles show oscilloscope voltage samples use to characterize the DA noise characteristics.

same experimental conditions as for the DPD characterization, $T_{\mathrm{rep}} = 0.8\,\mu\mathrm{s}$ and $\tau = 200\,\mathrm{ns}$, we record a train of 2500 pulses for each value of N_{L} and fit $\mathrm{var}N_{\mathrm{diff}}^{(\mathrm{DA})}$ with Eq. (4.1) we obtain a_0, η and a_2. As before, we construct "composite pulses" to determine a_2. The SHAs are gated for $\tau_{\mathrm{gate}} = 100\,\mathrm{ns}$ at times $t_1^{(\mathrm{gate})} = 10\,\mathrm{ns}$ and $t_2^{(\mathrm{gate})} = 20\,\mathrm{ns}$. The analysis parameters are $\mathrm{t}^{\mathrm{DA}} = 170\,\mathrm{ns}$ and $N'_{\mathrm{samp}} = 10$ points.

Typical results are shown in Fig. 4.9. From the fit outputs we determine that the DA is shot-noise limited from $7.4(1) \times 10^5 < N_{\mathrm{L}} < 3.7(9) \times 10^8$ photons, i.e., over almost 3 orders of magnitude. From the coefficients a_0 we can deduce the NEC for the DA and compare to the DPD performance. For the same number of samples, $N_{\mathrm{samp}} = N'_{\mathrm{samp}} = 10$ points, we find $\mathrm{NEC}^{\mathrm{DPD}} = 600$ electrons and $\mathrm{NEC}^{\mathrm{DA}} = 808$ electrons. Since the two calibration experiments were taken under the same experimental conditions, i.e., $T_{\mathrm{rep}} = 0.8\,\mu\mathrm{s}$ and $\tau = 200\,\mathrm{ns}$, we see that the capability of having the signal available in real time has the cost of increasing the electronic noise level by 2.6 dB.

We investigate the effect of τ_{gate}, the time for which the SHA are gated, by measuring $\mathrm{var}N_{\mathrm{diff}}^{\mathrm{DA}}$ vs N_{L} for different values of τ_{gate} and compare the noise performance. We obtain the same results for $\tau_{\mathrm{gate}} = 250\,\mathrm{ns}$, the manufacturer recommended value, as for $\tau_{\mathrm{gate}} = 100\,\mathrm{ns}$, with fit parameters comparable within

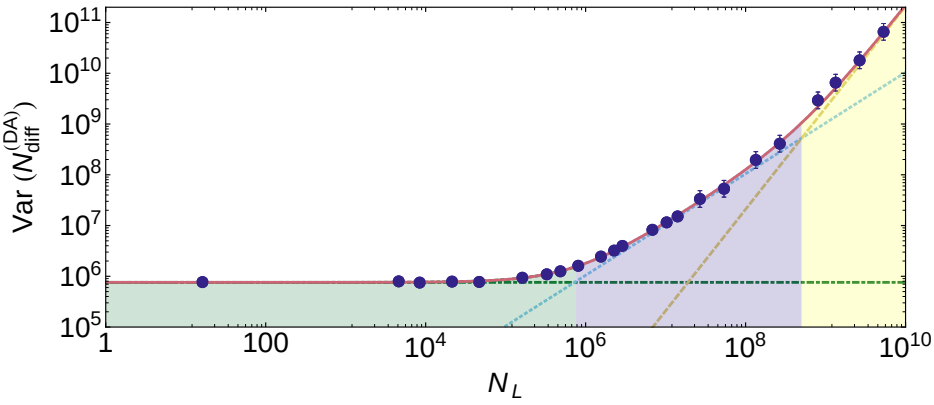

Figure 4.9: Variance of the output signal of the DA as function of the input photon-number in log-log scale. Solid red line fit to $\text{Var}(\text{NL}_{\text{diff}})$ using expression Eq. (4.1). Shaded areas depicts the different detection responses: green EN-limited, blue SN-limited and yellow TN-limited. Error bars represent $\pm 1\sigma$ standard error. Broken lines represent the different contribution from EN, SN and TN.

the error, but not for 50 ns where the DA-output is independent of N_{L}, i.e., dominated by electronic noise.

We study the effect of the settling time of SHA2 by varying the number of samples used for $\overline{V}_{\text{DA}}$ with t^{DA}. The gating times are unchanged, being $t_1^{(\text{gate})} = 10\,\text{ns}$ and $t_2^{(\text{gate})} = 20\,\text{ns}$ but for the analysis we take $N'_{\text{samp}} = 1$ point. We then fit $\text{var}N_{\text{diff}}^{(\text{DA})}$ to obtain the fit parameters a_0, η and a_2, from which we determine the EN-limited and TN-limited regions. In Fig. 4.10 we see that for values of t^{DA} where the noise of the SHA has not had time to settle the EN and the TN contributions are large, dominant over the SN. We also observe that once t^{DA} is sufficient, the EN region is flat as expected from the output of a the DA. From the fit output η we determine that the minimum time delay to faithfully sample the signal is $\text{t}^{\text{DA}} = 170\,\text{ns}$.

Comparing Fig. 4.9 and Fig. 4.10 we see that the SN-limited region is a bit narrower in the latter, due to the different N'_{samp} used in the analysis. This suggests that the output of the DA has fast frequency noise components that could be filtered to obtain the same noise performance as in the case of Fig. 4.9, i.e., averaging the DA output voltage.

Assuming an optical pulse with length equal to the DPD dead time, the minimum separation between consecutive pulses, or equivalently the higher measure-

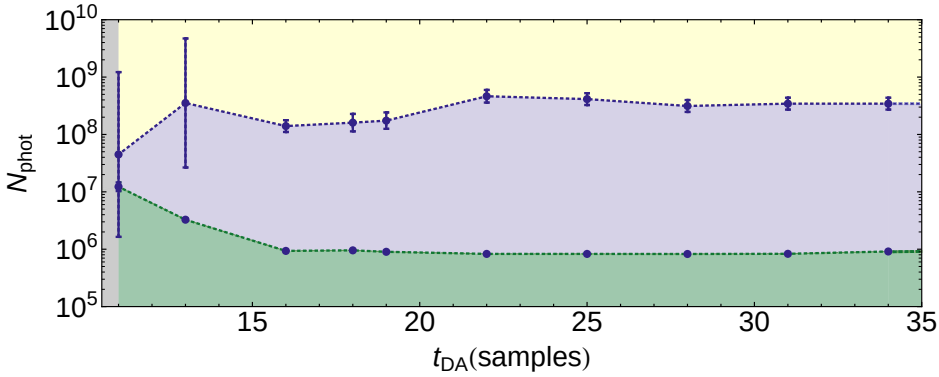

Figure 4.10: DA SN-limited region (blue area) as function of the SHA2 settling time (t^{DA}). Green shaded area is EN-limited region and TN-limited region in yellow, see text for details. Analysis done with $N'_{\text{samp}} = 1$ point at a sample rate of 100 Msps or 10 ns/sample. Error bars represent $\pm 1\sigma$ standard error.

ment bandwidth, is given the gating of the SHA, $\tau_{\text{gate}} = 100$ ns, its settling time of the second SHA, t^{DA} =170 ns and the analysis parameters N'_{samp} =10 ns. The maximum detection bandwidth in real time is $\simeq 2.3$ MHz.

4.3 DPD in Action

The DPD was used in the first experiment to combine simultaneous sub-projection-noise Faraday rotation measurements of both parallel and perpendicular components (Colangelo et al., 2017b). Several earlier experiments had demonstrated sub-projection-noise Faraday rotation measurements of a small component orthogonal to the mean spin, (Appel et al., 2009; Schleier-Smith et al., 2010b; Chen et al., 2011; Sewell et al., 2012) among other, and a few had made sub-projection-noise Faraday rotation measurements of the large component parallel to the mean spin (Béguin et al., 2014; Gajdacz et al., 2016; Kristensen et al., 2017).

Detecting the radial component with sub-Poisson sensitivity is a technical challenge since the radial component is large and the Poisson fluctuations are small, requiring a detector with high dynamic range. Moreover, the detector must precisely record both large and small rotations angles in rapid succession. The DPD we developed meets these technical challenges.

In the realization of that experiments a magnetic field along the x direction

drives a coherent rotation of the atoms in the y-z plane with a period T_L. It was necessary that the probe pulses length was much shorter than the Larmor precession period, $\tau \ll T_L$. This ensures that the time taken to complete a single-pulse measurement is small, i.e., the interaction between the light pulse and the atoms is almost instantaneous and the atomic state does not evolve during the probing. We sent probe pulses of τ =600 ns and the Larmor precession period was 38 µs.

As shown by Eq. (2.21) and described in references (Koschorreck et al., 2010a; Colangelo et al., 2013), the interaction Hamiltonian contains tensor light shifts. One possible strategy to minimize the tensorial polarizability is to alternate probe pulses with orthogonal polarizations, called "dynamical decoupling" probing (Koschorreck et al., 2010b). This cancellation works better when the time separation between different pulses is reduced. For this reason, having a detector with a high bandwidth was indispensable. Even though in the experiments reported in (Colangelo et al., 2017b,a) we did not take full advantage of the measurement bandwidth, we probed the atoms with vertically polarized probe pulses at 3 µs interval, with horizontally polarized probe pulses between the V-probe pulses, such probing rate would have been impossible with the previous detector.

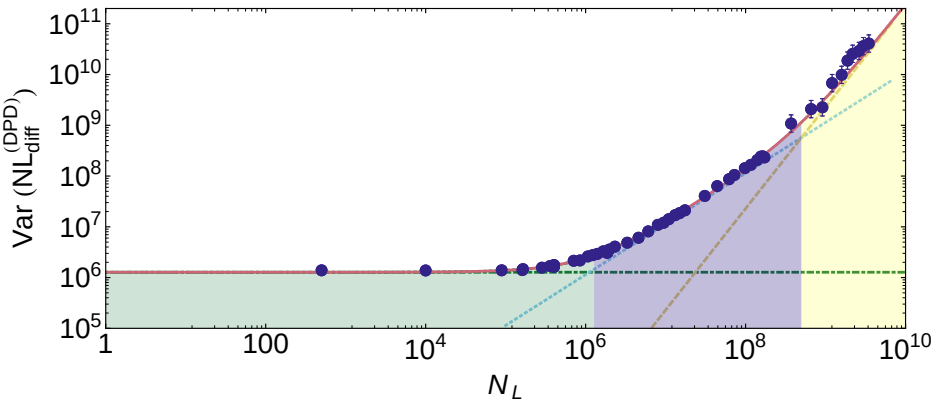

Figure 4.11: Shaper detector variance output signal in "balanced" configuration as a function N_{L} in log-log scale. Solid red line fit to Var(N_{diff}) using expression Eq. (4.1). Experimental parameters $T_{\mathrm{rep}} = 10\,\mu\mathrm{s}$, $\tau = 1\,\mu\mathrm{s}$.

The balanced detector we were using previously was developed by the group of Prof. Eugene Polzik from the Niels Bohr Institute of Copenhagen. It is based

on the same working principle, an integrator measures the difference in photo-charge between two photo-diodes. The main difference is that the signal from the integrator is fed into a pulse shaper giving an almost gaussian pulse output signal. As shown in Fig. 4.11, it had a larger electronic noise floor, requiring measurements with $N_{\mathrm{L}} > 2 \times 10^6$ photons to be in the shot noise limited region. At the same time, the detection of photons is technically noise limited for photons number $N_{\mathrm{L}} > 2 \times 10^8$, i.e., the shot noise limited range spans over two order of magnitude. The combination of integrator followed by a pulse shaper broadens the electronic response pulse compared to the detected optical pulse, where an input pulse of 25 ns FWHM produces a response pulse of 600 ns, limiting the measurement speed. Further details about this particular detector can be found in (Windpassinger et al., 2009; Windpassinger, 2008; Koschorreck, 2010).

4.4 Comparison with Literature

The DPD presented here offers a significant improvement in speed compared to other state-of-the-art detectors, while also having somewhat lower noise (Hansen et al., 2001; Windpassinger et al., 2009; Takeuchi et al., 2006). In (Windpassinger et al., 2009) two detectors based on two different charge-sensitive pre-amplifier are described with minimal NEC=280 electrons (Amptek-based detector) and NEC=340 electrons (Cremat-based detector) operated at speeds $\lesssim$ 200 kHz, exact value not reported. Our DPD shows a minimal NEC=242 electrons at 125 kHz, representing a noise improvement of 0.63 dB with respect to the Amptek-based detector and 1.84 dB to the Cremat-based detector, while operating at similar measurement bandwidth. Similarly, in (Takeuchi et al., 2006) the maximum measurement speed is 200 kHz and SN limited starting from 10^6 photons/pulse whereas at this bandwidth our DPD is SN limited from 7×10^4. Reference (Hansen et al., 2001), working at a repetition rate of 1 MHz reports a NEC of 730 electrons. At this speed, our DPD has a NEC of 600 electrons, a reduction of 0.87 dB.

Real time active control of quantum systems is a key element for advanced quantum information processing (Wiseman and Milburn, 2009; Serafini, 2012) and has been investigated in different platforms. It is very active area of research in the qubits community (Blok et al., 2014; Vijay et al., 2012), and has been applied to the detection of magnetic fields using real-time adaptive measurements (Bonato et al., 2016).

Focusing on atomic systems, prior work on feedback was done in Mabuchi's group (Geremia et al., 2004). Feedback schemes (Lloyd, 2000) have been theoretically proposed to deterministically produce spin squeezing states (Thomsen et al., 2002a,b) and have been experimentally produced (Inoue et al., 2013; Cox et al., 2016). Similar feedback schemes have been used to protect superposition

states against the decoherence induced (Vanderbruggen et al., 2013) or to remove entropy from an atomic ensemble (Behbood et al., 2013a).

Our real-time detection system fits the atomic needs where the coherence times running from µs to seconds requiring detection with low latency and large bandwidth to perform many manipulations of the atomic state before decoherence

A second atomic physics experiment in the group, this one working with a spinor Bose-Einstein condensate, uses a copy of this detector, also to measure Faraday rotation.

"In no affairs of mere prejudice, pro or con, do we deduce inferences with entire certainty, even from the most simple data"

Edgar Allan Poe, *The Narrative of Arthur Gordon Pym of Nantucket*

5 Radio-frequency interaction

In this chapter we describe the interaction of radio-frequency magnetic fields and alkali atoms. We begin with a basic overview of atomic magnetometry and find a theoretical description of the atomic spin evolution under such fields. After describing the magnetic side of the apparatus, we propose a new type of measurement that exploits the atomic coherence to sense arbitrarily-shaped radio-frequency time varying signals using a cold atomic ensemble. This measurement is compatible with spin squeezing and QND measurements. Finally, we experimentally verify the theory using a particular case of waveform, a linearly chirped signal. Parts of this chapter are published in reference (Martin Ciurana et al., 2017).

5.1 Principles of Atomic Magnetometry

Alkali atom based magnetometers have shown exceptional sensitivities (Kominis et al., 2003; Sheng et al., 2013; Dang et al., 2010) in magnetic field measurement. Atomic magnetometers characterize a magnetic field by observing the response of the atomic spins to the field. The valence electron couples more strongly than the nuclear spin to the external field, and so, to first order, the gyromagnetic ratio is simply that of a bare electron except that the electron spin must drag the nuclear spin along as it precesses. Detection of a magnetic field requires monitoring the spin precession due to the field, and there are numerous techniques for measur-

ing the atomic spin (Budker and Romalis, 2007). To date, most sensitive atomic magnetometers use optical read-out of the atomic state. Detection of small magnetic field requires detection of tiny optical rotation angles. DC magnetometers determine the amplitude of an external magnetic field by measuring the Larmor precession frequency of the atomic spins as

$$\omega_L = \gamma|\mathbf{B}| \tag{5.1}$$

where $\gamma = \mu_B g_F/\hbar$ =0.7 GHz T^{-1} for ^{87}Rb . The coupling of the spin to a magnetic field is given by the Hamiltonian

$$H = -\gamma \mathbf{F} \cdot \mathbf{B} \tag{5.2}$$

where we have taken $\hbar = 1$. The time evolution of the spins under the magnetic field is given by Eq. (2.27).

$$\frac{d}{dt}\mathbf{F} = \frac{1}{i}[\mathbf{F}, H] \tag{5.3}$$

Given the commutation relation between the angular momentum components we see that the spins precesses in a magnetic field accordingly to

$$\frac{d}{dt}\mathbf{F} = -\gamma \mathbf{B} \times \mathbf{F} \tag{5.4}$$

where γ is the gyromagnetic ratio. We see that Eq. (5.4) is equal to the classical equation for a dipole in a magnetic field, i.e., the effect of $\mathbf{B}$ on the atomic spin is to cause a precession about $\mathbf{B}$.

Atomic magnetometers can also be used to detect radio-frequency (RF) magnetic fields. As described earlier, the hyperfine interaction between the electron and the nuclear spins further splits the atomic energy level into states with total atomic spin $\mathbf{F}$. The interaction with an external magnetic field lifts the degeneracy between different Zeeman sub-levels. The resulting energy splitting ΔE solely depends on the strength of the bias field, see Eq. (5.1). The presence of an oscillating RF magnetic field applied transversally to the static bias field will induce resonant, coherent coupling between Zeeman sub-levels (Bloch, 1946; Hahn, 1950). The use of radio-frequency excitation to measure the Larmor frequency by monitoring the precessing transverse spin components was first proposed by Dehmelt (Dehmelt, 1957a,b), and the theory and first experimental demonstration were developed by Bell and Bloom (Bell and Bloom, 1957).

Formally, consider an oscillating field

$$\mathbf{B}_x(t) = \mathbf{x}\frac{\Omega}{\gamma}\cos(\omega t) \tag{5.5}$$

along the x-axis, which has two counter-propagating rotational components at frequencies $\pm\omega$ with amplitudes $\Omega/2$. The external bias is given by

$$\omega_L = \gamma|\mathbf{B}_0| \tag{5.6}$$

We assume that the oscillating frequency ω is much closer to ω_L than to $-\omega_L$, and shift to a reference frame that is co-rotating with the precessing spins and making the rotating wave approximation, i.e., neglecting all oscillations that are at frequencies far from the rotation frequency. Under such approximation the static bias field is replaced by an effective field

$$\gamma|\mathbf{B}_{\text{eff}}| = (\omega_L - \omega) \tag{5.7}$$

The co-rotating component of the oscillating field is static in this frame. The total effective magnetic field is given by

$$\gamma|\mathbf{B}_{\text{T}}| = (\omega_L - \omega) + \frac{\Omega}{2} \tag{5.8}$$

Using the dynamic evolution of the atomic spins given by Eq. (5.3), we obtain analytic expression for the time evolution of the atomic spin components assuming and input F_{y}-polarized state. As we measure in the lab frame, we transform the equations back and find:

$$F_{\text{x}}(t) = \left(\frac{\Omega \sin(\omega t) \sin(t\Omega')}{\Omega'} + \frac{2\Delta_{\text{RF}}\Omega \cos(\omega t) \sin\left(\frac{t}{2}\Omega'\right)^2}{\Omega'^2} \right) F_{\text{y}}(0) \tag{5.9a}$$

$$F_{\text{y}}(t) = \frac{\Delta_{\text{RF}}^2 + \Omega^2 \cos(t\Omega')}{\Omega'^2} F_{\text{y}}(0) \tag{5.9b}$$

$$F_{\text{z}}(t) = \left(-\frac{\Omega \cos(\omega t) \sin(t\Omega')}{\Omega'} + \frac{2\Delta_{\text{RF}}\Omega \sin(\omega_0 t) \sin\left(\frac{t}{2}\Omega'\right)^2}{(\Omega')^2} \right) F_{\text{y}}(0) \tag{5.9c}$$

where Ω and ω are the applied RF magnetic field amplitude and frequency, respectively. Ω' is the generalized Rabi frequency defined as

$$\Omega' = \sqrt{\Delta_{\text{RF}}^2 + \Omega^2} \tag{5.10}$$

where $\Delta_{\text{RF}} = \omega - \omega_L$ is the detuning of the RF from the resonance frequency. From Eq. (5.10) is easy to note that if the RF drive is not on resonance with the energy spitting introduced by the static bias field, its effect is to cause a faster oscillation of the spins.

In a typical Rabi flopping experiment, the observable is the spin population along the state preparation axis - i.e. in our case the F_{y} spin component - after

a fixed period of spin excitation. Here, in contrast, we measure the orthogonal F_z spin projection via Faraday rotation probing during the spin excitation. It is instructive to illustrate the different behavior of the components of **F**. The time evolution of the F_z and F_y components for various detunnings is depicted in Fig. 5.1. When the frequency of the RF-signal matches the atomic energy splitting the flopping frequency is minimal and the projection of the transverse spin component transferred by the RF maximal.

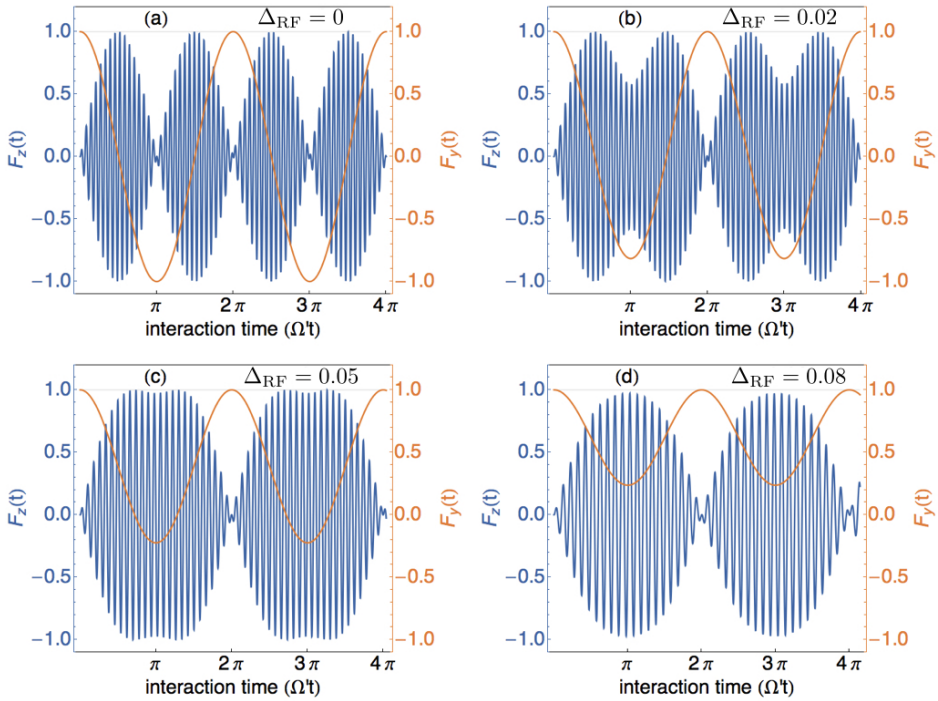

Figure 5.1: Simulation of the spin components evolutions using Eq. (5.9) for different detuning of the RF excitation. The spins, initially polarized along the y-axis evolve due to the interaction with the RF-field resulting in Rabi oscillations.

5.2 Detecting RF Excitations

The experimental apparatus is illustrated in Fig. 5.2. An RF field along x is produced with a low-inductance coil and an arbitrary waveform generator. Op-

tical pumping (OP) along the y direction is used to produce an initial atomic polarization, with an efficiency of $\sim 96\%$, as measured by Faraday rotation. A non-destructive measurement of the atomic state is made using a train of 600 ns duration pulses of linearly polarized light sent through the atoms at 4 µs intervals and 1500 MHz red detuned from the $f = 1 \rightarrow f' = 0$ transition on the D_2 line.

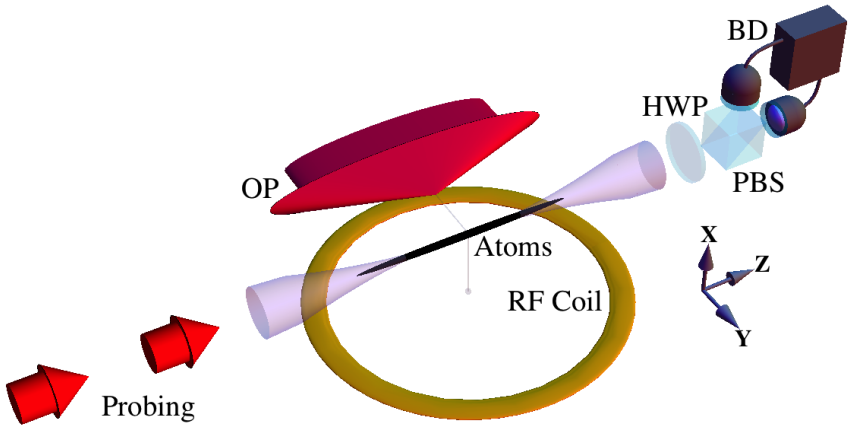

Figure 5.2: Experimental geometry (not to scale), showing dipole-trapped atoms, on-axis Faraday rotation probe pulses, transverse optical pumping (OP), and polarimeter elements: half-wave plate (HWP), polarizing beamsplitter (PBS), and balanced detector (BD). Radio-frequency (RF) magnetic fields in the $\hat{x}$ direction are produced by a coil, while a DC field of variable strength (not shown) is applied along $\hat{y}$.

5.2.1 Bias field adjustment

The geometry of the coils and their characteristics are described in (Schulz, 2002). In short, three coil pairs in near Helmholtz configuration surround the location of the atoms. They are used to cancel the earth and the laboratory environment fields and to set the desired bias field. They are operated by a low noise current source and produce bias fields of strengths in the 50 mG range. Given the full length of our atomic cloud, ~0.5 cm, atoms at different locations experience slightly different magnetic fields which cause them to precess at different frequencies. After a time sufficiently long the atoms would be out of phase and the atomic averaged signal measured with the Faraday probe will be zero. In order to minimize the field inhomogeneity along the sample length we use two sets of

four wires placed transversally to the trap axis, horizontally and vertically. They can handle currents up to 1500 mA to compensate for the gradient components $\partial B_{\mathrm{x}}/\partial z$ and $\partial B_{\mathrm{y}}/\partial z$. The coil pair to drive a field along the z-axis was designed to allow a current unequal currents in the to coils, with which $\partial B_{\mathrm{z}}/\partial z$ can be controlled.

A bias magnetic field along y is generated with coils in a near-Helmholtz geometry fed by a programmable current source and monitored using the atoms as an in-situ DC vector magnetometer. In the group we developed a technique to gain information about the three components of the magnetic field information and the gradient component along the trap axis (Behbood et al., 2013b). For the experiments presented in this thesis where the bias field is along one axis, a simplified version of the method is enough to set the field. We prepare the atoms to have $\langle \mathbf{F} \rangle$ along z under an orthogonal bias field B_{y} and observe free-induction decay (FID) (Abragam, 1961) signal of the resulting Larmor precession using the Faraday probe. A fit function of the type

$$\phi(t) = \beta + \alpha \cos(\omega_L t + \phi_0) e^{-t/T_2} \tag{5.11}$$

is sufficient to extract the field magnitude ($|B| = \omega_L/\gamma$) the components in the plane orthogonal to B_{y} ($\beta \propto \sqrt{B_{\mathrm{x}}^2 + B_{\mathrm{z}}^2}$) and the atomic coherence time T_2.

We minimize the amplitude of β by compensating homogeneous field along x and z directions with the bias coils and cancel field gradients along the length of the trap by adjusting the current in the compensating wires. The field is optimized in an iterative routine resulting in coherence time T_2 =4.8(3) ms and fields 99.1% along the y-axis. A typical optimized FID signal is shown in Fig. 5.3.

The coherence time is inversely proportional to the field gradient along the trap axis, $1/\mathrm{T}_2 \propto \partial|\mathrm{B}|/\partial\mathrm{z}$. To model the effect of the compensating wires we divide the field gradients into its parallel and perpendicular components to the bias field

$$\left(\frac{\partial|B|}{\partial z}\right)^2 = \left(\frac{\partial|B_{\mathrm{y}}|}{\partial z}\right)^2 + \left(\frac{\partial|B_{\perp}|}{\partial z}\right)^2 \tag{5.12}$$

To minimize the gradient field along the atomic cloud, the current through each set of wires reduces the corresponding term in the r.h.s. of Eq. (5.12). We fit the effect of the gradient compensation with the function

$$\mathrm{T}_2(\mathrm{I}) = \frac{\mathrm{a}}{\sqrt{(\partial \mathrm{B_y(I)}/\partial \mathrm{z} - \partial \mathrm{B_{y,0}}/\partial \mathrm{z})^2 + (\partial|\mathrm{B}_{\perp}|/\partial \mathrm{z})^2}} \tag{5.13}$$

The effect of the vertical compensating gradient wires is shown in Fig. 5.4 (a).

Experimentally we found that the bias field direction does have an effect on the efficiency of the F_{y}-state preparation. In order to have both a good state

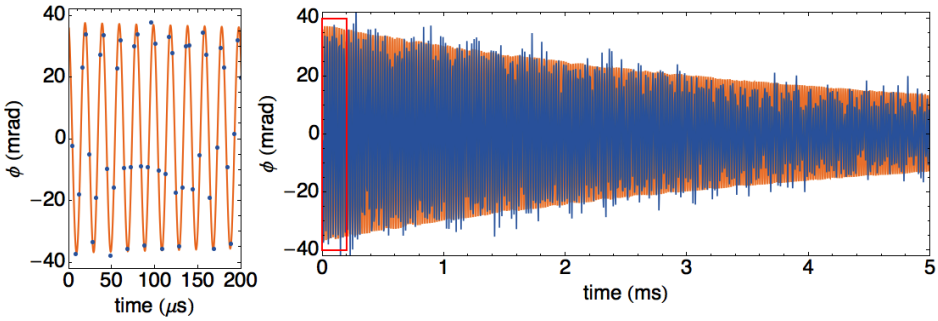

Figure 5.3: Free induction decay measurement of the F_z polarized state precessing in a magnetic field B_y, dark blue line. The orange line is a fit with the function Eq. (5.11), with fit outputs β =0.4(2) mrad, α =37.3(6) mrad, $\omega_L = 2\pi\times 50.35(5)$ kHz and T_2 =4.8(3) ms. Left plot is a zoom in on the FID trace for the first 200 µs.

polarization and a good coherence time it is necessary to iterate and fine tune the current through the bias coils and gradient wires. Fig. 5.4 (b) shows the change in atomic polarization for the same gradient compensating.

Another important aspect of the magnetic field is its stability. We can distinguish two time scales, short-term and long-term stability. By short-term stability, we refer to the stability of the B-field during a measurement process, including state preparation, evolution and detection, all in the range of 1 ms. In practice, the most important factor for the short-term stability is locking the measurement to the 50 Hz cycle of the mains, so that the field and its time derivative are reproducible from one measurement to the next. In Behbood et al. (2013b) we measured a peak to peak field fluctuation of ∼1 µT within a single 50 Hz cycle. By long-term stability we mean to have the experiment close to the same conditions in order to repeat it many times to collect statistics. For the squeezing experiments we need a large N_A and we run multiple experiments with the same atoms, we repeat successive trap loadings typically every 10 s. To collect statistics for the squeezing experiments we repeat the trap loading a minimum of 100 times. Thus, by long term stability we refer to have the same environmental conditions over to course of 15 min. In order to improve it one can use magnetic shielding (Kominis et al., 2003), active field control (Smith et al., 2011).

5.2.2 Radio-frequency Setup

The strength of the bias field determines the resonant frequency of the RF excitation. We decided to work in the ∼50 kHz regime as it was a good compromise

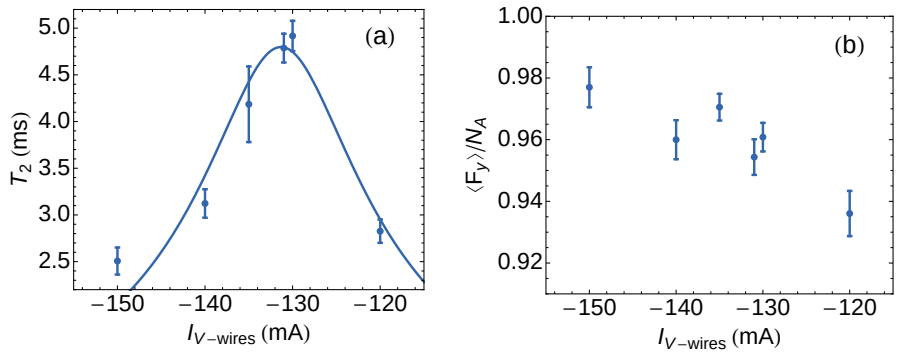

Figure 5.4: Atomic coherence time T_2 (a) and normalized atomic polarization along the y-axis (b) as a function of the current applied to the gradient-inducing vertical wire pairs. After the field optimization we can prepare the atoms in a macroscopic magnetization along the y-axis, with $F_\mathrm{y} \simeq N_\mathrm{A}$, $> 96\%$, and having a long coherence time, $\mathrm{T}_2 \approx 4.8\,\mathrm{ms}$. Solid line is fits using Eq. (5.13). Error-bars represent $\pm 1\sigma$ standard error.

between the measurement bandwidth and the field homogeneity. The atom-light interaction described by Eq. (2.21) is valid when the dynamical evolution of the system has to be much slower than the interaction time, i.e., the pulse duration τ has to be much shorter than the Larmor period T_L. On the other hand, the measurement time must be shorter that the atomic coherence time T_2. These two conditions can be expressed by the set of equations

$$\tau \ll T_L \propto |B_\mathrm{y}| \tag{5.14a}$$

$$N_\mathrm{p}\tau < \mathrm{T}_2 \propto \frac{\partial \mathrm{B}}{\partial \mathrm{z}} \tag{5.14b}$$

where N_p are the total number of pulses used in the measurement. Although we can apply a larger bias field and still fulfill Eq. (5.14a), we observed that for fields in the range of 100 mG, the gradient compensation was poor and the coherence time was reduced.

In order to drive radio-frequency fields to the atoms four main elements are needed: a frequency source that produces the RF signal, a switch to trigger the emission of the signal, an amplifier and the antenna responsible for driving the excitation. At this low frequencies and given the physical space limitations around the vacuum chamber, it is challenging to make a resonant antenna based on a driving LC-resonant circuit. The antenna we made to drive the RF-excitation

was a loop antenna with 25 mm diameter with 14 windings made out of a 1 mm thick copper wire. The coil was placed outside the vacuum chamber, approximately 8 cm from the atoms position, i.e., in the near-field. Its position and orientation were adjusted while watching the Rabi flopping driving the amplifier in the linear regime, i.e., far from saturation. We maximized the amplitude of the Rabi oscillations and the time the atoms oscillated for. In this way we ensure that the radiation pattern produced by the antenna is homogeneously distributed over the atomic cloud. The RF-signal is generated by the function generator (Tabor WW1281 A) and amplified using a low-frequency amplifier (Mini-Circuits, ZHL-32A+). The output of the amplifier is connected to the antenna via a unidirectional-coupler (Mini-Circuits, ZDC-15-6) to prevent the reflected power of the antenna, which is not impedance matched, from reaching the amplifier.

5.2.3 Rabi flopping measurements

To characterize the field-atom coupling we add an oscillatory driving field perpendicular to a static bias field. The combined effect of these two magnetic fields is to induce Rabi oscillations between the magnetic sub-levels of the atoms in the hyperfine levels. We load the ODT, apply a bias field along the y-axis, optically pump the atoms with a single 50 µs long pulse along the bias field and apply the RF signal with constant amplitude but varying frequency. In order to minimize probe scattering the atoms are probed semi-continuously with $N_{\mathrm{L}} \approx 2 \times 10^6$ photons and Δ =1.5 GHz. The measured F_{z} component is fitted with Eq. (5.9c) to determine the best-fit values for the mean drive field amplitude $\bar{\Omega}/2\pi$ =0.23(3) kHz and the mean on-resonance frequency $\bar{\omega}_L/2\pi = 42.28(1)$ kHz. The parameters $\bar{\omega}_L$ and $\bar{\Omega}$ are used to compute the theoretical solid curves in Fig. 5.6 (a). From the measured F_{z} evolutions we estimate $\mathfrak{f}_y = \min \sqrt{F^2 - F_z^2}$, the minimum of the longitudinal spin projection. In Fig. 5.6 (b) we plot the normalized maximal spin projection along the z-axis, $\mathcal{F}_z$, normalized by the total spin, $|F|$, obtained from the measured $F_{\mathrm{z}}(t)$.

In Fig. 5.5 we plot the measured Rabi frequencies as a function of the RF excitation frequency and find good agreement between the data and the theory.

5.3 Waveform Component Detection

State-of-the-art atomic sensors coherently detect the signal of interest in an scheme based on a Ramsey interferometry sequence. These sensors employ a measure-evolve-measure (MEM) sequence, in which a the system is prepared in a desired state, followed by a period of free evolution sometime called “Ramsey time” which accumulates signal over a time comparable to the atomic coherence

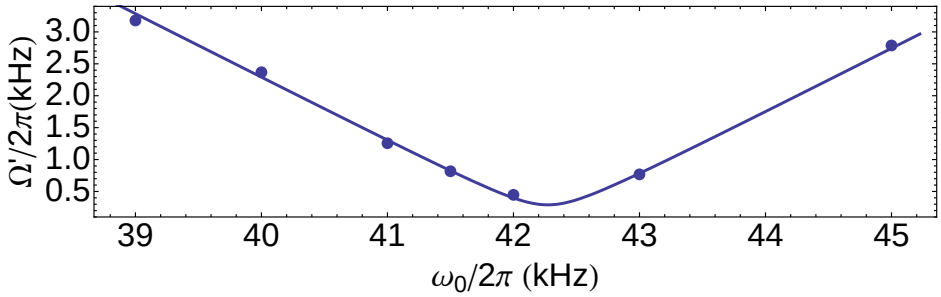

Figure 5.5: Measured generalized Rabi frequencies. Solid line is a theory curve using Eq.(5.10) and the best-fit values for $\bar{\Omega}$ and $\bar{\omega}_L$.

time. To stop the signal accumulation, the atomic system is transformed back and read-out. The atomic state readout typically destroys coherence.

It was originally devised as a way of measuring nuclear magnetic moments in a molecular beam using two oscillating fields at different points along the beam (Ramsey, 1950), but it has evolved into a widely applicable metrological technique. The Ramsey sequence underpins nearly all precision measurement made with atomic sensors. To list some examples, it has been used in precise measurements Earth's gravitational field (Rosi et al., 2014; Gillot et al., 2014), as inertial measurements (Dutta et al., 2016), to measure fundamental constants (Bouchendira et al., 2011) and to measure magnetic fields and time (Sewell et al., 2012; Leroux et al., 2010b), resulting in the most precise measurements ever made using an atomic ensemble (Hinkley et al., 2013; Bloom et al., 2014).

Focusing on magnetometry, up to now MEM sequences have been applied for the detection of constant (Sewell et al., 2012) and oscillating magnetic fields (Ockeloen et al., 2013). Here we extend coherent detection type of measurements to more general waveforms, those with time varying radio-frequency. As we have just seen, atoms are resonant to the particular RF matching the Larmor energy splitting. By adjusting the strength of the bias field we modify the atomic resonance frequency. The measurable atomic displacement takes the form of overlap integral, with a pattern function that is controlled by the experimenter. We extend coherent detection type of measurements to allow quantification of arbitrarily-shaped radio-frequency signal components. In the following section we formally describe our protocol.

5.3.1 Principle of the method

We consider an ensemble of atoms, described by a polarization $\mathbf{F}$, precessing in response to a magnetic field $\mathbf{B}(t) = \mathbf{y}B_{\mathrm{y}}(t) + \mathbf{x}B_{\mathrm{x}}(t)$, with $|B_{\mathrm{y}}| \gg |B_{\mathrm{x}}|$.

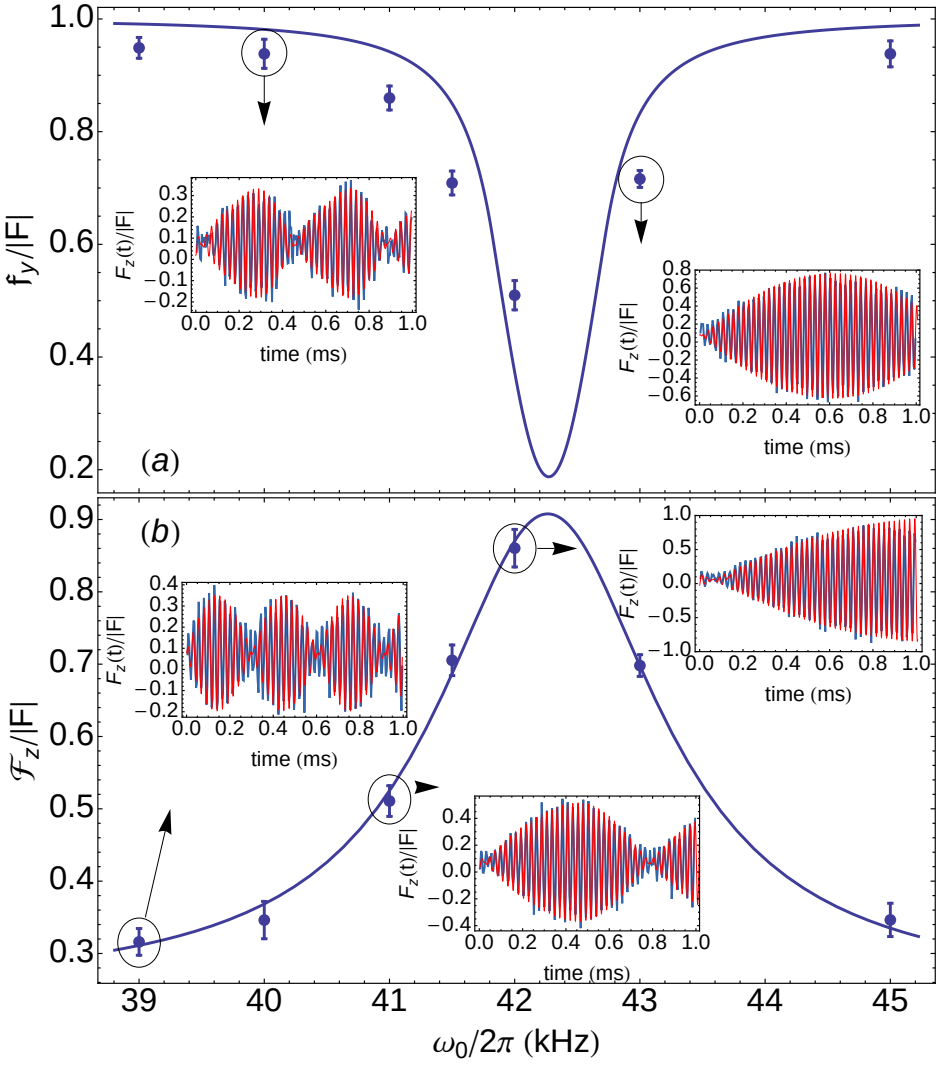

Figure 5.6: Atom-field coupling characterization. (a) Normalized minimum spin projection along the y-axis $\mathfrak{f}_y/|F|$, an estimate of the amount the spin vector has been tilted away from F_y by the RF-field. Solid line is a theory curve. (b) Normalized maximal spin projection along the z-axis, $\mathcal{F}_z$, normalized by the total spin, $|F|$. Error bar indicate $\pm 1\sigma$ standard error of the mean. Insets show representative traces of F_z versus time (blue curves) and fits of the rotating-wave solution of Eq. (5.15) (red curves).

F precesses about y at an experimenter-controlled Larmor angular frequency $\omega_L(t) = \gamma B_{\rm y}(t) + O(\gamma B_{\rm x}^2/B_{\rm y}) \approx \gamma B_{\rm y}(t)$, driven transversally by the small unknown perturbation $B_{\rm x}(t)$. The component $F_{\rm z}$ is assumed accessible to QND measurement.

The dynamics of the spins are governed by the Heisenberg equations of motion, Eq. (5.3), to find

$$\frac{d}{dt}F_i = -i[F_i, H_0(t) + H'(t)] \tag{5.15}$$

where $H_0 = -\gamma \mathbf{F}\cdot\mathbf{B} = -\gamma F_{\rm y} B_{\rm y}(t)$, γ is the gyromagnetic ratio for the $F = 1$ ground hyperfine state, and $H' = -\gamma F_{\rm x} B_{\rm x}(t)$ describes the unknown perturbation, assumed to be in the radio-frequency range. Under the assumption that $|B_{\rm y}| \gg |B_{\rm x}|$ a perturbation treatment is enough to solve the system dynamics. We use a Dyson series (Sakurai, 1994) to solve the resulting system of differential equations. We define $\mathbf{F}^{(0)}(t)$ to be the solution to Eq. (5.15) when $H' = 0$, i.e. $F_{\rm y}^{(0)}(t) = F_{\rm y}(0)$

$$\begin{pmatrix} F_{\rm z}^{(0)}(t) \\ F_{\rm x}^{(0)}(t) \end{pmatrix} = \begin{pmatrix} \cos\Theta(t) & \sin\Theta(t) \\ -\sin\Theta(t) & \cos\Theta(t) \end{pmatrix} \begin{pmatrix} F_{\rm z}(0) \\ F_{\rm x}(0) \end{pmatrix} \tag{5.16}$$

where $\Theta(t) \equiv \int_0^t dt'\,\omega_L(t')$, with $\omega_L(t) \equiv \gamma B_{\rm y}(t)$ is the accumulated angle. We then use the well-known result (Sakurai, 1994)

$$F_i(t) = F_i^{(0)}(t) - i\int_0^t dt'\,[F_i^{(0)}(t), H'(t')] + O(H')^2 \tag{5.17}$$

which, from the definition of $H'(t')$ gives the signal

$$\begin{aligned} F_{\rm z}(t) &= \cos\Theta(t)F_{\rm z}(0) + \sin\Theta(t)F_{\rm x}(0) \\ &\quad -\gamma\int_0^t dt'\,F_{\rm y}(t')B_{\rm x}(t')\cos[\Theta(t) - \Theta(t')] \\ &\quad +O(B_{\rm x})^2 \end{aligned} \tag{5.18}$$

We note that $F_{\rm y}(t') = F_{\rm y}(0) + O(B_{\rm x})^2$. At the same time, we can express $\delta F_{\rm y}^2 = \langle F_{\rm y}^2\rangle - \langle F_{\rm y}\rangle^2$, finding

$$\begin{aligned} F_{\rm z}(t) &= \cos\Theta(t)F_{\rm z}(0) + \sin\Theta(t)F_{\rm x}(0) \\ &\quad -\gamma\langle F_{\rm y}(0)\rangle\int_0^t dt'\,B_{\rm x}(t')\cos[\Theta(t) - \Theta(t')] \\ &\quad +O(B_{\rm x})^2 + O(\gamma t B_{\rm x}\delta F_{\rm y})^2. \end{aligned} \tag{5.19}$$

We note that the first line describes an operator relation, namely a rotation of the spin components $F_{\rm z}, F_{\rm x}$ about y, and contains the quantum noise associated

with the spin variables. In contrast, the second line of Eq. (5.19) has no operator content and describes a noiseless displacement by an amount proportional to the integral of the waveform $B_{\mathrm{x}}(t')$ multiplied by the *pattern function* $\cos[\Theta(t) - \Theta(t')]$. This describes a coherent build-up of the signal component matching the pattern function and a cancellation of signal components orthogonal to it (de Icaza Astiz et al., 2014). By proper choice of $\Theta(t)$, the pattern function can be made to take on any functional form bounded by ± 1. In this way, an arbitrarily-chosen waveform component can be selected for quantum-enhanced coherent estimation, with the measurement programmed by the applied $B_{\mathrm{y}}(t)$. The third line of Eq. (5.19) is negligible for the interesting case of weak signals and large atom number.

The formalism we have just described is general and valid for any type of excitation. In the following we experimentally verify it using a particular type of waveform, linearly chirped radio-frequency drives. In the following section we describe how to increase the signal accumulated by the atomic ensemble, that is, we restrict ourself to the second line of Eq. (5.19). In the subsequent chapter, **Chapter 6**, we will describe how to increase the sensitivity of the measurement by preparing the atoms in a reduced noise state.

5.3.2 Coherent detection of chirped radio-frequency signals

We have started this chapter describing the working principle of radio-frequency magnetometers. These magnetometers are sensitive to sinusoidal signals, which are a particular case of chirped signals in which the *chirp*, i.e. the change of frequency per unit time, is zero. We can use some of the things we have learned from the standard RF case for the detection of chirped excitations.

The signal we want the detect has a frequency varying in time as described by

$$B_{\mathrm{x}}(t) = \frac{\Omega}{\gamma} \cos(\omega_0 t + \kappa t^2) \tag{5.20}$$

Intuitively, the atomic energy splitting also has to change in time to efficiently detect this signal. This is to say that the bias magnetic fields need to be ramped. To characterize the ramp of the bias field we fit the FID signal with a chirped function of the form $\phi(t) = \beta + \alpha \cos(\omega_L t + \kappa t^2 + \phi_0) e^{-t/T_2}$, and follow the procedure described in Sect 5.2.1 to optimize the homogeneity of the field and the state preparation efficiency, i.e., we adjust the field gradients during the ramp to minimize the inhomogeneities introduced by the field ramp. We set the bias field to be constant for 200 µs and apply a ramp over 800 µs. Fitting the FID traces we find $\kappa = 2\pi \times 7.0(2) \times 10^6\,\mathrm{Hz}^2$ and T_2 =4.5(4) ms over the full 1 ms long measurement. Comparing against the T_2 value obtained for the constant bias field, we observe that the we can control the field homogeneity equally well

in the two cases.

To confirm the linearity of the chirp we divide the FID-signal in 100 µs long segments and fit them individually with a function $\tilde{\phi}(t) = \beta' + \alpha' \cos(\omega_{\mathrm{L}}^{(i)} t + \phi_0')$, where $\omega_{\mathrm{L}}^{(i)}$ is the Larmor frequency of the i-th segment. A quadratic fit to the fit outputs for $\omega_{\mathrm{L}}^{(i)}$ confirms the linearity of the ramp as the quadratic term in negligible, $a_2 t/a_1 = 1.6 \times 10^{-4}$, where t =800 µs is the time during the ramp is on, see Fig. 5.7.

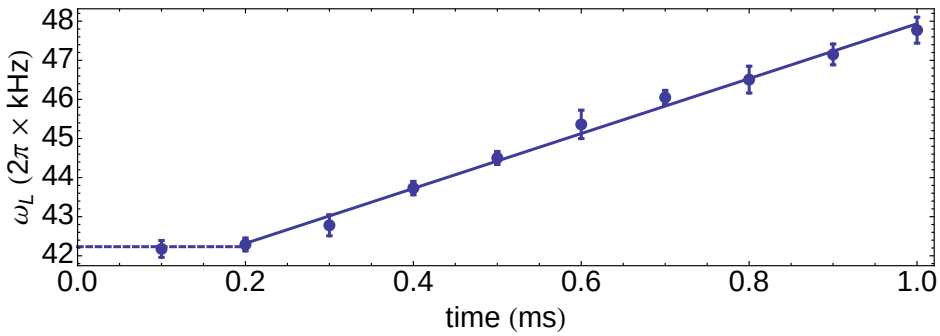

Figure 5.7: Change in Larmor frequency ω_L as a function of time. Solid line is a linear fit with slope $2\pi\times$ 7.0(2) $\times 10^6$ Hz^2. Broken line is the mean ω_L before the current of the y-coils is increased. Error bars represent $\pm 1\sigma$ standard error of the mean.

To study the chirped RF-excitation, the atoms are prepared by optical pumping in F_{y}-polarized state under a parallel and constant field. After the state preparation, we produce the same shape of the bias field as described above, constant for 200 µs followed by a ramp over 800 µs. This produces a Larmor frequency that sweeps linearly from $\omega_L^{(1)} = 2\pi \times 42.2$ kHz to $\omega_L^{(2)} = 2\pi \times 47.8$ kHz. During the ramp we send transverse RF chirped fields produced by the arbitrary waveform generator while we probe the atoms with the Faraday probe. Fig. 5.8 shows the observed F_{z} signal at different times during the frequency reamp as a function of the chirp κ. Agreement with theory from Eq. (5.15) is good, and variation in experimental signal is consistent with the independently-measured fluctuations of the magnetic field at the position of the atoms.

Selective response to chirped waveforms is shown in Fig. 5.9. There we plot $\mathcal{F}_z$, the maximal spin projection along the z-axis normalized by the total spin $|F|$, obtained from the measured $F_{\mathrm{z}}(t)$ There we plot the normalized maximal spin projection along the z-axis $\mathcal{F}_z$ normalized by the total spin $|F|$, obtained from the measured $F_{\mathrm{z}}(t)$. The ramp produces a "chirped" pattern function $\Theta(t)$,

making the atoms sensitive to $B_x(t)$ signals with similar chirp, but less sensitive to other waveforms, e.g. at constant frequency or with the opposite chirp. As expected, we observe a peak in the population transferred by the RF drive when κ matches the field ramp.

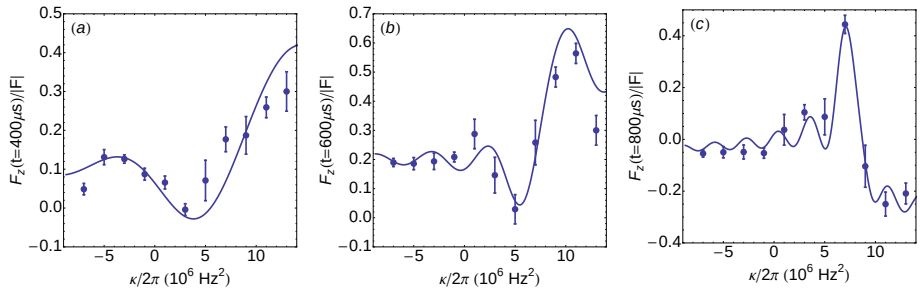

Figure 5.8: Axial polarization $F_z(t)/|F|$ at time (a) t=400 µs (b) t=600 µs and (c) t=800 µs. Solid line shows the solution of Eq. (5.15) with no free parameters.

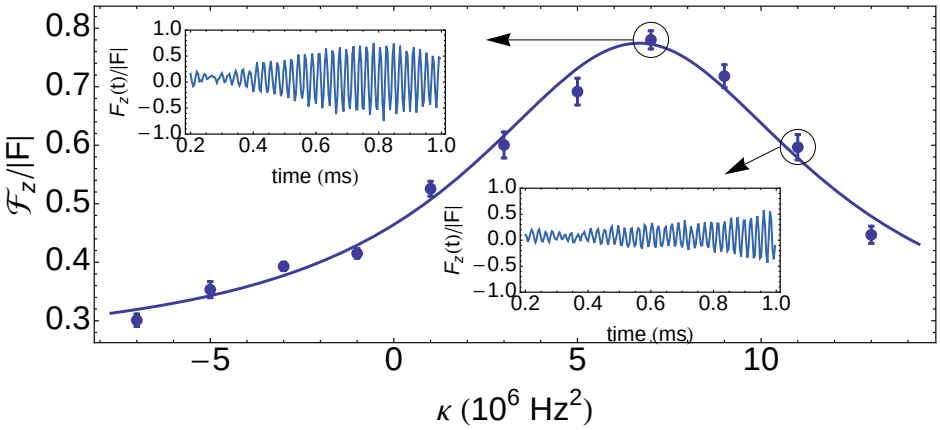

Figure 5.9: Maximal axial polarization $\max_t F_z(t)/|F|$ versus chirp of the RF excitation and confirms the specificity for waveforms resembling the pattern function. Representative traces in the insets. Solid line is the result of a Lorentzian fit giving the resonant chirp $\kappa/2\pi = 6.7(2) \times 10^6\,\mathrm{Hz}^2$. Error bars show $\pm 1\sigma$ standard error of the mean.

"But we cannot do it all at once; it is a sequence. An unfolding process. We can only control the end by making a choice at each step"

Philip K. Dick, *The Man in the High Castle*

6

Quantum enhanced radio-frequency waveform detection

In this chapter we describe atomic spin squeezed measurements in a magnetically sensitive system. We achieve spin squeezing using modulated quantum non-demolition measurements to evade the measurement back-action. We combine quantum nondemolition measurements and stroboscopic probing to detect waveform components with magnetic sensitivity beyond the standard quantum limit. We do this for two cases of interest, linearly chirped RF-magnetic fields and sinusoidal RF excitations, and achieve in both cases metrologically relevant improvement due to spin squeezing. The combination of quantum sensing advantage while also allowing full use of the system coherence results in a sensitivity-volume figure of merit comparable to the best RF magnetometers at these frequencies. Most of the contents of this chapter are published in reference (Martin Ciurana et al., 2017).

6.1 Creating Squeezed States by Stroboscopic Back-action Evading Measurements

The squeezed state is created by first preparing a CSS along the $\hat{y}$-axis and then making a collective measurement of F_z with measurement outcome ϕ. The

presence of a bias field along the same direction of the OP cause the mean spin to remain aligned along the field. The spin uncertainty in the x-z plan precesses around the external field at the Larmor period ω_L. Stroboscopic probing at twice the Larmor frequency allows the quantum uncertainty to redistribute, producing a state with a uncertainty below the SQL for the measured component while still fulfilling the Heisenberg uncertainty principle Eq. (2.3). In this way, the variable measured, F_{z}, is cyclic and as a result, the stroboscopic probing is equivalent to the probing of a constant of the motion. The measurement back-action appears in the orthogonal spin component, F_{x}, which will be anti-squeezed. However, F_{x} is not coupled in the measurement as the probing is always done at every π-phase interval.

This probing scheme was theoretically proposed in the context of gravitational wave detection in the late 70's (Thorne et al., 1978). Variations of this approach have been implemented with magnetic spin oscillators (Vasilakis et al., 2011, 2015) and mechanical oscillators (Suh et al., 2014).

6.2 Back-action Evading Waveform Detection

Looking back to Eq. (5.19), the first line described an operator relation. As with other squeezing-enhanced atomic measurements, the noise in $F_z(t)$ can be reduced by squeezing a linear combination of $F_z(0)$ and $F_x(0)$. To detect chirped waveform components beyond the projection-noise level we combine back-action evading measurements with coherent detection. Reduction of spin projection noise below the SQL (Takano et al., 2009; Appel et al., 2009; Schleier-Smith et al., 2010b; Chen et al., 2011; Sewell et al., 2012), has been demonstrated by quantum non-demolition measurement (Mitchell et al., 2012; Sewell et al., 2013) including large degrees of squeezing using cavity enhancement (Bohnet et al., 2014; Hosten et al., 2016b). Use of conditional spin-squeezed states has been demonstrated in magnetometry (Sewell et al., 2012) and clock operation (Appel et al., 2009; Leroux et al., 2010a; Hosten et al., 2016b).

These works employ a measure-evolve-measure (MEM) sequence, in which a first QND measurement produces a state with reduced projection noise, a period of free evolution accumulates signal, and a second QND measurement detects the change relative to the first measurement. This method exploits the coherence of the atomic system, allowing signal to accumulate prior to readout of the atomic state, which typically destroys coherence.

We generalize this method and apply it for the quantum enhanced detection of linearly chirped waveforms.

6.2.1 Experimental details

Measuring the quantum noise requires repetitions of the preparation and measurement of the atomic system many times to compute the variance of the measured optical signals $\mathrm{var}(\hat{S}_\mathrm{y})$.

For a single experiment we load the ODT with $N_\mathrm{A} = 1.3 \times 10^6$ atoms, measure the bias field ramp as in (Behbood et al., 2013b) and then repeat the following MEM sequence 21 times: dispersive measurement of N_A as described in Sect. 3.3; optical pumping to produce full polarization along $+y$; stroboscopic QND measurement $\mathcal{M}_1$ with result Φ_1; free evolution for time $t_\mathrm{hold} = 600\,\mu\mathrm{s}$; and a second stroboscopic QND measurement $\mathcal{M}_2$ with result Φ_2, as illustrated in Fig. 6.1. During the hold time B_y is ramped with $\kappa = 2\pi \times 5.6(1) \times 10^6\,\mathrm{Hz}^2$. The QND measurements $\mathcal{M}_1$ and $\mathcal{M}_2$ are made over 200 µs and contained 2.9×10^8 photons. The 21 repetitions of the MEM sequence allow us to vary N_A since atoms are lost from the trap during optical pumping.

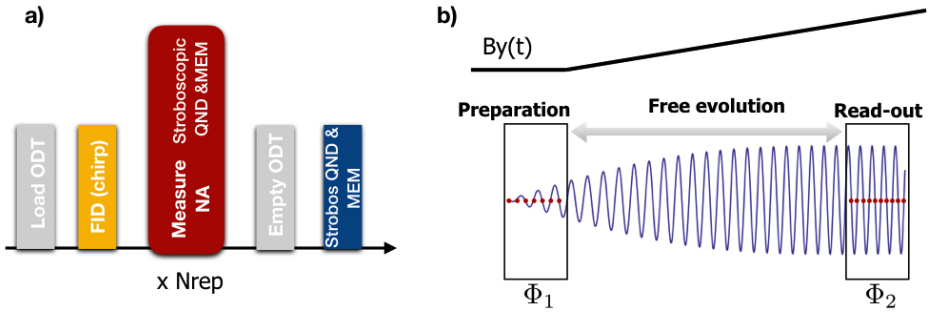

Figure 6.1: (a) Simple pulse sequence for stroboscopic QND measurement of atoms. We load atoms into the dipole trap. We polarize them along the z-axis under a B_y-field and measure a free induction decay signal to monitor the bias magnetic field. We re-polarize the atoms along the z direction under a B_z field to measure N_A in the dipole trap. Immediately afterward the atoms are polarized along the y-direction under a y-directed B-field and stroboscopic trains of QND-pulses are applied with t_hold =600 µs in between them. We repeat N_rep =21 times the spin state measurements. The atoms are released from dipole trap and the same probing sequence is applied one time to the empty trap to measure the polarimeter bias. This whole cycle is repeated 83 times. (b) Measure-evolve-measure sequence and illustration of back-action evading measurement of precessing spins for chirped $\omega_L(t)$. Probe times t_i are illustrated by red dots, timed to give precession angle $\Theta(t_i) = n\pi$ for integer n.

The probing is done using $\tau_{\rm pulse}$ =600 ns duration pulses of linearly polarized light with a detuning of 700 MHz to the red of the ^{87}Rb D_2 line. During a probe pulse the atomic spins rotate by an angle $\theta = \gamma B \tau_{\rm pulse}$. For the experiments here described the strength of the bias is $B = |\mathbf{B}| < 50\,\mathrm{mG}$, so during the optical pulse the atoms experience a rotation of their spins of $\theta \approx 13\,\mathrm{mrad}$, which can safely be neglected to treat the pulses as "instantaneous" from the atoms' point of view. Each QND measurement experiences a polarization rotation $\phi_n = g_1 F_{\rm z}(t_n)$, where n indexes the pulses. Because of the inversion of $F_{\rm z}$ between pulses and the pulse length, the ϕ_n can be aggregated as a single distributed measurement of $F_{\rm z}$, quantified by the pulse-train-averaged rotation signal

$$\Phi \equiv {N_{\rm p}}^{-1} \sum_{n=1}^{N_{\rm p}} (-1)^{n-1} \phi_n \tag{6.1}$$

as described in (Sewell et al., 2013; Koschorreck et al., 2010a). This represents a composite QND measurement of the input $F_{\rm z}$ variable (Vasilakis et al., 2011, 2015).

During $\mathcal{M}_1$ the field is constant. As we have shown in the previous chapter, in order to detect a chirped waveform the bias field needs to be ramped. For this experiment, the bias field produced Larmor frequency starting at $\omega_L^{(1)} = 2\pi\times$ 42.5 kHz and finishing at $\omega_L^{(2)} = 2\pi\times$ 47.1 kHz over a time interval of 800 µs, i.e., the atoms are sensitive to linearly chirps with $\kappa/2\pi = 5.8(1) \times 10^6\,\mathrm{Hz}^2$. This value is determined using the method described in Sec. 5.3.2. For technical reasons (the large inductance of the coils setting the bias field) the field produced by the bias coils was still increasing and $\mathcal{M}_2$ is performed on a slope of field. The probe periods $T_{\rm probe}^{(1)}$ =11.8 µs and $T_{\rm probe}^{(2)}$ =10.7 µs matched the Larmor precession frequency during $\mathcal{M}_1$ and $\mathcal{M}_2$ and contained $N_{\rm p}^{(1)} = 16$, $N_{\rm p}^{(2)} = 18$ pulses, respectively, with $N_{\rm L} = 1.81 \times 10^7$ photons per pulse.

6.2.2 Statistics of probing inhomogeneously-coupled atoms

As described in Sect. 2.5.3, in oder to properly determine the coupling between the atoms and the probe beam the spatial structure becomes important. We consider the statistics of the Faraday rotation measurements of an ensemble of $N_{\rm A}$ atoms, described by individual spin operators $\mathbf{f}_i$. To define the SQL, we consider the atomic ensemble to be in a coherent spin state, with independent individual spins and fully polarized with $\langle F_{\rm y}\rangle \simeq N_{\rm A}$. When the spatial structure of the probe beam is taken into account, the Faraday rotation is described by the

input-output relation for the Stokes component $\hat{S}_{\mathrm{y}}$

$$\hat{S}_{\mathrm{y}}^{(\mathrm{out})} = \hat{S}_{\mathrm{y}}^{(\mathrm{in})} + \hat{S}_{\mathrm{x}}^{(\mathrm{in})} \sum_{i=1}^{N_{\mathrm{A}}} g(\mathbf{x}_i) f_{\mathrm{z}}^{(i)} \tag{6.2}$$

where $g(\mathbf{x}_i)$ is the coupling strength for the i-th atom, proportional to the intensity at the location $\mathbf{x}_i$ of the atom. $\hat{S}_{\mathrm{y}}^{(\mathrm{in})}$ has zero mean and variance $N_{\mathrm{L}}/4$, where N_{L} is the mean photon number in the probe pulse $\hat{S}_{\mathrm{x}}$. The atomic spin is polarized along F_{y} and orthogonal to the measured F_{z} direction. The rotation angle $\phi = \hat{S}_{\mathrm{y}}^{(\mathrm{out})}/\hat{S}_{\mathrm{x}}^{(\mathrm{in})}$ has statistics

$$\begin{aligned} \langle \phi \rangle &= \langle f_{\mathrm{z}} \rangle \sum_{i=1}^{N_{\mathrm{A}}} \langle g(\mathbf{x}_i) \rangle_{\mathbf{x}_i} \\ &\equiv \langle f_{\mathrm{z}} \rangle \langle N_{\mathrm{A}} \rangle g_1 \end{aligned} \tag{6.3}$$

$$\begin{aligned} \mathrm{var}(\phi) &= \mathrm{var}(\phi_0) + \mathrm{var}(f_{\mathrm{z}}) \left\langle \sum_{i=1}^{N_{\mathrm{A}}} g^2(\mathbf{x}_i) \right\rangle_{N_{\mathrm{A}}, \mathbf{x}_i} \\ &\equiv \mathrm{var}(\phi_0) + \mathrm{var}(f_{\mathrm{z}}) \langle N_{\mathrm{A}} \rangle \tilde{g}_1^2 \end{aligned} \tag{6.4}$$

where ϕ_0 is the polarization angle of the input light, subject to shot-noise fluctuations and assumed independent of F_{z}, and the angle brackets indicate an average over the number and positions of the atoms. For known $\langle f_{\mathrm{z}} \rangle$ and $\mathrm{var}(f_{\mathrm{z}})$, measurements of $\langle \phi \rangle$ and $\mathrm{var}(\phi)$ versus N_{A} give the calibration factors g_1 and $\tilde{g}_1^2$.

Calibration of the g_1 factor

We calibrate $\langle \phi \rangle$, the measured rotation angle of the dispersive atom number measurement against an independent estimate of N_{A} made via absorption imaging. The results where shown in Fig. 3.8. To save on page-turning we reprint the calibration curve in Fig. 6.2 (a).

Calibration of the $\tilde{g}_1$ factor

To measure $\tilde{g}_1$ we use the the stroboscopic QND data. The atoms are prepared in an F_{y}-polarized state and then probed stroboscopically at twice the Larmor period, in such a way that the measured variable is $\pm F_{\mathrm{z}}$, evading back-action effects. The variance of the averaged rotation signal defined in Eq. (6.1) is

$$\mathrm{var}(\Phi) \equiv \mathrm{var}(\Phi_0) + \tilde{g}_1^2 \sum_{n=1}^{N_{\mathrm{p}}} \mathrm{var}(F_{z,n}) \tag{6.5}$$

with zero mean and variance $\mathrm{var}(\Phi_0) = (N_\mathrm{p} N_\mathrm{L})^{-1}$, and $F_{z,n}$ is the value of F_z at the time of the n-th probe pulse.

We compute the resulting evolution of the state using the covariance matrix methods described in (Colangelo et al., 2013) including probe-induced decoherence resulting in

$$\mathrm{var}\left(\frac{g_1}{N_\mathrm{p}}\sum_{n=1}^{N_\mathrm{p}} F_{z,n}\right) = \tilde{g}_1^2 \frac{1}{2}\alpha N_\mathrm{A} \tag{6.6}$$

where the correction factor α accounts for decoherence and noise introduced into the atomic state due to off-resonant probe scattering during the QND measurement.

Calculation of the noise contribution α

During each QND probe off-resonant scattering of photons introduces decoherence by pumping some into the far-off-resonance $f = 2$ ground state, and adds noise as some atoms return to the $f = 1$ state with randomized polarizations.

As described in Sec. 3.4.3, to measure the damage due to probing η_{sc} we prepare a state polarized along the y-axis under a B_y-field and send probe pulses with constant amplitude but varying length. The atomic polarization is then rotated into F_z by adiabatically rotating the bias field from B_y to B_z and probed with the Faraday probe, the same method used to quantify the state preparation efficiency. We fit the rotation angle of the probed states versus N_L with an exponential and find the atom-photon scattering probability $\eta_{sc} = 2.9(1) \times 10^{-11}$. The curve is shown in Fig. 3.11 and reprinted in Fig. 6.2 for convenience of the reader.

For known η_{sc} and branching ratio for atom excited from $f = 1$ to $f' = \{0, 1, 2\}$ and returning to the $f = 1$ manifold with random polarization, it is possible to calculate the atomic noise reduction, as described in (Colangelo et al., 2017b). We find $\alpha = 0.96$.

Projection noise level

Fig. 6.3 shows the measured variance of Φ_2 of the second train of QND-pulses as a function of the number of atoms in the trap. A linear measurement will show a variance that is quadratic in N_A:

$$\mathrm{var}(\Phi) = \mathrm{var}_0(\Phi) + \tilde{g}_1^2 \frac{1}{2}\alpha N_\mathrm{A} + a_2 N_\mathrm{A}^2. \tag{6.7}$$

Here $\mathrm{var}_0(\Phi)$ is the readout noise, which can be quantified by repeating the measurement without atoms in the trap since a negligible fraction of photons

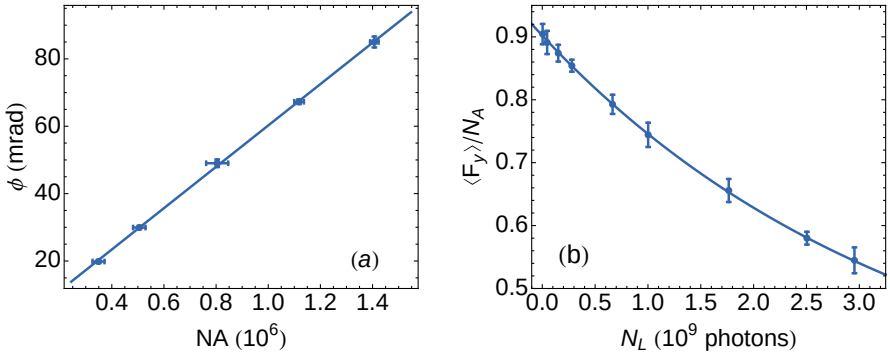

Figure 6.2: (a) Calibration of the mean Faraday rotation signal against input atom number N_{A} measured via absorption imaging. Solid line, the fit curve $\phi = a_0 + g_1 N_{\mathrm{A}}$ with values $g_1 = 6.16(9) \times 10^{-8}$ radian·atom^{-1}. (b) Atomic loss of coherence as a function of the number of photons in the measurement. Solid line is a fit with an exponential decay used to determine η_{sc}=2.9(1) $\times 10^{-10}$ photons^{-1} Error bars indicate $\pm 1\sigma$ statistical errors.

$\eta_{sc} N_{\mathrm{A}} \simeq 10^{-4}$, where η_{sc} is the atom-photon scattering rate, is lost due to off-resonant scattering. The term $a_2 N_{\mathrm{A}}^2$ corresponds to atomic technical noise associated with, e.g., fluctuations in state preparation, and the term $\propto N_{\mathrm{A}}$ corresponds to atomic projection noise. The factor 1/2 describes the F_{z} variance of an $f = 1$ atom polarized along y, and α accounts for the net noise reduction due to off-resonant scattering of probe photons, as we have just described. A fit of Eq. (6.7) to the data finds $\tilde{g}_1^2 = 1.2(2) \times 10^{-14}$ rad^2, determining the projection-noise level.

It is noticeable that Fig. 6.3 has a significant amount of technical noise. This extra noise is coming from the fact that the second QND measurement is done during the ramp of the magnetic field, and as a consequence the cancellation of the measurement back-action is poor.

6.2.3 Squeezing

To study the generation of squeezing we look at the correlation between $\mathcal{M}_1$ and $\mathcal{M}_2$. The first train of QND-pulses redistributes the noise to the non-measured component and $\mathcal{M}_2$ is used to evaluate its variance conditioned on the first measurement. The measurement noise reduction is quantified by $\mathrm{var}(\Phi_2|\Phi_1) = \mathrm{var}(\Phi_2 - \chi\Phi_1)$, where $\chi = \mathrm{cov}(\Phi_1, \Phi_2)/\mathrm{var}(\Phi_1) > 0$ describes the correlation be-

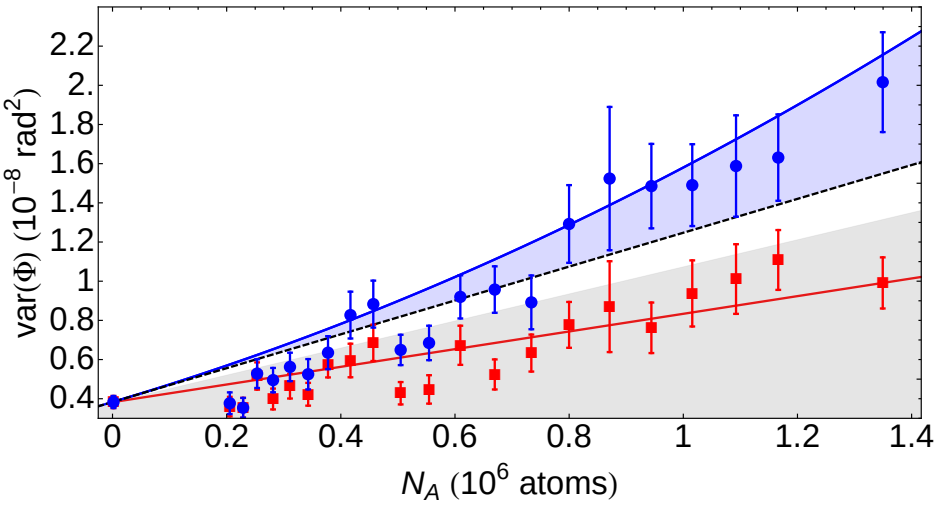

Figure 6.3: Atomic noise scaling of the stroboscopic QND measurement as a function of N_{A} for chirped bias field. Black dashed line shows calculated atomic projection noise for a coherent spin state (CSS) with $\mathrm{var}(\Phi) = \tilde{g}_1^2 N_{\mathrm{A}}/2$ plus readout noise (optical shot noise). Blue solid line is a quadratic fit to Φ_2 (blue circles) using Eq. (6.7). Blue shaded region shows atomic technical noise. The red squares indicate the conditional variance $\mathrm{var}(\Phi_2|\Phi_1)$ as a function of N_{A}, and the solid red line quadratic fit. Gray shaded area shows region of metrologically-relevant spin squeezing. Error bars represent $\pm 1\sigma$ standard error.

tween Φ_1 and Φ_2. The conditional variance is 0.71(8) below the projection noise level, or equivalently, 1.5(3) dB of noise reduction.

Metrological improvement is quantified by an expression similar to the Wineland criterion (Wineland et al., 1992), but taking into account the coherence loss and the noise reduction of the measured state, as defined in Eq. (2.35)

$$\xi_m^2 = \frac{1}{\eta^2} \frac{\mathrm{var}(\Phi_2|\Phi_1)}{\mathrm{var_L}(\Phi_1)} \tag{6.8}$$

where $\xi_m^2 < 1$ indicates metrological advantage and η accounts for the total loss of coherence of the spin-squeezed state relative to the input coherent spin state. The symbol in the denominator, $\mathrm{var_L}(\Phi_1)$, stands for the measured variance in Φ_1, including the N-independent component (read-out noise) and the component linear in N, which comes from atomic projection noise. The coherence after the first measurement is $F_{\mathrm{y}}^{(\mathcal{M}_1)} = \eta F_{\mathrm{y}}$, where $\eta \equiv (1-\eta_{\mathrm{sc}})(1-\eta_{\mathrm{field}})$ and $\eta_{\mathrm{sc}} = 0.08$ and $\eta_{\mathrm{field}} = 0.04$ are independently measured coherence loss due to probe scattering and field inhomogeneities, respectively, during $\mathcal{M}_1$. We find the metrological improvement due to squeezing $\xi_m^2 = 0.84(8)$. The noise in the optical rotation signal is reduced by 1.5(3) dB, while precision in the angle rotated by the atoms is increased by 0.8(3) dB.

6.3 Entanglement-assisted RF Sensing

The radio-frequency case is included as a special case of the chirped waveform detection beyond the projection-noise level when $\kappa = \kappa_L = 0$. In this section we demonstrate back-action evasion in a MEM sequence to detect RF magnetic fields.

We load the ODT with $N_{\mathrm{A}} = 1.5 \times 10^6$ atoms, measure the bias field and then repeat the following MEM sequence 16 times: dispersive measurement of N_{A}; optical pumping to produce full polarization along $+y$; QND measurement of $\mathcal{M}_1$ with result Φ_1; free evolution for time $t_{\mathrm{hold}} = 300\,\mu\mathrm{s}$; and a second QND measurement $\mathcal{M}_2$ with result Φ_2, as illustrated in Fig. 6.4.

During the hold time B_{y} is held constant, i.e. $\kappa = 0$, with $\omega_L = 2\pi \times 50.16\,\mathrm{kHz}$. The QND measurements $\mathcal{M}_1$ and $\mathcal{M}_2$ are made over 200 µs with T_{probe} =9.9 µs and containing $N_{\mathrm{p}}^{(1)} = N_{\mathrm{p}}^{(2)} = 20$ probe pulses, each with $N_{\mathrm{L}} = 2 \times 10^7$ photons. We repeat the full sequence 463 times to collect statistics. The experimental results are shown in Fig. 6.5.

Analyzed as above, we find a noise reduction of 0.58(5), or in power, 2.4(2) dB. Using Eq. (6.8) we find metrological improvement due to squeezing of $\xi_m^2 = 0.79(5)$, or 1.0(2) dB. The increased squeezing relative to the chirped case is due to the larger N_{A} and higher total photon number used in each collective

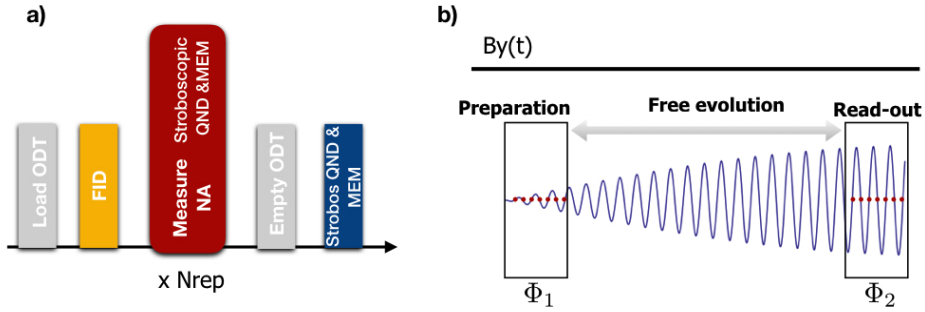

Figure 6.4: (a) Simple pulse sequence for stroboscopic QND measurement of atoms. Details are given in Fig. 6.1. Atom trap loading. Bias field monitoring. N_{rep} =16 repetition of the stroboscopic spin state measurements with t_{hold} =300 µs. Atoms are released from dipole trap, and a bias of polarimeter is measured. This whole cycle is repeated more than 463 times. (b) Measure-evolve-measure sequence and illustration of back-action evading measurement of precessing spins experiencing a fixed $\omega_L(t)$. Probe times t_i are illustrated by red dots, timed to give precession angle $\Theta(t_i) = n\pi$ for integer n.

measurement. The technical noise accumulated during the t_{hold} is smaller as the free evolution time is reduced. The limitation of t_{hold} is coming from the noise introduced by the mains, resulting in a different Larmor precession for the two measurements.

The presence of squeezing implies quantum correlation among the atoms, i.e., entanglement, which could be intra-atom entanglement of electron and nuclear spin, as presented in (Fernholz et al., 2008) or inter-atom entanglement, or both. To determine multi-particle entanglement we make use of the theory developed in (Sørensen and Mølmer, 2001). From this reference, we find that a single spin-1 system obeys the relation $\mathrm{var}(\mathrm{f_z}) \geq (1 - \sqrt{1 - \langle \mathrm{f_y} \rangle^2})/2$, where the f operators describe a single atom. By convexity arguments the macroscopic versions is

$$\mathrm{var}(\mathrm{F_z}/\mathrm{N_A}) \geq (1 - \sqrt{1 - \langle \mathrm{F_y}/\mathrm{N_A} \rangle^2})/2 \tag{6.9}$$

where the F operators describe the collective spin of N_A spin-1 atoms. The spin polarization after the measurement $\mathcal{M}_1$ is given by $\langle F_y \rangle = \eta N_A$, where $\eta \equiv (1 - \eta_{\mathrm{sc}})(1 - \eta_{\mathrm{field}})$ and $\eta_{\mathrm{sc}} = 0.11$ and $\eta_{\mathrm{field}} = 0.04$ are independently measured coherence loss due to probe scattering and field inhomogeneities, respectively. This gives $\mathrm{var}(\mathrm{F_z}/\mathrm{N_A}) \geq 0.24$.

Considering only the spin noise of the state produced by the QND measurement in Fig. 6.5, i.e., subtracting the readout noise, the measured atomic conditional

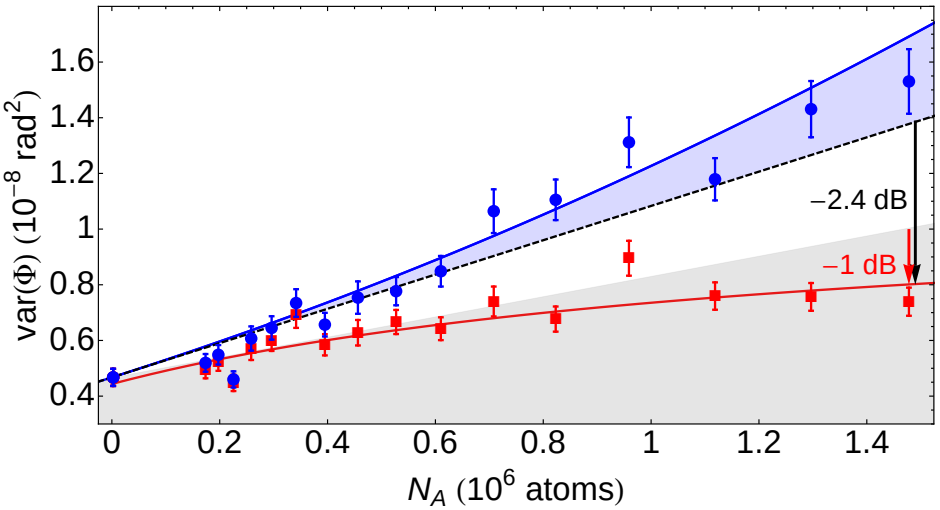

Figure 6.5: Atomic noise scaling of the stroboscopic QND measurement as a function of N_{A} for constant bias field. Black dashed line shows calculated atomic projection noise for a coherent spin state (CSS) with $\mathrm{var}(\Phi) = \tilde{g}_1^2 N_{\mathrm{A}}/2$ plus readout noise (optical shot noise). Blue solid line is a quadratic fit to Φ_2 (blue circles) using Eq. (6.7). Blue shaded region shows atomic technical noise. The red squares indicate the conditional variance $\mathrm{var}(\Phi_2|\Phi_1)$ as a function of N_{A}, and the solid red line quadratic fit to it. Gray shaded area shows region of metrologically-relevant spin squeezing. Error bars represent $\pm 1\sigma$ standard error.

variance is $[\mathrm{var}(\Phi_2|\Phi_1) - \mathrm{var}_0(\Phi)]\,/\mathrm{var}(\Phi_2)$=0.20(4). The results thus suggest (with 1σ confidence) inter-atom entanglement.

6.4 Field Sensitivity

In the previous section we have shown that by means of stroboscopic probing we can elude the measurement back-action and successfully achieve spin squeezing. Furthermore, from the optical rotation signal we can infer the F_{z}-component, and from its displacement from the origin we can infer the strength of the radio-frequency magnetic field.

6.4.1 Faraday Rotation Signal

We make use of the measured Faraday rotation signal to estimate the field amplitude. The observed signal is

$$\phi = g_1 F_z \tag{6.10}$$

with variance

$$\mathrm{var}(\phi) = \mathrm{var}(\phi_0) + \tilde{g}_1^2 \mathrm{var}(F_\mathrm{z}) \tag{6.11}$$

where $\mathrm{var}(\phi_0)$ is the read-out noise. For the spin squeezed state, we measure the conditional variance

$$\Delta^2\phi_\mathrm{cond} \equiv \mathrm{var}(\phi_2|\phi_1) = \mathrm{var}(\phi_0) + \tilde{g}_1^2 \mathrm{var}(F_\mathrm{z}^{(\mathrm{SSS})}) \tag{6.12}$$

By error propagation, the sensitivity to a parameter β is

$$\delta\beta = \frac{\Delta\phi(t)}{\left|\frac{d\langle\phi(t)\rangle}{d\beta}\right|} \tag{6.13}$$

from which we can estimate the sensitivity to the field amplitude Ω using a coherent spin state to be

$$\delta B^{(\mathrm{CSS})} = \frac{\Delta\phi}{|d\langle\phi\rangle/d\Omega|} = \frac{\Delta\phi}{g_1|F|}\frac{1}{I} \tag{6.14}$$

In Eq. (6.14) we can see that to precision with which we can estimate the phase depends on the mean spin length which acts as a lever arm, as discussed in Sec. 2.1.1. It also depends on I, the total coherent signal accumulated by the atoms described by the second line of Eq. (5.19).

Using spin squeezed atoms to sense a field would lead to a measurement sensitivity

$$\delta B^{(\mathrm{SSS})} = \frac{\Delta\phi_\mathrm{cond}}{\eta g_1|F|}\frac{1}{I} \tag{6.15}$$

where η is the polarization loss during the measurement. The sensitivity enhancement due to spin squeezing is quantified by

$$\frac{\delta B^{(\mathrm{SSS})}}{\delta B^{(\mathrm{CSS})}} = \frac{\Delta\phi_\mathrm{cond}}{\eta\Delta\phi} \tag{6.16}$$

or in variance, by the ratio

$$\xi_\mathrm{m}^2 = \frac{1}{\eta 2}\frac{\mathrm{var}(\phi_2|\phi_1)}{\mathrm{var}(\phi_1)} \tag{6.17}$$

which justifies the definition of metrological spin-squeezing factor introduced earlier, see Eq. (6.8).

6.4.2 Coherent signal accumulation

As shown in Eq. (6.15), in order to estimate the field sensitivity it is necessary to calculate the signal accumulated by the atoms during the free evolution period. Recalling Eq. (5.19), dropping the higher order terms and including that the probing is done at times such that $\Theta(t_i) = n\pi$, simplifies this expression further

$$F_{\mathrm{z}}(t_n) = (-1)^n \left(F_{\mathrm{z}}(0) - \gamma \langle F_{\mathrm{y}}(0) \rangle \int_0^{t_n} dt'\, B_{\mathrm{x}}(t') \cos\Theta(t') \right) \tag{6.18}$$

The accumulated signal during the hold time t_{hold} can be obtained by computing Eq. (6.18) for the two waveforms used.

For the detection of linearly chirped RF-excitations the bias field $B_{\mathrm{y}}(t)$ needs to have a ramp, which makes the atoms resonant to signals of the form $B_{\mathrm{x}}(t) = \Omega\cos(\omega t + \kappa t^2)$. The phase accumulated is $\Theta(t) = \omega_L t + \kappa_L t^2$, where $\kappa_L = (\omega_f - \omega_i)/\Delta t$ describes the change of the Larmor frequency caused by the ramp, applied for a time Δt. The radio-frequency magnetometry is included as a special case when $\kappa = \kappa_L = 0$. The probing is done twice per Larmor period, i.e., $\Theta(t) = n\pi$, which allows us to write Eq. (6.18) as

$$\begin{aligned} F_z(T) &= F_{\mathrm{z}}(0) - \gamma \langle F_{\mathrm{y}}(0) \rangle \int_0^T dt'\, \Omega \cos(\omega t' + \kappa t'^2) \cos(\omega_L t' + \kappa_L t'^2) \\ &= F_{\mathrm{z}}(0) - \gamma \Omega \langle F_{\mathrm{y}}(0) \rangle I_{\mathrm{chirp}}(\omega_L, \omega, \kappa_L, \kappa, T) \end{aligned} \tag{6.19}$$

Evaluating the integral on resonance, this is with $\omega = \omega_L$ and $\kappa_L = \kappa$ we get

$$\begin{aligned} I_{\mathrm{chirp}}(\omega_L, \omega, \kappa_L, \kappa, t_{\mathrm{hold}}) = \frac{t_{\mathrm{hold}}}{2} + \frac{\sqrt{\pi}}{4\sqrt{\kappa}} \Bigg[\cos\left(\frac{\omega_L^2}{2\kappa}\right) \left(C\left(\frac{\omega_L}{\sqrt{\pi\kappa}}\right) - C\left(\frac{2t_{\mathrm{hold}}\kappa + \omega_L}{\sqrt{\pi\kappa}}\right)\right) + \\ + \sin\left(\frac{\omega_L^2}{2\kappa}\right) \left(S\left(\frac{\omega_L}{\sqrt{\pi\kappa}}\right) - S\left(\frac{2t_{\mathrm{hold}}\kappa + \omega_L}{\sqrt{\pi\kappa}}\right)\right) \Bigg] \end{aligned} \tag{6.20}$$

where $S(u)$ and $C(u)$ are Fresnel sine and cosine integrals. Note that for $u \gg 1$, $S(u) \simeq 1/2 - \frac{1}{\pi u}\sin(\pi u^2/2)$ and $C(u) \simeq 1/2 + \frac{1}{\pi u}\cos(\pi u^2/2)$. In cases of interest, $\kappa \ll \omega_0$, giving the leading-order linear increase in signal. The error in ignoring the oscillating terms is smaller than 3% for our parameters.

From Eq. (6.13), the sensitivity of a coherent spin state to the RF drive amplitude Ω during a time t_{hold} is

$$\begin{aligned} \delta B_{\mathrm{RF}}^{\mathrm{CSS}} &= \frac{\Delta\Phi}{|d\langle\Phi\rangle/d\Omega|} = \frac{\Delta\Phi}{g_1 \langle F_{\mathrm{y}}(0)\rangle} \frac{1}{\gamma\ I(\omega_L, \omega, \kappa_L, \kappa, t_{\mathrm{hold}})} \\ &\simeq \frac{\Delta\Phi}{g_1 \langle F_{\mathrm{y}}(0)\rangle} \frac{2}{\gamma\ t_{\mathrm{hold}}} \end{aligned} \tag{6.21}$$

where we have used the definition of $g_1 = \phi/N_\mathrm{A}$ and the fact that $\langle F_\mathrm{y}(0)\rangle = N_\mathrm{A}$. For the spin squeezed state

$$\delta B_\mathrm{RF}^\mathrm{SSS} \simeq \frac{\Delta\Phi_\mathrm{cond}}{g_1\eta\langle F_\mathrm{y}(0)\rangle}\frac{2}{\gamma\ t_\mathrm{hold}} \tag{6.22}$$

where $\Delta\Phi^2_\mathrm{cond} = \mathrm{var}(\Phi_2|\Phi_1)$ is the conditional variance between the Φ_2 and Φ_1 optical signals.

Even though standard RF drive is included in the discussion presented above, it is illustrative to take a closer look at this case for a moment. In this experiment B_y is constant so that $\omega_L(t) = \omega_L$ and $\Theta(t) = \omega_L t$. Following the same analysis as for the case of chirped RF excitations, the signal accumulated can be estimated by solving Eq. (6.18), written as

$$\begin{aligned} F_\mathrm{z}(T) &= F_\mathrm{z}(0) - \gamma\langle F_\mathrm{y}(0)\rangle \int_0^T dt' B_x(t')\cos(\omega_L t') \\ &= F_\mathrm{z}(0) - \gamma\langle F_\mathrm{y}(0)\rangle I_\mathrm{RF}(\omega_L, \omega, T) \end{aligned} \tag{6.23}$$

We take the radio-frequency drives to have the quadrature $B_\mathrm{x}^{(\mathrm{c})}(t) = \Omega\cos(\omega t)$. Evaluating the integral on resonance, i.e. with $\omega = \omega_L$, we get

$$I_\mathrm{RF}^{(\mathrm{c})}(\omega_L = \omega, \omega, t_\mathrm{hold}) = \frac{t_\mathrm{hold}}{2} - \frac{\sin(2\omega t_\mathrm{hold})}{4\omega} \simeq \frac{t_\mathrm{hold}}{2} \tag{6.24}$$

since $1/\omega \ll t_\mathrm{hold}$. This result is a simplified solution of Eq. (6.20), which is not surprising since the RF-drive scenario is a special case of the most general chirped waveforms. However, solving the integration for the other quadrature, $B_\mathrm{x}^{(\mathrm{s})}(t) = \Omega\sin(\omega t)$ on resonance, we find the solution

$$I_\mathrm{RF}^{(\mathrm{s})}(\omega_L = \omega, \omega, t_\mathrm{hold}) = \frac{\sin(\omega t_\mathrm{hold})^2}{2\omega} \tag{6.25}$$

We see that the two integrations describe different quantities. The cosine quadrature can be associated with the spins' phase accumulation as it grows with time, whereas the sine component gives information about the spins trajectory as it shows a oscillating nature. In Fig. 6.6 we plot the solution for Eq. (6.24) and Eq. (6.25).

6.4.3 Magnetic sensitivity

The quantum enhanced single-shot sensitivity of the atoms to RF-drive amplitude can be estimated by using Eq. (6.22), which we re-write as

$$\delta B_\mathrm{RF}\sqrt{t_\mathrm{hold}} \simeq \frac{\sqrt{\mathrm{var}(\Phi_2|\Phi_1)}}{g_1\eta_\mathrm{hold}\langle F_\mathrm{y}(0)\rangle}\frac{2}{\gamma\ \sqrt{t_\mathrm{hold}}} \tag{6.26}$$

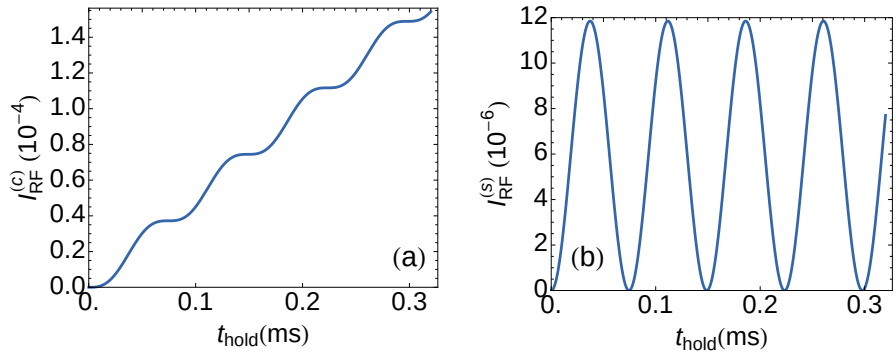

Figure 6.6: Analytical solution to the $I_{\mathrm{RF}}(\omega_L, \omega = \omega_L, t_{\mathrm{hold}})$ for (a) the cosine quadrature of the RF-drive and (b) the sine component using the experimental parameters. In (a) we can observe a growing as expected from the phase accumulation, whereas (b) has a cyclic character.

where $\mathrm{var}(\Phi_2|\Phi_1)$ is the conditional variance between the Φ_2 and Φ_1 optical signals, including the atomic noise and read-out noise, $\langle F_{\mathrm{y}}(0)\rangle = N_{\mathrm{A}}$ and η_{hold} is the total coherence loss during $\mathcal{M}_1$ and t_{hold}.

The experimental parameters for the two RF waveform used, i.e., constant frequency and linearly chirped, were different, having distinct evolution times and maximum number of atoms in the ODT. For the chirped excitation detection, the parameters are t_{hold} =600 µs and $N_{\mathrm{A}} = 1.3 \times 10^6$ atoms, from which we estimate a single-shot sensitivity of 3.36 $\mathrm{pT}/\sqrt{\mathrm{Hz}}$. For the constant frequency case, the free evolution time is t_{hold} =300 µs and $N_{\mathrm{A}} = 1.5 \times 10^6$ atoms, from which we estimate a single-shot sensitivity is 2.96 $\mathrm{pT}/\sqrt{\mathrm{Hz}}$.

Focusing on the latter, scaling the sensitivity by the volume of the atomic cloud, see Sec. 3.4.2 for details, $V = 1.8 \times 10^{-6}\mathrm{cm}^3$, we find $\delta\mathrm{B}\sqrt{\mathrm{V}} \approx 3.96$ $\mathrm{fT}\sqrt{\mathrm{cm}^3/\mathrm{Hz}}$. For comparison, the best alkali-vapor RF magnetometer (Lee et al., 2006) in this frequency range showed a sensitivity of 0.24 $\mathrm{fT}/\sqrt{\mathrm{Hz}}$ with $V = 96$ cm^3 or $\delta\mathrm{B}\sqrt{\mathrm{V}} = 2.35$ $\mathrm{fT}\sqrt{\mathrm{cm}^3/\mathrm{Hz}}$. Thus the RF magnetometer demonstrated here has a volume-adjusted sensitivity comparable with the best existing instruments.

It is illustrative to compare the sensitivity achieved with the quantum enhanced atoms to the ideal classical sensitivity. We use Eq. (6.21) to estimate the classical sensitivity, where the noise in the rotation angle $\Delta\Phi^2 = \mathrm{var}(\Phi_0) + \tilde{g}_1^2 N_{\mathrm{A}}/2$ is coming from the atomic projection noise for an ideal coherent spin state and the optical shot noise. The estimated single-shot sensitivity is 3.28 $\mathrm{pT}/\sqrt{\mathrm{Hz}}$. Comparing the two values, we see that the squeezed sensor outperforms the best classical measurement with an improvement of $\approx 11\%$ in the sensitivity.

"Perhaps that is the secret. It is not what we do, so much as why we do it"

George R.R. Martin, *Game of Thrones*

"To define is to limit"

Oscar Wilde, *The Picture of Dorian Gray*

7 Conclusions and outlook

Summary

This manuscript summarizes the core of the activities I led during my PhD studies. They can be split in two lines of research. On the one hand a technological development of a new generation of balanced differential photo-detectors with real-time capabilities. On the other hand we have theoretically proposed and experimentally verified a new measurement protocol to detect the amplitude of arbitrarily chosen components of radio-frequency waveforms with quantum enhanced sensitivity.

First, we have demonstrated a pulsed differential photo-detector (DPD) and a detection system to make the signal available in real time. The DPD has bandwidth up to $\sim$11 MHz, which to our knowledge makes it the fastest quantum-noise-limited differential photo-detector for pulses with as few as 6.8×10^5 photons per pulse. We have made the signal available in real time by using analog electronics, namely, a pair of sample and hold (SHA) and a differential amplifier (DA). The DA is shot-noise-limited per input pulses varying from 7.4×10^5 to 3.7×10^8 photons per pulse and shows low latency, 170 ns. We have shown that the DPD together with the DA can directly be employed in real-time quantum control experiments with flexible measurement bandwidth varying from kHz up to 2.3 MHz.

Second, we have derived an analytical expression for the time evolution of the

spin operators under external radio-frequency magnetic field using perturbation theory. We relate the transverse noiseless spin displacement to the coherent accumulation of the radio-frequency perturbation. The noise in the measurement is contained in the spin variables. We have experimentally tested our theory for two different waveforms, sinusoidal and linearly chirped. We have demonstrated the selective response of the method in the coherent build-up of the perturbation signal with the programmed applied bias field. The combination of quantum non-demolition measurements and stroboscopic probing in a measure-evolve-measure sequence has allowed us to prepare the atoms in a spin squeezed state resulting in quantum sensing advantage, while also allowing full use of the system coherence. Using a cold atomic ensemble of $\sim 1.5 \times 10^6$ ^{87}Rb atoms, we have demonstrated entanglement-enhanced sensing with metrologically relevant noise reduction for sinusoidal and linearly chirped waveforms, with $\xi^2_{\mathrm{m}} = 0.84(8)$ and $\xi^2_{\mathrm{m}} = 0.80(3)$, respectively. The sensitivity-volume figure of merit achieved is comparable to the best radio-frequency magnetometers at these frequencies.

Outlook

The experiments presented and the technical tools developed in this thesis will enable advanced sensing of non-trivial waveforms. The first and more natural extensions of this work will be the detection of non-trivial time-varying frequency magnetic fields. The detection of signals of biological origin such as neuronal activity (MacGregor et al., 2012) or heart beats (Bison et al., 2009; Xia et al., 2006) is an active field from the biological and physical point of view. Recent experiments on neural impulses detection have shown sensitivities approaching quantum limits (Barry et al., 2016; Jensen et al., 2016), and detection of such signals can certainly benefit from the measurement protocol demonstrated in this manuscript.

An area of research where this technique can be advantageous is cosmological radio-frequency signals. Astronomical radio sources coming from planets and stars are extremely weak, and radio telescopes require very large antennas to collect enough radio energy to study them combined with highly sensitive detection equipment. A more exotic but not goofy application can be to search of extra-terrestrial civilizations (Cocconi and Morrion, 1959; Dyson, 1960; Siemion et al., 2013). It is known that some kind of radio emissions are produced only from artificial sources, and large radio-telescopes are build to search for these signals (Hall, 2005).

From the theoretical point of view there is a long list of questions that remain unanswered. We have shown that with prior information about the dynamics of the signal of interest coherent detection outperforms continuous measurements at sensing time-varying magnetic fields. The signal accumulated in a measurement

that uses the atomic coherence is proportional to the overlap integral between the time-varying signal and a pattern function. Only in the case when they are orthogonal, the signal accumulated is null. It would be an interesting problem to study the minimum information required *a priori* in a coherent-based detection in order to improve the sensitivity of a continuous measurement or rapid sampling strategies.

Complementary studies have been done in NV-center form magnetic field sensing where the sensors is described using qubits formalism rather than the continuous variable (Magesan et al., 2013). In these experiments the dynamic of the signal is unknown but the noise properties are identified. They can reconstruct not only the amplitude but also the complete field profile by means of dynamical decoupling pulses which cancel the noise. They are based on control sequence combining sets of π-pulses and Walsh functions (Cooper et al., 2014).

A more general problem in quantum sensing is to identify methods to perform dynamical parameter estimation while reducing the number of measurements but still have robust and high fidelity estimates. Proof-of-principle experiments have been done in magnetometry (Puentes et al., 2014). Robust methods have been proposed (Magesan et al., 2013) as well as theoretical works taking into account the effect of imperfect measurements (Candès et al., 2006).

Appendix A

As explained in Section 2.5.2, probing stroboscopically at twice the Larmor period is a method to cancel the tensorial rotation of the probe polarization. Here we demonstrate this statement using input-output relations between operators before (in) and after (out) the interaction, to first order in the interaction time τ. To keep the notation as simple as possible, it is convenient to define the single atom rank-2 tensor operators (Colangelo et al., 2013), for which we use the symbol $\hat{j}$, as

$$\hat{j}_{\mathrm{x}} = (\hat{f}_{\mathrm{x}})^2 - (\hat{f}_{\mathrm{y}})^2 \tag{A.1a}$$

$$\hat{j}_{\mathrm{y}} = \hat{f}_{\mathrm{x}}\hat{f}_{\mathrm{y}} + \hat{f}_{\mathrm{y}}\hat{f}_{\mathrm{x}} \tag{A.1b}$$

$$\hat{j}_{\mathrm{k}} = \hat{f}_{\mathrm{x}}\hat{f}_{\mathrm{z}} + \hat{f}_{\mathrm{z}}\hat{f}_{\mathrm{x}} \tag{A.1c}$$

$$\hat{j}_{\mathrm{l}} = \hat{f}_{\mathrm{y}}\hat{f}_{\mathrm{z}} + \hat{f}_{\mathrm{z}}\hat{f}_{\mathrm{y}} \tag{A.1d}$$

$$\hat{j}_{\mathrm{m}} = \frac{1}{\sqrt{3}}(2(\hat{f}_{\mathrm{z}})^2 - (\hat{f}_{\mathrm{x}})^2 - (\hat{f}_{\mathrm{y}})^2) \tag{A.1e}$$

The full interaction Hamiltonian can be written in the more compact form of

$$\tau\hat{H}_{\mathrm{int}} = g_1\hat{S}_{\mathrm{z}}\hat{F}_{\mathrm{z}} + g_2\left(\hat{S}_{\mathrm{x}}\hat{J}_{\mathrm{x}} + \hat{S}_{\mathrm{y}}\hat{J}_{\mathrm{y}} + \hat{S}_0\hat{J}_{\mathrm{m}}\right) \tag{A.2}$$

To obtain evolution of the light and atomic operators we use the Heisenberg equation of motion in the Heisenberg picture

$$\frac{d\hat{O}}{dt} = \frac{1}{i}[\hat{O}, \hat{H}_{\mathrm{int}}] \tag{A.3}$$

The output of the $\hat{F}_{\mathrm{z}}$ operator after a single optical pulse under the full Hamiltonian Eq. (A.2) is

$$\hat{F}_{\mathrm{z}}^{(\mathrm{out})} = \hat{F}_{\mathrm{z}} + 2g_2\left(\hat{S}_{\mathrm{x}}\hat{J}_{\mathrm{y}} - \hat{S}_{\mathrm{y}}\hat{J}_{\mathrm{x}}\right) \tag{A.4}$$

After the probing, the spins precess under the magnetic field along the y-axis. After evolving for a time $t = \pi/\omega_L$ the spins components $\hat{F}_{\mathrm{z}}$ and $\hat{F}_{\mathrm{x}}$ have flipped

sign. The atomic state is

$$\hat{F}_{\mathrm{z}}^{(\mathrm{mid})} = \hat{F}_{\mathrm{z}} - 2g_2\left(\hat{S}_{\mathrm{x}}\hat{J}_{\mathrm{y}} - \hat{S}_{\mathrm{y}}\hat{J}_{\mathrm{x}}\right) \tag{A.5}$$

The change on the state given by Eq. (A.5) caused by the probe is

$$\begin{aligned}\hat{F}_{\mathrm{z}}^{(\mathrm{end})} = &- \hat{F}_{\mathrm{z}} - 2g_2\hat{S}_{\mathrm{x}}\hat{J}_{\mathrm{y}} + g_2^2\left(4\hat{F}_{\mathrm{z}}(\hat{S}_{\mathrm{x}}^2 - \hat{S}_{\mathrm{y}}^2) + 2\hat{J}_{\mathrm{x}}^2\hat{S}_{\mathrm{z}} + 2\hat{J}_{\mathrm{y}}^2\hat{S}_{\mathrm{x}}\right)\\ &+ g_1g_2\left(2\hat{F}_{\mathrm{z}}(\hat{J}_{\mathrm{x}}\hat{S}_{\mathrm{x}} + \hat{J}_{\mathrm{y}}\hat{S}_{\mathrm{y}}) - 4\hat{J}_{\mathrm{x}}\hat{S}_{\mathrm{x}}\hat{S}_{\mathrm{z}} + 4\hat{J}_{\mathrm{y}}\hat{S}_{\mathrm{y}}\hat{S}_{\mathrm{z}}\right)\end{aligned} \tag{A.6}$$

The probe pulses are linearly polarized, and so only the $\langle\hat{S}_{\mathrm{x}}\rangle$ Stokes operators is large while the mean value of the other Stokes operators is small. Similarly, the atoms are spin polarized along the y-axis, with negligible mean value in the other components. Finally, $g_1 \propto \frac{1}{\Delta}$ and $g_2 \propto \frac{1}{\Delta^2}$. From scaling arguments, only the first two terms of Eq. (A.6) contribute to the mean value of the measured F_{z} component. There is a residual contribution of the tensor light-shift that the stroboscopic probing does not cancel, the term $2g_2\hat{S}_{\mathrm{x}}\hat{J}_{\mathrm{y}}$.

The measurement of the atomic components is done by detecting the $\hat{S}_{\mathrm{y}}$ Stokes component. The detected signal when the atoms are along the $+z$-axis is

$$\hat{S}_{\mathrm{y}}^{(\mathrm{out})} = \hat{S}_{\mathrm{y}} + g_1\hat{S}_{\mathrm{x}}\hat{F}_{\mathrm{z}} - g_2\hat{S}_{\mathrm{z}}\hat{J}_{\mathrm{x}} \tag{A.7}$$

Equivalently, when the atoms have rotated by a phase π, the measured optical rotation signal is

$$\begin{aligned}\hat{S}_{\mathrm{y}}^{(\mathrm{end})} = &\hat{S}_{\mathrm{y}} + g_1\left(-\hat{F}_{\mathrm{z}}\hat{S}_{\mathrm{x}} + g_2(-2\hat{J}_{\mathrm{y}}\hat{S}_{\mathrm{x}}^2 + 2\hat{J}_{\mathrm{x}}\hat{S}_{\mathrm{x}}\hat{S}_{\mathrm{y}} - \hat{F}_{\mathrm{z}}\hat{J}_{\mathrm{y}}\hat{S}_{\mathrm{z}} + 2\hat{J}_{\mathrm{y}}\hat{S}_{\mathrm{z}}^2)\right)\\ &+ \hat{F}_{\mathrm{z}}^2g_1^2\hat{S}_{\mathrm{y}} - 2g_2\hat{J}_{\mathrm{x}}\hat{S}_{\mathrm{z}} + g_2^2\left(2\hat{J}_{\mathrm{x}}(\hat{J}_{\mathrm{y}}\hat{S}_{\mathrm{x}} - \hat{J}_{\mathrm{x}}\hat{S}_{\mathrm{y}}) + 2\hat{F}_{\mathrm{z}}\hat{S}_{\mathrm{y}}\hat{S}_{\mathrm{z}}\right)\end{aligned} \tag{A.8}$$

Using the scaling argument as for the atomic evolution, we see that in Eq. (A.8) only the first two terms contribute to the mean measured optical signal. Comparing Eq. (A.7) and Eq. (A.8), we see a sign difference between the two expression. Because of the inversion of F_{z}, in order to compute statistics of a single measurement of F_{z} distributed in several pulses, there must be a sign difference between odd an even pulses, as expressed by Eq. (6.1).

Degree of Squeezing

All along the manuscript we have characterized the interaction strength through the coupling constant coefficient g_1. However, the coupling coefficient depends on the detuning of the Faraday probe. An alternative characterization of the light-atom interaction strength independent of the detuning is based on the definition

of the on-resonance optical depth d_0. Since ^{87}Rb is a multilevel atom with three relevant excited states, $f = 1 \rightarrow f' = \{0, 1, 2\}$, and the 'on-resonant' term might be confusing. We define the on-resonance in the case of large detuning where the main transition for the dispersive interaction is the $f = 1 \rightarrow f' = 0$. Although the atomic distribution is far from homogeneous, we define it in analogy with the usual definition of optical depth for a homogeneous medium Hammerer et al. (2004, 2010),

$$d_0 = \frac{\sigma_0}{A} N_{\mathrm{A}} \tag{A.9}$$

where $\sigma_0 = \frac{\lambda^2}{\pi}$ is the on-resonance scattering cross-section for atoms in $f = 1$. In turn, A characterizes the interaction area of light and atoms. We infer the interaction area from the measured value of g_1 and its definition, Koschorreck (2010):

$$g1(\Delta, A) = \frac{1}{A} \frac{\Gamma \lambda^2}{32\pi} \left(-\frac{4}{\Delta - \delta_0} - \frac{5}{\Delta - \delta_1} + \frac{5}{\Delta - \delta_2} \right) \tag{A.10}$$

where δ_i is the frequency difference between the lowest excited hyperfine level, $f' = 0$, and the level with i. The detuning from the resonance $f = 1 \rightarrow f' = 0$ is Δ, and take $\Delta < 0$ as red detuned. Γ is the excited state line-width. In Fig. A.1 we show the different scaling of g_1 with detuning.

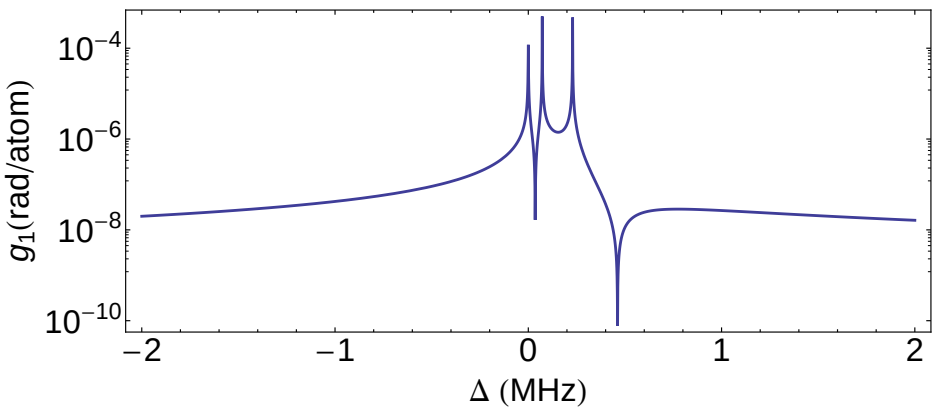

Figure A.1: Theory curve of the coupling constants for vector light shift (g_1) for the interesting region of detunings from transition $f = 1 \rightarrow f' = 0$. The interaction area was chosen to be $A = 4 \times 10^{-9}$ m^2, a value close to the estimated for our trap.

An equivalent definition of the interaction area is to say that it is the transverse area over which one could spread the atoms and light homogeneously and achieve

the same interaction strength as measured. For the measured value of $g_1 = 6.16(9)\times10^{-8}$ radian·atom^{-1}, we infer an effective interaction area of $A = 4.0(5)\times 10^{-9}\mathrm{m}^2$. With the maximum number of atoms in the ODT for the reported experiments, $N_\mathrm{A} = 1.54(2)\times10^6$, we estimate d_0=72(1).

If we ignore decoherence and loss mechanisms, the degree of squeezing for spin-1/2 particles has been shown Duan et al. (2000); Madsen and Mølmer (2004); Hammerer et al. (2004); de Echaniz et al. (2005) to be

$$\xi^2 = \frac{1}{1+d_0\eta} \tag{A.11}$$

where η is the number of photons scattered during the probing. As a side comment, comparable results are obtained using the signal-to-noise metric for the QND measurement, see Eq. (2.30). In this description, Eq. (A.11) can be written as

$$\xi^2 = \frac{1}{1+\kappa^2} \tag{A.12}$$

with $\kappa^2 = \tilde{g}_1^2 N_\mathrm{A} N_\mathrm{L}/2$, being N_A the number of atoms in the trap and N_L the number of photons used in the measurement.

It is possible to generalize Eq. (A.11) in the presence of decoherence and atoms loss, de Echaniz et al. (2005), to find

$$\xi^2 = \frac{1-\beta}{1+d_0\eta} + \eta\frac{1-\beta}{1-\eta} + \gamma\frac{1-\beta}{(1-\eta)^2} \tag{A.13}$$

where β is the number of scattered photons which produce atom losses and γ those that produce decoherence, with $\eta = \beta + \gamma$. For ^{87}Rb , $\gamma = \frac{5}{3}\beta$ according to the branching rations.

From Eq. (A.13), we find that the maximum squeezing is achieved for $\eta = 0.07$, resulting in $\xi^2 = 0.28$. The spin squeezed states generated in this thesis where prepared using different photon number, $N_\mathrm{L}^{(\mathrm{RF})} = 4\times10^8$ and $N_\mathrm{L}^{(\mathrm{C})} = 2.9\times10^8$ for constant field and chirped waveform detection, respectively. The corresponding scattered atom fractions are $\eta^{(\mathrm{RF})} = \eta_\mathrm{sc} N_\mathrm{L}^{(\mathrm{RF})} = 0.12$ and $\eta^{(\mathrm{C})} = \eta_\mathrm{sc} N_\mathrm{L}^{(\mathrm{C})} = 0.08$, where η_sc was reported on Sec. 3.4.3. From the scattered fractions we predict noise reductions of $\xi^2_{(\mathrm{RF})} = 0.32$ and $\xi^2_{(\mathrm{C})} = 0.29$, close to the theoretical optimal value.

The quantum enhanced atoms are let to evolve for a time t_hold where they acquire information about the magnetic field. During this time, the quantum correlations decay. Assuming two body correlations among the atoms, the squeezing will decay at a rate $\propto e^{-2t/\mathrm{T}_2}$, where T_2 is the atomic spin coherence time. With the experimental parameters ${t_\mathrm{hold}}^{(\mathrm{RF})}$ =300 µs and ${t_\mathrm{hold}}^{(\mathrm{C})}$ =600 µs and coherence times $\mathrm{T}_2^{(\mathrm{RF})}$ =4.8 ms and $\mathrm{T}_2^{(\mathrm{C})}$ =4.5 ms for constant and ramped bias field, respectively, we estimate the squeezing to be reduced by a factor 1.13 for the

quantum enhanced RF-magnetometer and 1.30 for the quantum enhanced waveform estimation. Thus, the ideal noise reduction we could have obtained with this system are $\xi^2_{(\mathrm{RF})} = 0.36$ for sinusoidal magnetic fields and $\xi^2_{(\mathrm{C})} = 0.37$ for magnetic waveforms.

We stress that this estimation is based on theoretical models for spin-1/2 systems. We exploit the spin-1 nature of the ground state of ^{87}Rb . In order to model and quantify this system more sophisticated descriptions, Colangelo et al. (2013) are needed.

Appendix B

In this Appendix we include the schematics for the Differential Photo-Detector (DPD) and for the Sample and Hold (SHA) detector which allows real time capabilities. Due to ICFO's intellectual property rights, the schematics have been simplified and some details have been omitted.

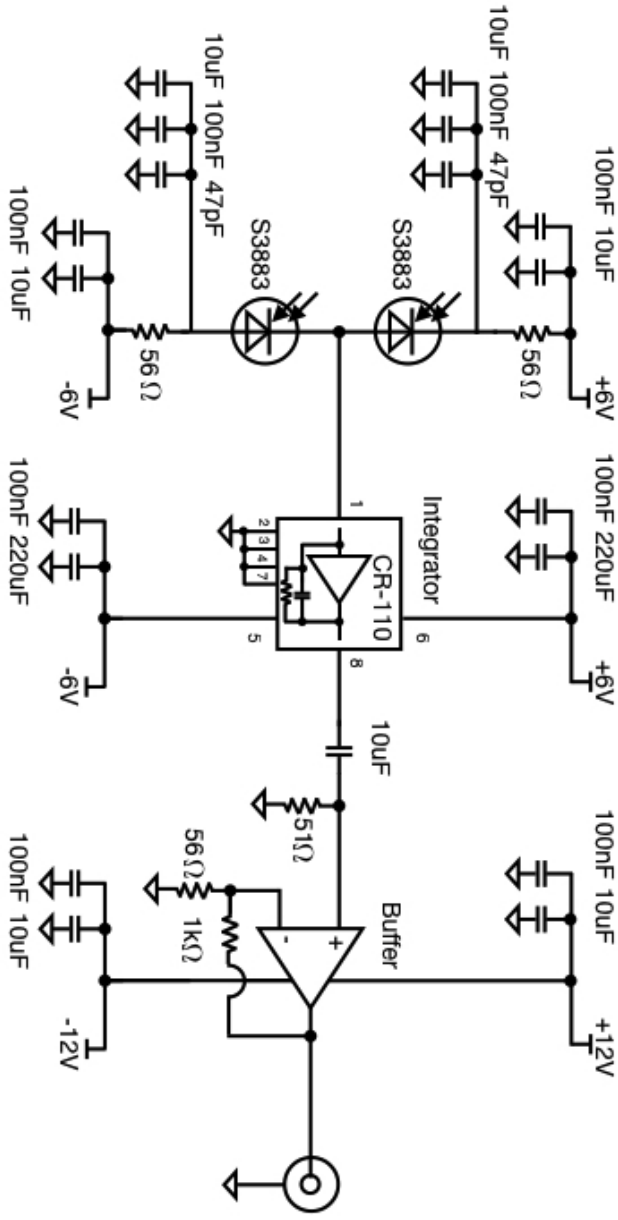

Figure B.2: Layout for the DPD.

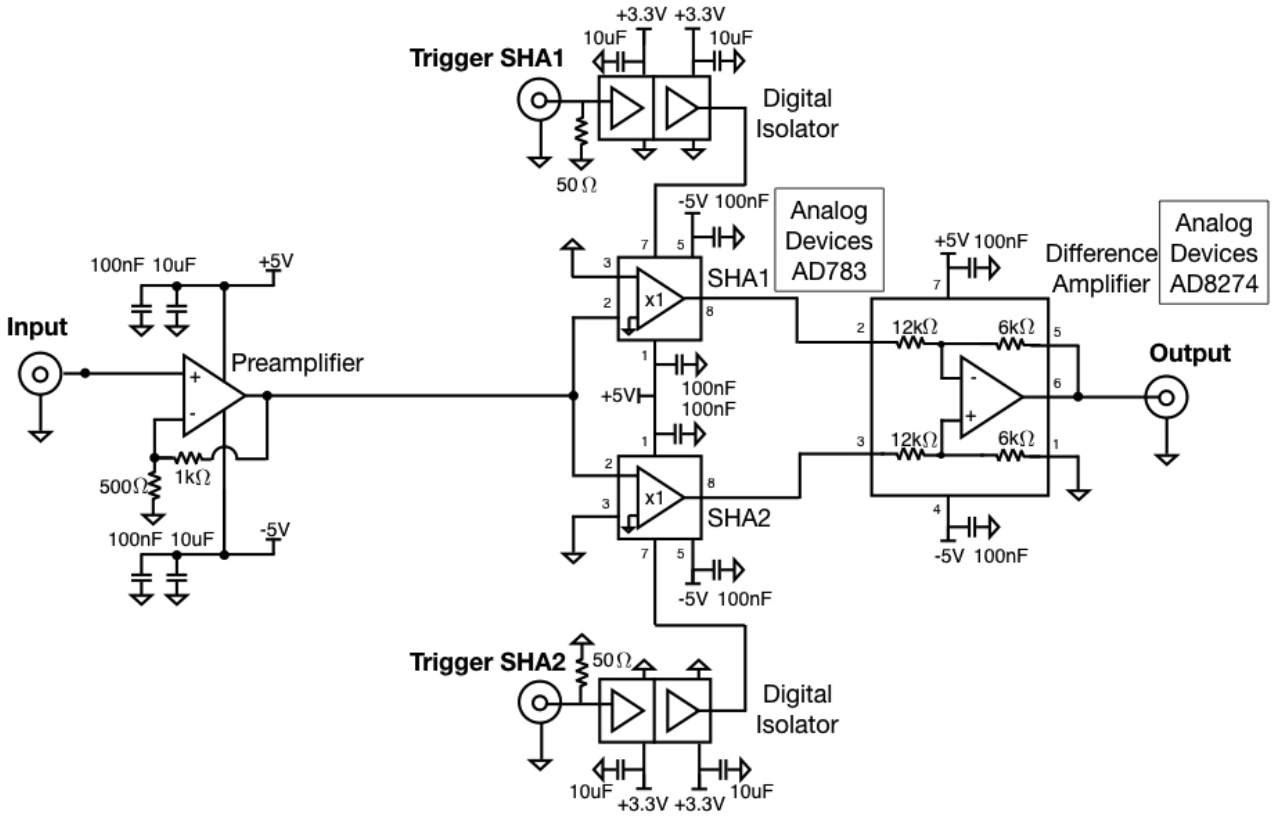

Figure B.3: Layout for the SHA detector.

"Personal isn't the same as important"
"Pride is all very well, but a sausage is a sausage"
Terry Pratchett, *Men at arms*

List of Publications

List of publications arising from this thesis:

F. Martin Ciurana, G. Colangelo, L. Slodička, R. J. Sewell and M. W. Mitchell, *Entanglement-enhanced radio-frequency field detection and waveform sensing*, Physical Review Letter **119**, 043603 (2017).

F. Martin Ciurana, G. Colangelo, R. J. Sewell and M. W. Mitchell, *Real-time shot-noise-limited differential photodetection for atomic quantum control*, Optics Letter **41**, 2946-2949 (2016).

During the time of my thesis I have been involved in other projects that are related with this thesis but not discussed here. They have been published somewhere.

G. Colangelo, F. Martin Ciurana, G. Puentes, M. W. Mitchell and R. J. Sewell, *Entanglement-enhanced phase estimation without prior phase information*, Physical Review Letter **118**, 233603 (2017)

G. Colangelo, F. Martin Ciurana, L. C. Bianchet, R. J. Sewell and M. W. Mitchell, *Simultaneous tracking of spin angle and amplitude beyond classical limits*, Nature **543**, 525-528 (2017)

N. Behbood, F. Martin Ciurana, G. Colangelo, M. Napolitano, G. Tóth, R. J. Sewell and M.W. Mitchell, *Generation of macroscopic singlet states in a cold atomic ensemble*, Physical Review Letter **113**, 093601 (2014)

R. J. Sewell, M. Napolitano, N. Behbood, G. Colangelo, F. Martin Ciurana and M. W. Mitchell, *Ultrasensitive atomic spin measurements with a nonlinear interferometer*, Physical Review X **4**, 021045 (2014)

G. Colangelo, R. J. Sewell, N. Behbood, F. Martin Ciurana, G. Triginer and M. W. Mitchell, *Quantum atom-light interfaces in the Gaussian description for*

spin-1 systems, New Journal of Physics, **15**, 103007 (2013)

N. Behbood, G. Colangelo, F. Martin Ciurana, M. Napolitano, R. J. Sewell and M. W. Mitchell, *Feedback cooling of an atomic spin ensemble*, Physical Review Letter **111**, 103601 (2013)

N. Behbood, F. Martin Ciurana, G. Colangelo, M. Napolitano, M. W. Mitchell and R. J. Sewell, *Real-time vector field tracking with a cold-atom magnetometer*, Applied Physics Letter **102**, 173504 (2013)

Results under peer-review:
G. Vitagliano, G. Colangelo, F. Martin Ciurana, M. W. Mitchell, R. J. Sewell and G. Tóth, *Entanglement and extreme planar spin squeezing*, submitted to Physics Review Letter.

Bibliography

A. Abragam. The Principles of Nuclear Magnetism. Oxford University Press, 1961.

F. Allmendinger, W. Heil, S. Karpuk, W. Kilian, A. Scharth, U. Schmidt, A. Schnabel, Yu. Sobolev, and K. Tullney. New limit on lorentz-invariance- and *cpt*-violating neutron spin interactions using a free-spin-precession ^{3}He-^{129}Xe comagnetometer. Phys. Rev. Lett., 112:110801, Mar 2014. doi: 10.1103/PhysRevLett.112.110801. URL https://link.aps.org/doi/10.1103/PhysRevLett.112.110801.

A. André, A. S. Sørensen, and M. D. Lukin. Stability of atomic clocks based on entangled atoms. Phys. Rev. Lett., 92:230801, Jun 2004. doi: 10.1103/PhysRevLett.92.230801. URL http://link.aps.org/doi/10.1103/PhysRevLett.92.230801.

J. Appel, P. J. Windpassinger, D. Oblak, U. B. Hoff, N. Kjærgaard, and E. S. Polzik. Mesoscopic atomic entanglement for precision measurements beyond the standard quantum limit. Proc. Nat. Acad. Sci., 106(27):10960–10965, 2009. doi: 10.1073/pnas.0901550106. URL http://www.pnas.org/content/106/27/10960.abstract.

M. Auzinsh, D. Budker, D. F. Kimball, S. M. Rochester, J. E. Stalnaker, A. O. Sushkov, and V. V. Yashchuk. Can a quantum nondemolition measurement improve the sensitivity of an atomic magnetometer? Phys. Rev. Lett., 93:173002, Oct 2004. doi: 10.1103/PhysRevLett.93.173002. URL http://link.aps.org/doi/10.1103/PhysRevLett.93.173002.

H.A. Bachor and T.C. Ralph. A Guide to Experiments in Quantum Optics. Wiley, 2004. ISBN 9783527403936. URL https://books.google.es/books?id=7yCLQgAACAAJ.

Ben Q. Baragiola, Leigh M. Norris, Enrique Montaño, Pascal G. Mickelson, Poul S. Jessen, and Ivan H. Deutsch. Three-dimensional light-matter interface for collective spin squeezing in atomic ensembles. Phys. Rev. A, 89:033850,

Mar 2014. doi: 10.1103/PhysRevA.89.033850. URL https://link.aps.org/doi/10.1103/PhysRevA.89.033850.

John F. Barry, Matthew J. Turner, Jennifer M. Schloss, David R. Glenn, Yuyu Song, Mikhail D. Lukin, Hongkun Park, and Ronald L. Walsworth. Optical magnetic detection of single-neuron action potentials using quantum defects in diamond. Proceedings of the National Academy of Sciences, 113(49):14133–14138, 2016.

J.-B. Béguin, E. M. Bookjans, S. L. Christensen, H. L. Sørensen, J. H. Müller, E. S. Polzik, and J. Appel. Generation and detection of a sub-poissonian atom number distribution in a one-dimensional optical lattice. Phys. Rev. Lett., 113:263603, Dec 2014. doi: 10.1103/PhysRevLett.113.263603. URL http://link.aps.org/doi/10.1103/PhysRevLett.113.263603.

N. Behbood, G. Colangelo, F. Martin Ciurana, M. Napolitano, R. J. Sewell, and M. W. Mitchell. Feedback cooling of an atomic spin ensemble. Phys. Rev. Lett., 111:103601, Sep 2013a. doi: 10.1103/PhysRevLett.111.103601. URL http://link.aps.org/doi/10.1103/PhysRevLett.111.103601.

N. Behbood, F. Martin Ciurana, G. Colangelo, M. Napolitano, M. W. Mitchell, and R. J. Sewell. Real-time vector field tracking with a cold-atom magnetometer. Applied Physics Letters, 102(17):173504, 2013b. doi: http://dx.doi.org/10.1063/1.4803684. URL http://scitation.aip.org/content/aip/journal/apl/102/17/10.1063/1.4803684.

Naeimeh Behbood. Generation of Macroscopic Spin Singlets in Cold Atomic Ensembles. PhD thesis, ICFO-UPC, 2015.

William E. Bell and Arnold L. Bloom. Optical detection of magnetic resonance in alkali metal vapor. Phys. Rev., 107:1559–1565, Sep 1957. doi: 10.1103/PhysRev.107.1559. URL https://link.aps.org/doi/10.1103/PhysRev.107.1559.

G. Bison, N. Castagna, A. Hofer, P. Knowles, J.-L. Schenker, M. Kasprzak, H. Saudan, and A. Weis. A room temperature 19-channel magnetic field mapping device for cardiac signals. Applied Physics Letters, 95(17):173701, 2009. doi: 10.1063/1.3255041. URL http://dx.doi.org/10.1063/1.3255041.

F. Bloch. Nuclear induction. Phys. Rev., 70:460–474, Oct 1946. doi: 10.1103/PhysRev.70.460. URL https://link.aps.org/doi/10.1103/PhysRev.70.460.

M. S. Blok, C. Bonato, M. L. Markham, D. J. Twitchen, V. V. Dobrovitski, and R. Hanson. Manipulating a qubit through the backaction of sequential partial

measurements and real-time feedback. Nat Phys, 10(3):189–193, 03 2014. URL http://dx.doi.org/10.1038/nphys2881.

B. J. Bloom, T. L. Nicholson, J. R. Williams, S. L. Campbell, M. Bishof, X. Zhang, W. Zhang, S. L. Bromley, and J. Ye. An optical lattice clock with accuracy and stability at the 10-18 level. Nature, 506(7486):71–75, 02 2014. URL http://dx.doi.org/10.1038/nature12941.

J. G. Bohnet, K. C. Cox, M. A. Norcia, J. M. Weiner, Z. Chen, and J. K. Thompson. Reduced spin measurement back-action for a phase sensitivity ten times beyond the standard quantum limit. Nat Photon, 8(9):731–736, 09 2014. URL http://dx.doi.org/10.1038/nphoton.2014.151.

C. Bonato, M. S. Blok, H. T. Dinani, D. W. Berry, M. L. Markham, D. J. Twitchen, and R. Hanson. Optimized quantum sensing with a single electron spin using real-time adaptive measurements. Nat Nano, 11(3):247–252, 03 2016. URL http://dx.doi.org/10.1038/nnano.2015.261.

Rym Bouchendira, Pierre Cladé, Saïda Guellati-Khélifa, François Nez, and François Biraben. New determination of the fine structure constant and test of the quantum electrodynamics. Phys. Rev. Lett., 106:080801, Feb 2011. doi: 10.1103/PhysRevLett.106.080801. URL https://link.aps.org/doi/10.1103/PhysRevLett.106.080801.

Vladimir B. Braginsky, Yuri I. Vorontsov, and Kip S. Thorne. Quantum nondemolition measurements. Science, 209(4456):547–557, 1980. ISSN 0036-8075. doi: 10.1126/science.209.4456.547. URL http://science.sciencemag.org/content/209/4456/547.

D. Budker, W. Gawlik, D. F. Kimball, S. M. Rochester, V. V. Yashchuk, and A. Weis. Resonant nonlinear magneto-optical effects in atoms. Rev. Mod. Phys., 74:1153–1201, Nov 2002. doi: 10.1103/RevModPhys.74.1153. URL https://link.aps.org/doi/10.1103/RevModPhys.74.1153.

Dmitry Budker and Michael Romalis. Optical magnetometry. Nat Phys, 3(4):227–234, 04 2007. URL http://dx.doi.org/10.1038/nphys566.

le Bureau Internationel des Poids et Mesures. http://www.bipm.org/en/publications/si-brochure/second.html. URL http://www.bipm.org/en/publications/si-brochure/second.html.

Emmanuel J. Candès, Justin K. Romberg, and Terence Tao. Stable signal recovery from incomplete and inaccurate measurements. Communications on Pure and Applied Mathematics, 59(8):1207–1223, 2006. ISSN 1097-0312. doi: 10.1002/cpa.20124. URL http://dx.doi.org/10.1002/cpa.20124.

W. Chaibi, R. Geiger, B. Canuel, A. Bertoldi, A. Landragin, and P. Bouyer. Low frequency gravitational wave detection with ground-based atom interferometer arrays. Phys. Rev. D, 93:021101, Jan 2016. doi: 10.1103/PhysRevD.93.021101. URL https://link.aps.org/doi/10.1103/PhysRevD.93.021101.

W. Chalupczak, R. M. Godun, S. Pustelny, and W. Gawlik. Room temperature femtotesla radio-frequency atomic magnetometer. Applied Physics Letters, 100(24):242401, 2012. doi: 10.1063/1.4729016. URL http://dx.doi.org/10.1063/1.4729016.

Zilong Chen, Justin G. Bohnet, Shannon R. Sankar, Jiayan Dai, and James K. Thompson. Conditional spin squeezing of a large ensemble via the vacuum rabi splitting. Phys. Rev. Lett., 106:133601, Mar 2011. doi: 10.1103/PhysRevLett.106.133601. URL http://link.aps.org/doi/10.1103/PhysRevLett.106.133601.

Giuseppe Cocconi and Philip Morrion. Searching for interstellar communications. Nature, 184(4690):844–846, 09 1959. URL http://dx.doi.org/10.1038/184844a0.

G. Colangelo, F. Martin Ciurana, G. Puentes, M. W. Mitchell, and R. J. Sewell. Entanglement-enhanced phase estimation without prior phase information. Phys. Rev. Lett., 118:233603, Jun 2017a. doi: 10.1103/PhysRevLett.118.233603. URL https://link.aps.org/doi/10.1103/PhysRevLett.118.233603.

Giorgio Colangelo. Quantum Measurements with Cold Atomic Ensembles. PhD thesis, ICFO - UPC, 2016.

Giorgio Colangelo, Robert J Sewell, Naeimeh Behbood, Ferran Martin Ciurana, Gil Triginer, and Morgan W Mitchell. Quantum atom–light interfaces in the gaussian description for spin-1 systems. New Journal of Physics, 15(10):103007, 2013. URL http://stacks.iop.org/1367-2630/15/i=10/a=103007.

Giorgio Colangelo, Ferran Martin Ciurana, Lorena C. Bianchet, Robert J. Sewell, and Morgan W. Mitchell. Simultaneous tracking of spin angle and amplitude beyond classical limits. Nature, 543(7646):525–528, 03 2017b. URL http://dx.doi.org/10.1038/nature21434.

A. Cooper, E. Magesan, H. N. Yum, and P. Cappellaro. Time-resolved magnetic sensing with electronic spins in diamond. Nature Communications, 5:3141 EP, 01 2014. URL http://dx.doi.org/10.1038/ncomms4141.

Kevin C. Cox, Graham P. Greve, Joshua M. Weiner, and James K. Thompson. Deterministic squeezed states with collective measurements and feedback. Phys. Rev. Lett., 116:093602, Mar 2016. doi: 10.1103/PhysRevLett.116.093602. URL https://link.aps.org/doi/10.1103/PhysRevLett.116.093602.

Herbert Crepaz. Trapping and cooling rubidium atoms for quantum information. PhD thesis, Faculty of Mathematics, Computer Science and Physics of the University of Innsbruck, 2006.

H. B. Dang, A. C. Maloof, and M. V. Romalis. Ultrahigh sensitivity magnetic field and magnetization measurements with an atomic magnetometer. Applied Physics Letters, 97(15):151110, 2010. doi: 10.1063/1.3491215. URL http://dx.doi.org/10.1063/1.3491215.

Nir Davidson, Heun Jin Lee, Charles S. Adams, Mark Kasevich, and Steven Chu. Long atomic coherence times in an optical dipole trap. Phys. Rev. Lett., 74:1311–1314, Feb 1995. doi: 10.1103/PhysRevLett.74.1311. URL https://link.aps.org/doi/10.1103/PhysRevLett.74.1311.

S. R. de Echaniz, M. W. Mitchell, M. Kubasik, M. Koschorreck, H. Crepaz, J. Eschner, and E. S. Polzik. Conditions for spin squeezing in a cold 87 rb ensemble. Journal of Optics B: Quantum and Semiclassical Optics, 7(12):S548, 2005. URL http://stacks.iop.org/1464-4266/7/i=12/a=016.

S. R. de Echaniz, M. Koschorreck, M. Napolitano, M. Kubasik, and M. W. Mitchell. Hamiltonian design in atom-light interactions with rubidium ensembles: A quantum-information toolbox. Phys. Rev. A, 77:032316, Mar 2008. doi: 10.1103/PhysRevA.77.032316. URL https://link.aps.org/doi/10.1103/PhysRevA.77.032316.

Y. Natali Martinez de Escobar, Silvana Palacios Álvarez, Simon Coop, Thomas Vanderbruggen, Krzysztof T. Kaczmarek, and Morgan W. Mitchell. Absolute frequency references at 1529 and 1560nm using modulation transfer spectroscopy. Opt. Lett., 40(20):4731–4734, Oct 2015. doi: 10.1364/OL.40.004731. URL http://ol.osa.org/abstract.cfm?URI=ol-40-20-4731.

Yannick A. de Icaza Astiz, Vito Giovanni Lucivero, R. de J. León-Montiel, and Morgan W. Mitchell. Optimal signal recovery for pulsed balanced detection. Phys. Rev. A, 90:033814, Sep 2014. doi: 10.1103/PhysRevA.90.033814. URL http://link.aps.org/doi/10.1103/PhysRevA.90.033814.

C. L. Degen, F. Reinhard, and P. Cappellaro. Quantum sensing. Rev. Mod. Phys., 89:035002, Jul 2017. doi: 10.1103/RevModPhys.89.035002. URL https://link.aps.org/doi/10.1103/RevModPhys.89.035002.

H. G. Dehmelt. Modulation of a light beam by precessing absorbing atoms. Phys. Rev., 105:1924–1925, Mar 1957a. doi: 10.1103/PhysRev.105.1924. URL https://link.aps.org/doi/10.1103/PhysRev.105.1924.

H. G. Dehmelt. Slow spin relaxation of optically polarized sodium atoms. Phys. Rev., 105:1487–1489, Mar 1957b. doi: 10.1103/PhysRev.105.1487. URL https://link.aps.org/doi/10.1103/PhysRev.105.1487.

Savas Dimopoulos, Peter W. Graham, Jason M. Hogan, Mark A. Kasevich, and Surjeet Rajendran. Atomic gravitational wave interferometric sensor. Phys. Rev. D, 78:122002, Dec 2008. doi: 10.1103/PhysRevD.78.122002. URL https://link.aps.org/doi/10.1103/PhysRevD.78.122002.

Lu-Ming Duan, J. I. Cirac, P. Zoller, and E. S. Polzik. Quantum communication between atomic ensembles using coherent light. Phys. Rev. Lett., 85:5643–5646, Dec 2000. doi: 10.1103/PhysRevLett.85.5643. URL https://link.aps.org/doi/10.1103/PhysRevLett.85.5643.

Brice Dubost. Light-Matter Interaction with Atomic Ensembles. PhD thesis, ICFO - UPC, 2012.

I. Dutta, D. Savoie, B. Fang, B. Venon, C. L. Garrido Alzar, R. Geiger, and A. Landragin. Continuous cold-atom inertial sensor with 1 nrad/sec rotation stability. Phys. Rev. Lett., 116:183003, May 2016. doi: 10.1103/PhysRevLett.116.183003. URL https://link.aps.org/doi/10.1103/PhysRevLett.116.183003.

Freeman J. Dyson. Search for artificial stellar sources of infrared radiation. Science, 131(3414):1667–1668, 1960. ISSN 0036-8075. doi: 10.1126/science.131.3414.1667. URL http://science.sciencemag.org/content/131/3414/1667.

J. Esteve, C. Gross, A. Weller, S. Giovanazzi, and M. K. Oberthaler. Squeezing and entanglement in a bose-einstein condensate. Nature, 455(7217):1216–1219, 10 2008. URL http://dx.doi.org/10.1038/nature07332.

T. Fernholz, H. Krauter, K. Jensen, J. F. Sherson, A. S. Sørensen, and E. S. Polzik. Spin squeezing of atomic ensembles via nuclear-electronic spin entanglement. Phys. Rev. Lett., 101:073601, Aug 2008. doi: 10.1103/PhysRevLett.101.073601. URL http://link.aps.org/doi/10.1103/PhysRevLett.101.073601.

Naceur Gaaloul, H. Ahlers, T.A. Schulze, Y. Singh, S.T. Seidel, W. Herr, W. Ertmer, and E. Rasel. Quantum tests of the equivalence principle with atom

interferometry. Acta Astronautica, 67(9):1059 – 1062, 2010. ISSN 0094-5765. doi: http://dx.doi.org/10.1016/j.actaastro.2010.06.043. URL http://www.sciencedirect.com/science/article/pii/S0094576510002341.

M. Gajdacz, A. J. Hilliard, M. A. Kristensen, P. L. Pedersen, C. Klempt, J. J. Arlt, and J. F. Sherson. Preparation of ultracold atom clouds at the shot noise level. Phys. Rev. Lett., 117:073604, Aug 2016. doi: 10.1103/PhysRevLett.117.073604. URL http://link.aps.org/doi/10.1103/PhysRevLett.117.073604.

R. Geiger, V. Ménoret, G. Stern, N. Zahzam, P. Cheinet, B. Battelier, A. Villing, F. Moron, M. Lours, Y. Bidel, A. Bresson, A. Landragin, and P. Bouyer. Detecting inertial effects with airborne matter-wave interferometry. Nature Communications, 2:474 EP, 09 2011. URL http://dx.doi.org/10.1038/ncomms1479.

J. M. Geremia, John K. Stockton, and Hideo Mabuchi. Tensor polarizability and dispersive quantum measurement of multilevel atoms. Phys. Rev. A, 73:042112, Apr 2006. doi: 10.1103/PhysRevA.73.042112. URL https://link.aps.org/doi/10.1103/PhysRevA.73.042112.

J.M. Geremia, John K. Stockton, and Hideo Mabuchi. Real-time quantum feedback control of atomic spin-squeezing. Science, 304(5668):270–273, 2004. ISSN 0036-8075. doi: 10.1126/science.1095374. URL http://science.sciencemag.org/content/304/5668/270.

P. Gillot, O. Francis, A. Landragin, F. Pereira Dos Santos, and S. Merlet. Stability comparison of two absolute gravimeters: optical versus atomic interferometers. Metrologia, 51(5):L15, 2014. URL http://stacks.iop.org/0026-1394/51/i=5/a=L15.

Vittorio Giovannetti, Seth Lloyd, and Lorenzo Maccone. Advances in quantum metrology. Nat Photon, 5(4):222–229, 04 2011. URL http://dx.doi.org/10.1038/nphoton.2011.35.

P. Grangier, R. E. Slusher, B. Yurke, and A. LaPorta. Squeezed-light–enhanced polarization interferometer. Phys. Rev. Lett., 59:2153–2156, Nov 1987. doi: 10.1103/PhysRevLett.59.2153. URL https://link.aps.org/doi/10.1103/PhysRevLett.59.2153.

Robert D. Guenther. Modern Optics. Wiley, 1990.

E. L. Hahn. Spin echoes. Phys. Rev., 80:580–594, Nov 1950. doi: 10.1103/PhysRev.80.580. URL https://link.aps.org/doi/10.1103/PhysRev.80.580.

J. Hald, J. L. Sørensen, C. Schori, and E. S. Polzik. Spin squeezed atoms: A macroscopic entangled ensemble created by light. Phys. Rev. Lett., 83:1319–1322, Aug 1999. doi: 10.1103/PhysRevLett.83.1319. URL https://link.aps.org/doi/10.1103/PhysRevLett.83.1319.

Peter Hall. The Square Kilometre Array: An Engineering Perspective. Springer-Verlag New York, 2005.

K. Hammerer, K. Mølmer, E. S. Polzik, and J. I. Cirac. Light-matter quantum interface. Phys. Rev. A, 70:044304, Oct 2004. doi: 10.1103/PhysRevA.70.044304. URL https://link.aps.org/doi/10.1103/PhysRevA.70.044304.

Klemens Hammerer, Anders S. Sørensen, and Eugene S. Polzik. Quantum interface between light and atomic ensembles. Rev. Mod. Phys., 82:1041–1093, Apr 2010. doi: 10.1103/RevModPhys.82.1041. URL https://link.aps.org/doi/10.1103/RevModPhys.82.1041.

H. Hansen, T. Aichele, C. Hettich, P. Lodahl, A. I. Lvovsky, J. Mlynek, and S. Schiller. Ultrasensitive pulsed, balanced homodyne detector: application to time-domain quantum measurements. Opt. Lett., 26(21):1714–1716, Nov 2001.

N. Hinkley, J. A. Sherman, N. B. Phillips, M. Schioppo, N. D. Lemke, K. Beloy, M. Pizzocaro, C. W. Oates, and A. D. Ludlow. An atomic clock with 10-18 instability. Science, 341(6151):1215–1218, 2013. ISSN 0036-8075. doi: 10.1126/science.1240420. URL http://science.sciencemag.org/content/early/2013/08/21/science.1240420.

M. J. Holland, M. J. Collett, D. F. Walls, and M. D. Levenson. Nonideal quantum nondemolition measurements. Phys. Rev. A, 42:2995–3005, Sep 1990. doi: 10.1103/PhysRevA.42.2995. URL https://link.aps.org/doi/10.1103/PhysRevA.42.2995.

O. Hosten, R. Krishnakumar, N. J. Engelsen, and M. A. Kasevich. Quantum phase magnification. Science, 352(6293):1552–1555, 2016a. ISSN 0036-8075. doi: 10.1126/science.aaf3397. URL http://science.sciencemag.org/content/352/6293/1552.

Onur Hosten, Nils J. Engelsen, Rajiv Krishnakumar, and Mark A. Kasevich. Measurement noise 100 times lower than the quantum-projection limit using entangled atoms. Nature, 529(7587):505–508, 01 2016b. URL http://dx.doi.org/10.1038/nature16176.

S. F. Huelga, C. Macchiavello, T. Pellizzari, A. K. Ekert, M. B. Plenio, and J. I. Cirac. Improvement of frequency standards with quantum entanglement. Phys.

Rev. Lett., 79:3865–3868, Nov 1997. doi: 10.1103/PhysRevLett.79.3865. URL http://link.aps.org/doi/10.1103/PhysRevLett.79.3865.

Mills Ian. Draft Chapter 2 for SI Brochure following redefinitions of the base units. BIPM, 2012.

Ryotaro Inoue, Shin-Ichi-Ro Tanaka, Ryo Namiki, Takahiro Sagawa, and Yoshiro Takahashi. Unconditional quantum-noise suppression via measurement-based quantum feedback. Phys. Rev. Lett., 110:163602, Apr 2013. doi: 10.1103/PhysRevLett.110.163602. URL http://link.aps.org/doi/10.1103/PhysRevLett.110.163602.

W. M. Itano, J. C. Bergquist, J. J. Bollinger, J. M. Gilligan, D. J. Heinzen, F. L. Moore, M. G. Raizen, and D. J. Wineland. Quantum projection noise: Population fluctuations in two-level systems. Phys. Rev. A, 47:3554–3570, May 1993. doi: 10.1103/PhysRevA.47.3554. URL http://link.aps.org/doi/10.1103/PhysRevA.47.3554.

Kasper Jensen, Rima Budvytyte, Rodrigo A. Thomas, Tian Wang, Annette M. Fuchs, Mikhail V. Balabas, Georgios Vasilakis, Lars D. Mosgaard, Hans C. Stærkind, Jörg H. Müller, Thomas Heimburg, Søren-Peter Olesen, and Eugene S. Polzik. Non-invasive detection of animal nerve impulses with an atomic magnetometer operating near quantum limited sensitivity. Scientific Reports, 6:29638 EP –, 07 2016. URL http://dx.doi.org/10.1038/srep29638.

W. Ketterle, D. S. Durfee, and D. M. Stamper-Kurn. Making, probing and understanding bose-einstein condensates. eprint arXiv:cond-mat/9904034, 1999.

Masahiro Kitagawa and Masahito Ueda. Squeezed spin states. Phys. Rev. A, 47:5138–5143, Jun 1993. doi: 10.1103/PhysRevA.47.5138. URL https://link.aps.org/doi/10.1103/PhysRevA.47.5138.

I. K. Kominis, T. W. Kornack, J. C. Allred, and M. V. Romalis. A subfemtotesla multichannel atomic magnetometer. Nature, 422(6932):596–599, 04 2003. URL http://dx.doi.org/10.1038/nature01484.

M. Koschorreck, M. Napolitano, B. Dubost, and M. W. Mitchell. Sub-projection-noise sensitivity in broadband atomic magnetometry. Phys. Rev. Lett., 104:093602, Mar 2010a. doi: 10.1103/PhysRevLett.104.093602. URL http://link.aps.org/doi/10.1103/PhysRevLett.104.093602.

M. Koschorreck, M. Napolitano, B. Dubost, and M. W. Mitchell. Quantum nondemolition measurement of large-spin ensembles by dynamical decoupling. Phys. Rev. Lett., 105:093602, Aug 2010b. doi: 10.1103/PhysRevLett.

105.093602. URL http://link.aps.org/doi/10.1103/PhysRevLett.105.093602.

Marco Koschorreck. Generation of Spin Squeezing in an Ensemble of Cold Rubidium 87. PhD thesis, ICFO-UPC, 2010.

M. A. Kristensen, M. Gajdacz, P. L. Pedersen, C. Klempt, J. F. Sherson, J. J. Arlt, and A. J. Hilliard. Sub-atom shot noise faraday imaging of ultracold atom clouds. Journal of Physics B: Atomic, Molecular and Optical Physics, 50(3): 034004, 2017. URL http://stacks.iop.org/0953-4075/50/i=3/a=034004.

M. Kubasik, M. Koschorreck, M. Napolitano, S. R. de Echaniz, H. Crepaz, J. Eschner, E. S. Polzik, and M. W. Mitchell. Polarization-based light-atom quantum interface with an all-optical trap. Phys. Rev. A, 79:043815, Apr 2009. doi: 10.1103/PhysRevA.79.043815. URL http://link.aps.org/doi/10.1103/PhysRevA.79.043815.

Marcin Kubasik. Towards Spin Squeezing in Cold Atomic Ensembles. PhD thesis, ICFO - UPC, 2009.

S. J. M. Kuppens, K. L. Corwin, K. W. Miller, T. E. Chupp, and C. E. Wieman. Loading an optical dipole trap. Phys. Rev. A, 62:013406, Jun 2000. doi: 10.1103/PhysRevA.62.013406. URL https://link.aps.org/doi/10.1103/PhysRevA.62.013406.

D. V. Kupriyanov, O. S. Mishina, I. M. Sokolov, B. Julsgaard, and E. S. Polzik. Multimode entanglement of light and atomic ensembles via off-resonant coherent forward scattering. Phys. Rev. A, 71:032348, Mar 2005. doi: 10.1103/PhysRevA.71.032348. URL https://link.aps.org/doi/10.1103/PhysRevA.71.032348.

A. Kuzmich, N. P. Bigelow, and L. Mandel. Atomic quantum non-demolition measurements and squeezing. Europhys. Lett., 42(5):481–486, 1998. doi: 10.1209/epl/i1998-00277-9. URL http://dx.doi.org/10.1209/epl/i1998-00277-9.

A. Kuzmich, L. Mandel, and N. P. Bigelow. Generation of spin squeezing via continuous quantum nondemolition measurement. Phys. Rev. Lett., 85:1594–1597, Aug 2000. doi: 10.1103/PhysRevLett.85.1594. URL https://link.aps.org/doi/10.1103/PhysRevLett.85.1594.

S.-K. Lee, K. L. Sauer, S. J. Seltzer, O. Alem, and M. V. Romalis. Subfemtotesla radio-frequency atomic magnetometer for detection of nuclear quadrupole resonance. Applied Physics Letters, 89(21):214106, 2006. doi: http://dx.doi.org/10.1063/1.2390643. URL http://scitation.aip.org/content/aip/journal/apl/89/21/10.1063/1.2390643.

Ian D. Leroux, Monika H. Schleier-Smith, and Vladan Vuletić. Implementation of cavity squeezing of a collective atomic spin. Phys. Rev. Lett., 104:073602, Feb 2010a. doi: 10.1103/PhysRevLett.104.073602. URL http://link.aps.org/doi/10.1103/PhysRevLett.104.073602.

Ian D. Leroux, Monika H. Schleier-Smith, and Vladan Vuletić. Orientation-dependent entanglement lifetime in a squeezed atomic clock. Phys. Rev. Lett., 104:250801, Jun 2010b. doi: 10.1103/PhysRevLett.104.250801. URL https://link.aps.org/doi/10.1103/PhysRevLett.104.250801.

P. D. Lett, W. D. Phillips, S. L. Rolston, C. E. Tanner, R. N. Watts, and C. I. Westbrook. Optical molasses. J. Opt. Soc. Am. B, 6(11):2084–2107, Nov 1989. doi: 10.1364/JOSAB.6.002084. URL http://josab.osa.org/abstract.cfm?URI=josab-6-11-2084.

LIGO. A gravitational wave observatory operating beyond the quantum shot-noise limit. Nat Phys, 7(12):962–965, 12 2011. URL http://dx.doi.org/10.1038/nphys2083.

LIGO. Enhanced sensitivity of the ligo gravitational wave detector by using squeezed states of light. Nat Photon, 7(8):613–619, 08 2013. URL http://dx.doi.org/10.1038/nphoton.2013.177.

Seth Lloyd. Coherent quantum feedback. Phys. Rev. A, 62:022108, Jul 2000. doi: 10.1103/PhysRevA.62.022108. URL https://link.aps.org/doi/10.1103/PhysRevA.62.022108.

Vito Giovanni Lucivero, Ricardo Jiménez-Martínez, Jia Kong, and Morgan W. Mitchell. Squeezed-light spin noise spectroscopy. Phys. Rev. A, 93:053802, May 2016. doi: 10.1103/PhysRevA.93.053802. URL https://link.aps.org/doi/10.1103/PhysRevA.93.053802.

Jian Ma, Xiaoguang Wang, C.P. Sun, and Franco Nori. Quantum spin squeezing. Physics Reports, 509(2–3):89 – 165, 2011. ISSN 0370-1573. doi: https://doi.org/10.1016/j.physrep.2011.08.003. URL http://www.sciencedirect.com/science/article/pii/S0370157311002201.

Lucy J. MacGregor, Friedemann Pulvermüller, Maarten van Casteren, and Yury Shtyrov. Ultra-rapid access to words in the brain. Nature Communications, 3:711 EP, 02 2012. URL http://dx.doi.org/10.1038/ncomms1715.

Lars Bojer Madsen and Klaus Mølmer. Spin squeezing and precision probing with light and samples of atoms in the gaussian description. Phys. Rev. A, 70:052324, Nov 2004. doi: 10.1103/PhysRevA.70.052324. URL https://link.aps.org/doi/10.1103/PhysRevA.70.052324.

Easwar Magesan, Alexandre Cooper, Honam Yum, and Paola Cappellaro. Reconstructing the profile of time-varying magnetic fields with quantum sensors. Phys. Rev. A, 88:032107, Sep 2013. doi: 10.1103/PhysRevA.88.032107. URL https://link.aps.org/doi/10.1103/PhysRevA.88.032107.

Leonard Mandel and Emil Wolf. Optical Coherence. Cambridge University Press, 1995.

M. Suhail Zubairy Marlan O. Scully. Quantum Optics. Cambridge University Press, 1997.

F. Martin Ciurana, G. Colangelo, Robert J. Sewell, and Morgan W. Mitchell. Real-time shot-noise-limited differential photodetection for atomic quantum control. Opt. Lett., 41(13):2946–2949, Jul 2016. doi: 10.1364/OL.41.002946. URL http://ol.osa.org/abstract.cfm?URI=ol-41-13-2946.

F. Martin Ciurana, G. Colangelo, L. Slodička, R. J. Sewell, and M. W. Mitchell. Entanglement-enhanced radio-frequency field detection and waveform sensing. Phys. Rev. Lett., 119:043603, Jul 2017. doi: 10.1103/PhysRevLett.119.043603. URL https://link.aps.org/doi/10.1103/PhysRevLett.119.043603.

D. J. McCarron, S. A. King, and S. L. Cornish. Modulation transfer spectroscopy in atomic rubidium. Measurement Science and Technology, 19(10):105601, 2008. URL http://stacks.iop.org/0957-0233/19/i=10/a=105601.

J. M. McGuirk, G. T. Foster, J. B. Fixler, M. J. Snadden, and M. A. Kasevich. Sensitive absolute-gravity gradiometry using atom interferometry. Phys. Rev. A, 65:033608, Feb 2002. doi: 10.1103/PhysRevA.65.033608. URL https://link.aps.org/doi/10.1103/PhysRevA.65.033608.

Harold J. Metcalf and Peter van der Straten. Laser Cooling and Trapping. Springer-Verlag New York, 1999.

M. W. Mitchell, M. Koschorreck, M. Kubasik, M. Napolitano, and R. J. Sewell. Certified quantum non-demolition measurement of material systems. New Journal of Physics, 14(8):085021, 2012. URL http://stacks.iop.org/1367-2630/14/i=8/a=085021.

J. H. Müller, P. Petrov, D. Oblak, C. L. Garrido Alzar, S. R. de Echaniz, and E. S. Polzik. Diffraction effects on light–atomic-ensemble quantum interface. Phys. Rev. A, 71:033803, Mar 2005. doi: 10.1103/PhysRevA.71.033803. URL https://link.aps.org/doi/10.1103/PhysRevA.71.033803.

Mario Napolitano. Interaction-Based Nonlinear Quantum Metrology with a Cold Atomic Ensemble. PhD thesis, ICFO - UPC, 2014.

Caspar F. Ockeloen, Roman Schmied, Max F. Riedel, and Philipp Treutlein. Quantum metrology with a scanning probe atom interferometer. Phys. Rev. Lett., 111:143001, Oct 2013. doi: 10.1103/PhysRevLett.111.143001. URL http://link.aps.org/doi/10.1103/PhysRevLett.111.143001.

C. Orzel, A. K. Tuchman, M. L. Fenselau, M. Yasuda, and M. A. Kasevich. Squeezed states in a bose-einstein condensate. Science, 291(5512):2386–2389, 2001. ISSN 0036-8075. doi: 10.1126/science.1058149. URL http://science.sciencemag.org/content/291/5512/2386.

Poizat, J. Ph., Roch, J. F., and Grangier, P. Characterization of quantum non-demolition measurements in optics. Ann. Phys. Fr., 19(3):265–297, 1994. doi: 10.1051/anphys:01994001903026500. URL https://doi.org/10.1051/anphys:01994001903026500.

A. Predojević, Z. Zhai, J. M. Caballero, and M. W. Mitchell. Rubidium resonant squeezed light from a diode-pumped optical-parametric oscillator. Phys. Rev. A, 78:063820, Dec 2008. doi: 10.1103/PhysRevA.78.063820. URL https://link.aps.org/doi/10.1103/PhysRevA.78.063820.

Graciana Puentes, Gerald Waldherr, Philipp Neumann, Gopalakrishnan Balasubramanian, and Jörg Wrachtrup. Efficient route to high-bandwidth nanoscale magnetometry using single spins in diamond. Scientific Reports, 4:4677 EP, 04 2014. URL http://dx.doi.org/10.1038/srep04677.

I. I. Rabi, S. Millman, P. Kusch, and J. R. Zacharias. The molecular beam resonance method for measuring nuclear magnetic moments. the magnetic moments of ${}_3\mathrm{Li}^6$, ${}_3\mathrm{Li}^7$ and ${}_9\mathrm{F}^{19}$. Phys. Rev., 55:526–535, Mar 1939. doi: 10.1103/PhysRev.55.526. URL https://link.aps.org/doi/10.1103/PhysRev.55.526.

Norman F. Ramsey. A molecular beam resonance method with separated oscillating fields. Phys. Rev., 78:695–699, Jun 1950. doi: 10.1103/PhysRev.78.695. URL http://link.aps.org/doi/10.1103/PhysRev.78.695.

Max F. Riedel, Pascal Böhi, Yun Li, Theodor W. Hänsch, Alice Sinatra, and Philipp Treutlein. Atom-chip-based generation of entanglement for quantum metrology. Nature, 464(7292):1170–1173, 04 2010. URL http://dx.doi.org/10.1038/nature08988.

G. Rosi, F. Sorrentino, L. Cacciapuoti, M. Prevedelli, and G. M. Tino. Precision measurement of the newtonian gravitational constant using cold atoms. Nature, 510(7506):518–521, 06 2014. URL http://dx.doi.org/10.1038/nature13433.

Charles A. Sackett. Quantum measurement: A condensate's main squeeze. Nature, 464(7292):1133–1134, 04 2010. URL http://dx.doi.org/10.1038/4641133a.

J. J. Sakurai. Modern Quantum Mechanics. Addison-Wesley Publishing Company, 1994.

I. Savukov, T. Karaulanov, and M. G. Boshier. Ultra-sensitive high-density rb-87 radio-frequency magnetometer. Applied Physics Letters, 104(2):023504, 2014. doi: http://dx.doi.org/10.1063/1.4861657. URL http://scitation.aip.org/content/aip/journal/apl/104/2/10.1063/1.4861657.

I. M. Savukov, S. J. Seltzer, M. V. Romalis, and K. L. Sauer. Tunable atomic magnetometer for detection of radio-frequency magnetic fields. Phys. Rev. Lett., 95:063004, Aug 2005. doi: 10.1103/PhysRevLett.95.063004. URL http://link.aps.org/doi/10.1103/PhysRevLett.95.063004.

Monika H. Schleier-Smith, Ian D. Leroux, and Vladan Vuletić. Squeezing the collective spin of a dilute atomic ensemble by cavity feedback. Phys. Rev. A, 81:021804, Feb 2010a. doi: 10.1103/PhysRevA.81.021804. URL https://link.aps.org/doi/10.1103/PhysRevA.81.021804.

Monika H. Schleier-Smith, Ian D. Leroux, and Vladan Vuletić. States of an ensemble of two-level atoms with reduced quantum uncertainty. Phys. Rev. Lett., 104:073604, Feb 2010b. doi: 10.1103/PhysRevLett.104.073604. URL http://link.aps.org/doi/10.1103/PhysRevLett.104.073604.

Matthias Schulz. Tightly confined atoms in optical dipole traps. PhD thesis, Institut für Experimentalphysik, Innsbruck, 2002.

Alessio Serafini. Feedback control in quantum optics: An overview of experimental breakthroughs and areas of application. ISRN Optics, 2012:15, 2012. URL http://dx.doi.org/10.5402/2012/275016%]275016.

R. J. Sewell, M. Koschorreck, M. Napolitano, B. Dubost, N. Behbood, and M. W. Mitchell. Magnetic sensitivity beyond the projection noise limit by spin squeezing. Phys. Rev. Lett., 109:253605, Dec 2012. doi: 10.1103/PhysRevLett.109.253605. URL http://link.aps.org/doi/10.1103/PhysRevLett.109.253605.

R. J. Sewell, M. Napolitano, N. Behbood, G. Colangelo, and M. W. Mitchell. Certified quantum non-demolition measurement of a macroscopic material system. Nat Photon, 7(7):517–520, 07 2013. URL http://dx.doi.org/10.1038/nphoton.2013.100.

V. Shah, G. Vasilakis, and M. V. Romalis. High bandwidth atomic magnetometery with continuous quantum nondemolition measurements. Phys. Rev. Lett., 104:013601, Jan 2010. doi: 10.1103/PhysRevLett.104.013601. URL https://link.aps.org/doi/10.1103/PhysRevLett.104.013601.

D. Sheng, S. Li, N. Dural, and M. V. Romalis. Subfemtotesla scalar atomic magnetometry using multipass cells. Phys. Rev. Lett., 110:160802, Apr 2013. doi: 10.1103/PhysRevLett.110.160802. URL http://link.aps.org/doi/10.1103/PhysRevLett.110.160802.

Andrew P. V. Siemion, Paul Demorest, Eric Korpela, Ron J. Maddalena, Dan Werthimer, Jeff Cobb, Andrew W. Howard, Glen Langston, Matt Lebofsky, Geoffrey W. Marcy, and Jill Tarter. A 1.1-1.9 ghz seti survey of the kepler field. i. a search for narrow-band emission from select targets. The Astrophysical Journal, 767(1):94, 2013. URL http://stacks.iop.org/0004-637X/767/i=1/a=94.

A. Smith, B. E. Anderson, S. Chaudhury, and P. S. Jessen. Three-axis measurement and cancellation of background magnetic fields to less than 50 μG in a cold atom experiment. Journal of Physics B: Atomic, Molecular and Optical Physics, 44(20):205002, 2011. URL http://stacks.iop.org/0953-4075/44/i=20/a=205002.

Greg A. Smith, Souma Chaudhury, Andrew Silberfarb, Ivan H. Deutsch, and Poul S. Jessen. Continuous weak measurement and nonlinear dynamics in a cold spin ensemble. Phys. Rev. Lett., 93:163602, Oct 2004. doi: 10.1103/PhysRevLett.93.163602. URL https://link.aps.org/doi/10.1103/PhysRevLett.93.163602.

M. J. Snadden, J. M. McGuirk, P. Bouyer, K. G. Haritos, and M. A. Kasevich. Measurement of the earth's gravity gradient with an atom interferometer-based gravity gradiometer. Phys. Rev. Lett., 81:971–974, Aug 1998. doi: 10.1103/PhysRevLett.81.971. URL https://link.aps.org/doi/10.1103/PhysRevLett.81.971.

Lord Kelvin Snyder F. Wilbert. Lord kelvin on atoms as fundamental natural standards (for base units). IEEE Transactions on Instrumentation and Measurement, 22(1):99, March 1973.

D. Sofikitis, G. Stern, L. Kime, E. Dimova, A. Fioretti, D. Comparat, and P. Pillet. Loading a dipole trap from an atomic reservoir. Eur. Phys. J. D, 61(2): 437–442, 2011.

Anders S. Sørensen and Klaus Mølmer. Entanglement and extreme spin squeezing. Phys. Rev. Lett., 86:4431–4434, May 2001. doi: 10.1103/PhysRevLett.86.4431. URL https://link.aps.org/doi/10.1103/PhysRevLett.86.4431.

J. K. Stockton, K. Takase, and M. A. Kasevich. Absolute geodetic rotation measurement using atom interferometry. Phys. Rev. Lett., 107:133001, Sep 2011. doi: 10.1103/PhysRevLett.107.133001. URL https://link.aps.org/doi/10.1103/PhysRevLett.107.133001.

J. Suh, A. J. Weinstein, C. U. Lei, E. E. Wollman, S. K. Steinke, P. Meystre, A. A. Clerk, and K. C. Schwab. Mechanically detecting and avoiding the quantum fluctuations of a microwave field. Science, 344(6189):1262–1265, 2014. ISSN 0036-8075. doi: 10.1126/science.1253258. URL http://science.sciencemag.org/content/344/6189/1262.

T. Takano, M. Fuyama, R. Namiki, and Y. Takahashi. Spin squeezing of a cold atomic ensemble with the nuclear spin of one-half. Phys. Rev. Lett., 102:033601, Jan 2009. doi: 10.1103/PhysRevLett.102.033601. URL http://link.aps.org/doi/10.1103/PhysRevLett.102.033601.

M. Takeuchi, T. Takano, S. Ichihara, A. Yamaguchi, M. Kumakura, T. Yabuzaki, and Y. Takahashi. Fast polarimetry system for the application to spin quantum non-demolition measurement. Applied Physics B, 83(1):33–36, 2006. ISSN 1432-0649. doi: 10.1007/s00340-006-2137-x. URL http://dx.doi.org/10.1007/s00340-006-2137-x.

L. K. Thomsen, S. Mancini, and H. M. Wiseman. Continuous quantum nondemolition feedback and unconditional atomic spin squeezing. Journal of Physics B: Atomic, Molecular and Optical Physics, 35(23):4937, 2002a. URL http://stacks.iop.org/0953-4075/35/i=23/a=316.

L. K. Thomsen, S. Mancini, and H. M. Wiseman. Spin squeezing via quantum feedback. Phys. Rev. A, 65:061801, Jun 2002b. doi: 10.1103/PhysRevA.65.061801. URL https://link.aps.org/doi/10.1103/PhysRevA.65.061801.

Kip S. Thorne, Ronald W. P. Drever, Carlton M. Caves, Mark Zimmermann, and Vernon D. Sandberg. Quantum nondemolition measurements of harmonic oscillators. Phys. Rev. Lett., 40:667–671, Mar 1978. doi: 10.1103/PhysRevLett.40.667. URL http://link.aps.org/doi/10.1103/PhysRevLett.40.667.

Henning Vahlbruch, Moritz Mehmet, Simon Chelkowski, Boris Hage, Alexander Franzen, Nico Lastzka, Stefan Goßler, Karsten Danzmann, and Roman Schnabel. Observation of squeezed light with 10-db quantum-noise reduction. Phys. Rev. Lett., 100:033602, Jan 2008. doi: 10.1103/PhysRevLett.100.033602. URL https://link.aps.org/doi/10.1103/PhysRevLett.100.033602.

T. Vanderbruggen, R. Kohlhaas, A. Bertoldi, S. Bernon, A. Aspect, A. Landragin, and P. Bouyer. Feedback control of trapped coherent atomic ensembles. Phys. Rev. Lett., 110:210503, May 2013. doi: 10.1103/PhysRevLett.110.210503. URL https://link.aps.org/doi/10.1103/PhysRevLett.110.210503.

G. Vasilakis, V. Shah, and M. V. Romalis. Stroboscopic backaction evasion in a dense alkali-metal vapor. Phys. Rev. Lett., 106:143601, Apr 2011. doi: 10.1103/PhysRevLett.106.143601. URL http://link.aps.org/doi/10.1103/PhysRevLett.106.143601.

G. Vasilakis, H. Shen, K. Jensen, M. Balabas, D. Salart, B. Chen, and E. S. Polzik. Generation of a squeezed state of an oscillator by stroboscopic back-action-evading measurement. Nat Phys, 11(5):389–392, 05 2015. URL http://dx.doi.org/10.1038/nphys3280.

R. Vijay, C. Macklin, D. H. Slichter, S. J. Weber, K. W. Murch, R. Naik, A. N. Korotkov, and I. Siddiqi. Stabilizing rabi oscillations in a superconducting qubit using quantum feedback. Nature, 490(7418):77–80, 10 2012. URL http://dx.doi.org/10.1038/nature11505.

W. Wasilewski, K. Jensen, H. Krauter, J. J. Renema, M. V. Balabas, and E. S. Polzik. Quantum noise limited and entanglement-assisted magnetometry. Phys. Rev. Lett., 104:133601, Mar 2010. doi: 10.1103/PhysRevLett.104.133601. URL http://link.aps.org/doi/10.1103/PhysRevLett.104.133601.

Patrick J. Windpassinger. Non-destructive quantum state measurements and Quantum noise squeezing. PhD thesis, NBI - University of Copenhagen, 2008.

Patrick J Windpassinger, Marcin Kubasik, Marco Koschorreck, Axel Boisen, Niels Kjærgaard, Eugene S Polzik, and Jörg Helge Müller. Ultra low-noise differential ac-coupled photodetector for sensitive pulse detection applications. Measurement Science and Technology, 20(5):055301, 2009. URL http://stacks.iop.org/0957-0233/20/i=5/a=055301.

D. J. Wineland, J. J. Bollinger, W. M. Itano, F. L. Moore, and D. J. Heinzen. Spin squeezing and reduced quantum noise in spectroscopy. Phys. Rev. A, 46:R6797–R6800, Dec 1992. doi: 10.1103/PhysRevA.46.R6797. URL http://link.aps.org/doi/10.1103/PhysRevA.46.R6797.

D. J. Wineland, J. J. Bollinger, W. M. Itano, and D. J. Heinzen. Squeezed atomic states and projection noise in spectroscopy. Phys. Rev. A, 50:67–88, Jul 1994. doi: 10.1103/PhysRevA.50.67. URL https://link.aps.org/doi/10.1103/PhysRevA.50.67.

M. Wiseman and G. J. Milburn. Quantum Measurement and Control. Cambridge University Press, 2009.

H. Xia, A. Ben-Amar Baranga, D. Hoffman, and M. V. Romalis. Magnetoencephalography with an atomic magnetometer. Applied Physics Letters, 89(21): 211104, 2006. doi: 10.1063/1.2392722. URL http://dx.doi.org/10.1063/1.2392722.

Acknowledgments

I am dearly indebted to several people, without whom this thesis would not have been possible.

First of all, I would like to express my deep gratitude to Morgan Mitchell for advising this thesis. After being a master student in his group, and without many arguments for it, he gave me the opportunity to join his group. It has been a privilege to work with him and to learn from him encyclopedic knowledge. I really appreciated his support and motivation, and at the same time his constant effort to push to improve.

I am also indebted to Rob Sewell, who I have worked with during the first three years of my time at ICFO. Without his hard work and commitment, we would not have achieved our results. He taught me almost everything I know about the lab. I thank him for his support and advice.

I have spent most of my time in the lab ~~procrastinating theoretical calculations~~. It is in the laboratory when you really get to know the people you work with. I have been very lucky for sharing the lab with Naeimeh Behbood and Giorgio Colangelo, two amazing yet very different people. With Naimeh we coincide when the experiment decided not to work but we had to make it work because there was no time left. We learnt that events generally are cowards, they do not occur singly but run in packs and happen all at once, even so we made it. I have overlapped most of my time with Giorgio, and we really made a team. We reached a point when we knew what the other was thinking without saying a word. Together we domesticated the beast. It has been a great experience to spend so many hours in the lab with someone who is so energetic.

I would like to thank Mario Napolitano who cared for the young and gullible students. I also want to thank Lukas Slodička, who visited our lab for three months during which we started to work with radio-frequency signals and measured the first Rabi floppings. It was an enjoyable experience to work with someone deeply motivated with science. I learned a lot from him.

I thank the other members of our group, present and previous, for their support and the stimulating discussions. From the *light* lab: Yannick de Icaza Astiz, Federica Beduini, Joanna Zielinska, Gianvito Lucivero, Hara Troullinou, Jia Kong and Ricardo Jiménez. From the *atoms 2* lab, finally working with a BEC: Natali Martínez, Martijn Jasperse, Thomas Vanderbruggen, Pau Gómez, Simon Coop

and Silvana Palacios. The laboratory I worked on has been disassembled and a new line of research is starting, the so-called *1 atom* lab. To Nan Li, Vindhiya Prakash, Natalia Bruno and Lorena Bianchet (who for a short time was enrolled in our lab), I do not thank you for dismantle my lab (no resentment, in fact it is something I dreamed about a few times) but I wish you good luck, for sure the experiment will produce many interesting results in the future.

I owe a lot to my officemates. Yannick who introduced me many ICFOnians. Thanks to Gianvito who can cheer you up with just few words and likes listening to loud and good music. I cannot forget Fede and Natalia for the Spanish-Italian language exchange. I have never seen a lab-book so clean, organized and detailed as Fede's. It's an embarrassing comparison with mine and my terrible handwriting. And to my last officemate, Simon, who has to put up with my (hardly always) inappropriate jokes.

I am grateful to the people working on ICFO's administration department, especially to Human Resources, Purchases & Travel and Logistics. They make a great job and relieve us from most of the paper work and daily issues. I also want to thanks and highlight the help from ICFO's technicians, the support from IT department, and from the people working on the Mechanical and Electronic Workshops, they contribution in this thesis has been essential, in particular the work done by José Carlos Cifuentes, head of the Electronic Workshop, in the development of the balanced photo-detectors.

When you are in the lab, frustrated because the experiments does not work but there are no reasons for it, there is nothing like a "Hi!" or a smile from someone who is as frustrated as you are when you meet at the corridor. Thanks to the numerous other ICFOnians who brought be back to reality and made my time more pleasant. I am afraid they are so many that I cannot list them all, but you know who you are.

I must highlight a particular group of ICFOnians, *Los Puercos*, for the time we have shared outside ICFO, for the chats about physics, for the gossips and for the times we went out for a beer, but a single one ... Thank you Juan Miguel, Lisa, Miquel, Míriam, Giorgio, Roland, Silvana and Pau for your friendship and for being there.

Vull agrair a en Sàes, a en Miky i a l'Alba els grans moments d'esbarjo compartits durant aquest temps. No importa el temps que passi, sempre acabem rient fins que fa mal.

També vull reconèixer a na Laura Creixell per ses lliçons (necessàries?) de català.

De manera molt especial vull donar les gràcies a l'Isy i a l'Adri, dues de les persones que fa més temps que conec i que malgrat això encara m'aguanten. Sento que més que un agraïment els dec una disculpa, durant aquest temps massa vegades els hi he hagut de dir que no a tot de plans i quedades per estar enfeinat.

Merece un sincero agradecimiento Tere, quien me ha enseñado el poder de las coincidencias.

Finalment, aquest treball no hagués estat possible sense el suport incondicional de la meva família. Aquestes paraules no són suficients per expressar la meva gratitut, però també sé que no fa falta que ho digui perquè ja ho sabeu.

Last and least, I would like to thank my arms, for always being by side. My legs, for always supporting me, and my fingers... because I can always count on them.

"A bruise is a lesson... and each lesson makes us better"
George R. R. Martin, *Game of Thrones*